

SEARCH FOR THE STANDARD MODEL HIGGS BOSON IN THE DECAY
CHANNEL $H \rightarrow ZZ \rightarrow \ell^+\ell^-q\bar{q}$ AT CMS

A Dissertation

Submitted to the Faculty

of

Purdue University

by

Matthew K. Kress

In Partial Fulfillment of the

Requirements for the Degree

of

Doctor of Philosophy

December 2013

Purdue University

West Lafayette, Indiana

Dedication:

I would like to dedicate this work to my wife Julianne who has been such a support to me during my time at Purdue. She has truly been the joy of my life and I am so grateful that I can be a part of her life. I am also grateful for my children: Hyrum, Abraham, and Mercy. They have been so patient with me and are always there ready to play with me whenever I can. Also to my parents Naomi and Kip. They have always encouraged me to chase my dreams and provided me the encouragement and environment to do so.

I am grateful to Professor Bortoletto for being my advisor and allowing me the opportunity to join the CMS collaboration. I am amazed at her love for physics and the dedication she puts into her work. Also to those at Purdue that I have worked with, Jakub, Miguel, Petra, Daniele, and Mayra. They have been such a support to me and have been so good to answer all my questions.

I would also like to thank all the members of the 2l2q group for all the work they have done. Without them this analysis would never have been possible.

TABLE OF CONTENTS

	Page
LIST OF TABLES	vi
LIST OF FIGURES	viii
ABSTRACT	xviii
1 The Standard Model of Particle Physics	1
1.1 Particles and Forces	1
1.2 The Electroweak Interaction	3
1.3 The Higgs Boson	5
1.3.1 Higgs Boson Mass	6
1.4 The LHC Higgs Boson Search	11
1.4.1 LHC Higgs Production	11
1.4.2 Higgs Decay	14
1.4.3 $H \rightarrow ZZ \rightarrow l^+l^-q\bar{q}$ Channel	15
2 Experimental Apparatus	21
2.1 The Large Hadron Collider	21
2.2 The Compact Muon Solenoid	26
2.2.1 CMS Subsections	27
2.2.2 The CMS Trigger System	33
3 Electron, Muon, and Jet Reconstruction	37
3.1 Electron Reconstruction	37
3.2 Muon Reconstruction	38
3.3 Jet Reconstruction	40
3.4 Particle Flow Reconstruction	41
4 Event Selection	47
4.1 Datasets	47
4.1.1 Simulated Events	48
4.2 Pile-Up	48
4.3 Preselection	49
4.3.1 Lepton Selection	50
4.3.2 Jet Selection	52
4.3.3 B-tagging of jets	55
4.3.4 Higgs candidates	56
5 Signal Optimization	59

	Page
5.1 Tagging Classification	59
5.2 Helicity Likelihood	61
5.2.1 Angular Discriminant	67
5.3 Signal Optimization Based on Helicity Neural Network	70
5.3.1 Neural Network Architecture	73
5.3.2 Helicity Neural Network	74
5.3.3 Extended MVA Variables	78
5.4 Helicity Optimization	80
5.5 Missing Transverse Energy	82
5.6 Summary of Selection Requirements	86
6 Correlated and Uncorrelated Systematic Uncertainties	89
6.1 Signal Uncertainties	89
6.1.1 Trigger and Lepton Selection Efficiency	89
6.1.2 Jet Reconstruction	92
6.1.3 b-Tagging	94
6.1.4 MET uncertainty	95
6.1.5 Pile-up	95
6.1.6 Production mechanism	96
6.1.7 Luminosity uncertainty	98
6.2 Background systematic uncertainties	99
6.2.1 Background normalization uncertainties	99
6.2.2 Background shape uncertainties	99
6.2.3 Upper and Lower Side Band Comparison	101
7 Statistical interpretation and results	107
7.1 Signal determination	107
7.2 Results	108
8 Conclusion	117
A Data and Monte Carlo samples	119
B Trigger efficiencies and Monte Carlo correction factors	123
C Lepton identification requirements and efficiencies	127
D Systematic uncertainties on the signal	131
E Expected signal and background events per btag category	133
F Determination of $t\bar{t}$ background from data	135
G Mass distributions for the electron and muon channels	141
H Limit Cross Checks	145
I 3D Prototype Silicon Sensors	147

	Page
I.1 3D Sensors	147
I.2 Threshold and Noise Measurements	149
LIST OF REFERENCES	154

LIST OF TABLES

Table	Page
1.1 The three generations of spin $\frac{1}{2}$ particles.	2
1.2 The four forces and their associated gauge bosons. Charge is in units of the proton charge.	3
1.3 Electric charge (Q), isospin (I_3), and hypercharge (Y) of the fermions.	4
1.4 Electric charge (Q), isospin (I_3), and hypercharge (Y) of the Φ field.	6
1.5 Higgs production processes at the LHC.	13
1.6 The main Standard Model background processes for the $H \rightarrow ZZ \rightarrow l^+l^-q\bar{q}$ channel and their cross sections at 8 TeV [20].	18
4.1 Event trigger requirements for data.	51
4.2 Jet cuts to remove fakes.	54
5.1 B-tag categories.	59
5.2 Definitions of the 5 angular variables describing events of the form $ab \rightarrow X \rightarrow ZZ \rightarrow 2l2j$ as seen in Figure 5.2.	63
5.3 The polynomials used for fitting each angular variable.	69
5.4 Selection on the 3 b-tag categories.	87
5.5 Signal expected yields with 19.6 fb^{-1} of data. The background is the combination of Z+jets, $t\bar{t}$, and diboson Monte Carlo.	87
6.1 Summary of systematic uncertainties on signal normalization. Most sources are multiplicative errors on the cross section measurement, except for expected Higgs cross section.	90
6.2 The Legs for the Electron HLT.	92
6.3 These are the event requirements for the tag and probe method of calculating trigger and lepton selection efficiency.	92
6.4 Jet energy scale (JES) uncertainty for a variety of Higgs boson masses.	94
6.5 Systematic uncertainties on the signal acceptance following PDF4LHC recommendations.	97

Table	Page
6.6 Summary of systematic uncertainties on the normalization and shape of the background determination.	100
A.1 Data samples used in the analysis.	119
A.2 The signal samples, $H \rightarrow ZZ \rightarrow \ell^+\ell^- q\bar{q}$ ($\ell = e, \mu, \tau$), simulated with POWHEG are <i>/GluGluToHToZZTo2L2Q_M-xyz_8TeV-powheg-pythia6/Summer12_DR53X-PU_S10_START53_V7A-v1/AODSIM</i> , where xyz is the Higgs boson mass hypothesis, m_H . The cross section times branching fraction for each m_H value is listed in pb. Each sample was generated with 300,000 events.	120
A.3 Background simulated samples of the Summer12 production used in the analysis. The equivalent luminosity of the processed events for each sample is computed using the (N)NLO cross section in the 3 rd column.	121
B.1 Working point loose to the HLT Ele8 leg tag-and-probe efficiencies and scale factors.	123
B.2 Working point loose to the HLT Ele17 leg tag-and-probe efficiencies and scale factors.	124
B.3 Dimuon trigger efficiencies, calculated using the Muon POG official numbers, for two tight muons, both with $p_T > 20$ GeV/ c , in four bins of pseudorapidity for each of the two muons.	125
B.4 Muon trigger efficiencies from trigger simulation for the Z+jets simulated samples.	125
B.5 Muon trigger efficiencies from trigger simulation for the Higss (300 GeV) simulated samples.	126
C.1 Electron ID requirements for the Loose ID working point.	128
C.2 Muon ID requirements for the Tight ID working point.	128
C.3 Data to simulation scale factors for electron (upper) and muon (lower) identification requirements in various η ranges.	129
D.1 Systematic uncertainty on the signal in the muon channel.	131
D.2 Systematic uncertainty on the signal in the electron channel.	132
E.1 Expected yields in the 0-btag category.	133
E.2 Expected yields in the 1-btag category.	133
E.3 Expected yields in the 2-btag category.	134

LIST OF FIGURES

Figure	Page
1.1 An effective potential, $V(\Phi)$, that leads to spontaneous symmetry breaking. [9]	7
1.2 Upper and lower bounds on the Higgs mass. [11]	8
1.3 The ratio $CL_S = CL_{(S+B)}/CL_B$ for the signal plus background hypothesis. Solid line: observation; dashed line: median background expectation. The dark and light shaded bands around the median expected line correspond to the 68% and 95% probability bands. The intersection of the horizontal line for $CL_S = 0.05$ with the observed curve is used to define the 95% confidence level lower bound on the mass of the Standard Model Higgs boson. [13]	10
1.4 Observed and median expected (for the background-only hypothesis) 95% C.L. Bayesian upper production limits expressed as multiples of the SM cross section as a function of Higgs boson mass for the combined CDF and D0 searches in all decay modes. The dark and light shaded bands indicate, respectively, the 1 and 2 standard deviations probability regions in which the limits are expected to fluctuate in the absence of signal. The blue short dashed line shows median expected limits assuming the SM Higgs boson is present at $m_H = 125$ GeV. [14]	11
1.5 Indirect determination of the Higgs boson mass: $\Delta\chi^2$ as a function of M_H for the standard fit (top) and the complete fit (bottom). The solid (dashed) lines give the results when including (ignoring) theoretical errors. [15]	12
1.6 The most important processes for Higgs production at hadron colliders. Gluon fusion (a), vector boson fusion (b), Associative production with W (c) and an example of the diagrams having associative production with a top pair (d). [17]	13
1.7 Standard Model Higgs boson production cross sections at $\sqrt{s} = 7, 8$ TeV. Transition for VBF at $MH=300$ GeV at 8 TeV is due to change from ZWA to complex-pole-scheme. [18]	14
1.8 Standard Model Higgs boson decay branching ratios for two different m_H ranges. [18]	16
1.9 Standard Model Higgs boson production cross section times branching ratio at $\sqrt{s} = 7$ TeV and 8 TeV. [18]	19
2.1 Standard Model cross sections at the Tevatron and LHC colliders. [21]	22
2.2 Map of the CERN accelerator complex. [23]	23

Figure	Page
2.3 Top left: ATLAS experiment [27]. Top right: CMS experiments [28]. Bottom left: LHCb experiment [29]. Bottom right: ALICE experiment [30].	24
2.4 Integrated luminosity delivered by the LHC to each experiment in 2010 to 2012. [31]	25
2.5 The CMS experiment. HCAL stands for hadron calorimeter and ECAL stands for Electromagnetic calorimeter.	27
2.6 A graphical slice of the CMS experiment.	28
2.7 Total integrated luminosity for 2010 to 2012 delivered by the LHC and recorded by CMS. [34]	29
2.8 A CMS detector glossary of the cylindrical coordinate system used in this paper [35].	30
2.9 CMS solenoid magnet. [37]	30
2.10 View of the CMS tracker in the rz-plane. Each line in the strip tracker represents a silicon strip detector, whereas lines in the pixel detector represent ladders and petals on which the detectors are mounted in the barrel and endcaps, respectively. [39]	31
2.11 Longitudinal section of the electromagnetic calorimeter (one quadrant). [40]	32
2.12 The barrel and endcap transition region. [40]	32
2.13 A quarter slice of the CMS HCAL detectors. The right end of the beam line is the interaction point. FEE denotes the location of the Front End Electronics for the barrel and the endcap. In the diagram, the numbers on the top and left refer to segments in η , and the numbers on the right and the bottom refer to scintillator layers. Colors/shades indicate the combinations of layers that form the different depth segments, which are numbered sequentially starting at 1, moving outward from the interaction point. The outer calorimeter is assigned depth 4. [42]	33
2.14 Overview of Level 1 Trigger. [43]	35
3.1 Muon momentum resolution when using the muon spectrometers only (blue), the tracker only (green), and the full system (red): barrel ($ \eta < 0.2$) results are shown on the left, endcaps ($1.8 < \eta < 2.0$) on the right. [48]	39
3.2 A sample parton-level event (generated with Herwig [50]), together with many random soft “ghosts”, clustered with the anti- k_t algorithm, illustrating the “active” catchment areas of the resulting hard jets. This shows the cylindrical jets all with radius of R=1 or less. [49]	41

Figure	Page
3.3 Reconstructed jet energy fractions as a function of jet pseudo-rapidity. In the central region, bottom to top: charged hadrons (red), photons (blue), electrons (cyan), neutral hadrons (green). In the forward region: HF hadrons (pink), HF electromagnetic particles (gray). [48]	42
3.4 Jet response as a function of η integrated over all p_T 's below 750 GeV (top) and as a function of p_T , in the barrel (left) and in the endcaps (right). The response curves are fit with exponential functions of p_T . [51]	44
3.5 Jet-energy resolutions as a function of p_T for corrected calo-jets and for particle-flow jets (upwards triangles) in the barrel (left) and in the endcaps (right). The resolution curves are fit to the sum of a constant term, a stochastic term and a noise term. [51]	45
4.1 Top Left: Number of interaction in the 2012 data and the simulated samples for electrons. Top Right: Number of interaction in the 2012 data and the simulated samples for muons. Bottom Left: Electron Monte Carlo pile-up corrected. Bottom Right: Muon Monte Carlo pile-up corrected.	49
4.2 Di-lepton invariant mass in data and MC of $Z \rightarrow \ell\ell$ candidates after lepton selection. Left: Muon channel. Right: Electron channel. The selection described in preselection is applied except for the cut on m_{jj}	53
4.3 β fraction of the total transverse momentum of charged particles in a jet that is computed from particles pointing to the primary interaction for different background and signal samples (left) and efficiency of a cut in $\beta < 0.2$ for signal with Higgs mass of 200 GeV and 300 GeV and Z+Jets background, as a function of the number of reconstructed vertices in an event(right). [65]	54
4.4 Di-jet invariant mass in data and MC for $\ell\ell jj$ candidates which have passed the preselection. Left: Muon channel. Right: Electron channel.	55
4.5 Distribution of the jet probability (JP) discriminator that is used for b-tagging. Right: Muons. Left: Electrons. The peaks in the distribution come from calculating the jet probability non-continuously in η bins. This phenomenon is well understood and expected.	57
4.6 An event display of a Higgs event candidate decaying to two muons and two jets. [67]	58

Figure	Page
5.1 Various kinematic variables comparing Z+Jets background and Higgs of 300 GeV simulations to demonstrate the correlation between the kinematics and m_{ZZ} . (Top Left) $p_T(ll)$ vs m_{ZZ} for Z+Jets. (Top Right) $p_T(ll)$ vs m_{ZZ} for Higgs 300. (Middle Left) $p_T(jj)$ vs m_{ZZ} for Z+Jets. (Middle Right) $p_T(jj)$ vs m_{ZZ} for Higgs 300. (Bottom Left) ΔR_{jj} vs m_{ZZ} for Z+Jets. (Bottom Right) ΔR_{jj} vs m_{ZZ} for Higgs 300.	62
5.2 Diagram depicting the decay $X \rightarrow ZZ \rightarrow 2l2q$ and the 5 decay angles which describe it.	64
5.3 Five angular distributions of $\cos \theta_1, \cos \theta_2, \cos \theta^*, \Phi, \Phi_1$ and the helicity likelihood discriminant for 2012 electron data (points) and Summer 2012 Monte Carlo samples (histogram) in the 0 b-tag category. The red line is the expected distribution for a Higgs boson with mass 300 GeV. The selection is as described in preselection.	64
5.4 Five angular distributions of $\cos \theta_1, \cos \theta_2, \cos \theta^*, \Phi, \Phi_1$ and the helicity likelihood discriminant for 2012 electron data (points) and Summer 12 Monte Carlo samples (histogram) in the 1 b-tag category. Open histograms indicate the expected distribution for a Higgs boson with mass 300 GeV. The selection is as described in preselection.	65
5.5 Five angular distributions of $\cos \theta_1, \cos \theta_2, \cos \theta^*, \Phi, \Phi_1$ and the helicity likelihood discriminant for 2012 electron data (points) and Summer 12 Monte Carlo samples (histogram) in the 2 b-tag category. Open histograms indicate the expected distribution for a Higgs boson with mass 300 GeV. The selection is as described in preselection.	65
5.6 Five angular distributions of $\cos \theta_1, \cos \theta_2, \cos \theta^*, \Phi, \Phi_1$ and the helicity likelihood discriminant for 2012 muon data (points) and Summer 12 Monte Carlo samples (histogram) in the 0 b-tag category. The red line is the expected distribution for a Higgs boson with mass 300 GeV. The selection is as described in preselection.	66
5.7 Five angular distributions of $\cos \theta_1, \cos \theta_2, \cos \theta^*, \Phi, \Phi_1$ and the helicity likelihood discriminant for 2012 muon data (points) and Summer 12 Monte Carlo samples (histogram) in the 1 b-tag category. Open histograms indicate the expected distribution for a Higgs boson with mass 300 GeV. The selection is as described in preselection.	66
5.8 Five angular distributions of $\cos \theta_1, \cos \theta_2, \cos \theta^*, \Phi, \Phi_1$ and the helicity likelihood discriminant for 2012 muon data (points) and Summer 12 Monte Carlo samples (histogram) in the 2 b-tag category. Open histograms indicate the expected distribution for a Higgs boson with mass 300 GeV. The selection is as described in preselection.	67

Figure	Page
5.9 Fitting the angular variables for a reconstructed Higgs mass of 500 GeV in signal Monte Carlo samples (first 5 plots) and for the Z+Jets background samples (bottom 5 plots). These are taken in a mass window of 450 GeV to 550 GeV in the ZZ invariant mass distribution.	70
5.10 Fitting the parameters a_2 (left), a_4 (middle), a_6 (right) for $\cos(\theta_1)$ to calculate the acceptance function $G_{\theta_1}(\theta_1; M)$ as a function of the reconstructed Higgs mass. The same fitting is done for the other angular variables.	71
5.11 A $\cos(\theta^*)$ comparison for the 450 GeV reconstructed Higgs mass signal simulations fitting the acceptance function $G_{\theta_1}(\theta_1; M)$ directly to data (right), and plotting $G_{\theta_1}(\theta_1; 450)$ from the extrapolated polynomial coefficients (left). There is very good agreement between the fitting and extrapolation.	71
5.12 HelyLD for electrons (right) and muons(left) for the 3 b-tag categories, 0-tag (top), 1-tag (middle), 2-tag (bottom). The preselection is applied to this data and the 300 GeV signal Monte Carlo is scaled by 100 to get a better picture of the comparison.	72
5.13 $\cos(\theta^*)$ distributions for electrons (right) and muons (left). The mismatch between simulation and data can be seen in the range $0.8 < \cos(\theta^*) < 1.0$	73
5.14 HelyLD distribution after applying the selection $0.8 < \cos(\theta^*) $ showing much better agreement between Monte Carlo simulation and data.	73
5.15 Neural Network architecture used for the training.	74
5.16 The training is done after preselection and mixing electrons and muons. Additionally we require at least one JP medium jet with training 400 GeV Higgs boson with a MLP neural network.	75
5.17 The MLP neural network distribution for electrons (top) and muons (bottom). This training was done on the 400 GeV signal simulations, but applied to the 300, 400, 500, and 600 GeV samples to display the discriminating power over the entire mass range. The signal simulations are scaled for ease of reading.	76
5.18 The ROC curve for signal and background comparing the HelyLD, MLP, and an alternate training for a likelihood discriminant using the TMVA package after preselection (right). The same curve is given with additional selection of -6%/+10% of the Higgs mass to give a better estimation of performance for the final shape analysis.	77

Figure	Page
5.19 The MLP neural network output for electrons (right column) and muons (left column) for the 0 b-tag region (top row), 1 b-tag region (center row) and 2 b-tag region (bottom row). This is after preselection and also has a 300 GeV signal sample superimposed on the graphs multiplied by 100 for better visibility.	78
5.20 Background Rejection Versus Signal Efficiency in the 1tag region comparing the Multi Variant Analysis output to the helicity likelihood discriminant for a Higgs mass of 200, 300, 400, and 500 GeV. This is calculated after preselection, Z boson mass requirements, and requirements on MET significance, in a -6%/+10% Higgs mass window.	79
5.21 Background Rejection Versus Signal Efficiency in the 2tag region comparing the Multi Variant Analysis output to the the helicity likelihood discriminant for a Higgs mass of 200, 300, 400, and 500 GeV. This is calculated after preselection, Z boson mass requirements, and requirements on MET significance, in a -6%/+10% Higgs mass window.	80
5.22 Signal samples are normalized to background. Left: $\frac{Z_{upt}}{\sum pt}$ after preselection. Right: $\frac{Z_{upt}}{\sum pt}$ after preselection and $376 < m_{ZZ} < 440$ GeV.	81
5.23 Applying a MLP training to preselection and at least one JP medium jet. The working point is the equivalent performance of current analysis that we apply in the two tag region. The helyLD variable is shown for comparison. Left: ROC curves after preselection. Right: ROC curves after preselection and $376 < m_{ZZ} < 440$ GeV.	81
5.24 This training is for a MLP neural network trained on the 5 decay angles of a Higgs 400 GeV sample. This training is applied after preselection and requiring at least one JP medium jet to samples with a Higgs mass of 300, 400, and 500 GeV. The working point is the background rejection point that we currently achieve in the two tag region in our analysis. The helyLD variable is shown for comparison.	82
5.25 The Punzi equation $\frac{\text{sig}_{eff}}{0.98 + \sqrt{B}}$ for the 3 b-tag regions 0-tag (left column), 1-tag (center column), 2-tag (right column) and Higgs masses 300 (top row), 400 (second row), 500 (third row), 600 (bottom row) GeV. Also a selection outside of the region $\pm 20\%$ around the Higgs masses for each sample is applied to make it similar to the final region. Each plots shows electrons and muons separately.	83

Figure	Page
5.26 Distributions for MET significance after preselection for electrons (right column) and muons (left column) for the 0 b-tag region (top row), 1 b-tag region (center row), and 2 b-tag region (bottom row). A signal simulation is superimposed for a Higgs 300 GeV and multiplied by 100 for ease of reading.	85
6.1 Fitting of super-cluster to GSF Electrons for ϵ_{RECO} calculation.	93
6.2 Fitting of GSF Electrons for ϵ_{ISO} calculation.	93
6.3 Estimated number of true interactions in 2012 data, assuming different values of minimum-bias cross section. The central value is 69.3 mb (solid circles).	96
6.4 Left: reconstructed $m_H = 600\text{GeV}$ Higgs signal (area normalized) with the nominal line-shape (black) and systematic variations (blue/red). Gaussian fits to the core of the distribution are overlaid. Right: parameterization of the signal efficiencies, as function of the Higgs mass hypothesis, in the three btag categories, and the muon and electron channels.	98
6.5 Shape variation of the $M_{\ell\ell jj}$ distribution for Z+jets simulated events when varying the systematic uncertainties: (left) jet energy scale, (right) $p_T^{\ell\ell jj}$ -based re-weighting. Black dots denote the reference shapes. Red and blue histograms indicate the up and down variations of the corresponding systematic uncertainties.	101
6.6 Relative difference on the shape of the $M_{\ell\ell jj}$ distribution for Z+jets simulated events when varying the systematic uncertainties: (left) jet energy scale, (right) $p_T^{\ell\ell jj}$ -based re-weighting.	102
6.7 Residual differences in the $M_{\ell\ell jj}$ distributions between the data and the background, in the M_{jj} sideband control region (top). Alternative templates for the background prediction taking into account those residual variations, for the electron (middle) and the muon channels (bottom).	103
6.8 Comparing Data and MC in the 0 btag regions for both the upper sideband and lower sideband regions. Data and MC are first normalized to unity before the comparisons. All plots are a function of the mass of the two Zs. Top left: Data - MC for electrons. Top right: Data - MC for muons. Bottom left: Data/MC for electrons. Bottom right: Data/MC for muons.	104
6.9 Comparing Data and MC in the 1 btag regions for both the upper sideband and lower sideband regions. Data and MC are first normalized to unity before the comparisons. All plots are a function of the mass of the two Zs. Top left: Data - MC for electrons. Top right: Data - MC for muons. Bottom left: Data/MC for electrons. Bottom right: Data/MC for muons.	105

Figure	Page
6.10 Comparing Data and MC in the 2 btag regions for both the upper sideband and lower sideband regions. Data and MC are first normalized to unity before the comparisons. All plots are a function of the mass of the two Zs. Top left: Data - MC for electrons. Top right: Data - MC for muons. Bottom left: Data/MC for electrons. Bottom right: Data/MC for muons.	106
7.1 Parameterization of signal efficiency as a function of Higgs mass hypothesis in 0-btag (left), 1-btag (middle), 2-btag (right) categories and in the muon (top) and electron (bottom) channels.	108
7.2 Mass distributions of the $\ell^+\ell^-jj$ system for events in the signal region in the electron (top) and muon (bottom) channels. From left to right, plots correspond to the 0-, 1-, and 2-btag categories.	110
7.3 Mass distributions of Figure 7.2 in logarithmic scale.	110
7.4 Mass distributions of the $\ell^+\ell^-jj$ system for events in the m_{jj} sideband region in the electron (top) and muon (bottom) channels. From left to right, plots correspond to the 0-, 1-, and 2-btag categories.	111
7.5 Mass distributions of Figure 7.4 in logarithmic scale.	111
7.6 Observed (solid) and expected (dashed) 95% CL upper limit on the ratio of the production cross section to the SM expectation for the Higgs boson obtained using the CL_s technique. The 68% and 95% ranges of expectation for the background-only model are also shown with green and yellow bands, respectively. The solid line at 1 indicates the expectation for a SM-Higgs-like boson. The plot shows the expected and observed limits using 19.6 fb^{-1} of data.	113
7.7 Observed (solid) and expected (dashed) 95% CL upper limit on the ratio of the production cross section to the SM expectation for the Higgs boson obtained using the CL_s technique, separate for the different lepton flavor and b-tag categories. The 68% and 95% ranges of expectation for the background-only model are also shown with green and yellow bands, respectively. The solid line at 1 indicates the expectation for a SM-Higgs-like boson.	114
7.8 Observed (solid) and expected (dashed) 95% C.L. upper limit on the product of the production cross section and branching fraction for $H \rightarrow ZZ$ obtained with the CL_s technique. The 68% and 95% ranges of expectation for the background-only model are also shown with green and yellow bands, respectively. The left plot shows the observed limit only at the points where the signal shape can be directly obtained from the simulation. .	115

Figure	Page
7.9 Observed (solid) and expected (dashed) 95% CL upper limit on the ratio of the production cross section to the SM expectation for the Higgs boson obtained using the CL_s technique. The 68% and 95% ranges of expectation for the background-only model are also shown with green and yellow bands, respectively. The solid line at 1 indicates the expectation for a SM-Higgs-like boson. This result is the combination of this study (i.e. Figure 7.6) with the previous 2011 results.	116
F.1 Powheg + Pythia top MC $e^\pm\mu^\mp$ to $(e^+e^- + \mu^+\mu^-)$ comparison for several variables after different steps of the selection, as specified in the legends. Top: dilepton (left) and dijet transverse momentum (right). Bottom: dilepton + dijet “Higgs” invariant mass (left) and transverse momentum (right).	136
F.2 Comparison of 2012 $e^\pm\mu^\mp$ data to Powheg + Pythia top MC, corresponding to an integrated luminosity of 19.6 fb^{-1} . Red dots are $e^\pm\mu^\mp$ data; white histogram top Monte Carlo; blue histogram other small backgrounds. Top: dilepton invariant mass (left) and dijet invariant mass (right). Bottom: “Higgs” invariant mass for events with 1 JPL b-tag (left), and two (1 JPM + 1 JPL) b-tags and MET significance < 10 (right).	137
F.3 MET significance distribution for dilepton data compared to the sum of Drell-Yan Monte Carlo plus $e^\pm\mu^\mp$ data for events with two btags (left). Dijet invariant mass (right) for $e^+e^- + \mu^+\mu^-$ and $e^\pm\mu^\mp$ data for events outside the leptonic Z mass window, with two b-tags, and MET significance > 8 . Other cuts are detailed in the text. Red dots are $e^+e^- + \mu^+\mu^-$ data; white histogram Drell Yan Monte Carlo; blue histogram $e^\pm\mu^\mp$ data (plus other small backgrounds).	138
F.4 Comparison of 2012 $e^\pm\mu^\mp$ data to Powheg + Pythia top MC normalized to the $t\bar{t}$ NLO cross-section. Red dots are $e^\pm\mu^\mp$ data; white histogram top Monte Carlo. Top: dilepton invariant mass (left) and dijet invariant mass (right). Bottom: MET significance (left), and “Higgs” invariant mass (right).	139
G.1 Mass distributions of the $\ell^+\ell^-jj$ system for events in the electron and muon channels: data in the m_{jj} (top) signal and (bottom) sideband regions. From left to right, plots correspond to the 0-, 1-, and 2-btag categories.	141

Figure	Page
H.1 Observed (solid) and expected (dashed) 95% CL upper limit on the ratio of the production cross section to the SM expectation for the Higgs boson obtained using the <i>cut-and-count</i> technique, which integrates the mass distributions in a range [$m_H - 6\%$, $m_H + 10\%$] around each Higgs mass hypothesis. The 68% and 95% ranges of expectation for the background-only model are also shown with green and yellow bands, respectively. The solid line at 1 indicates the expectation for a SM-Higgs-like boson.	145
I.1 Operations of planar and 3D detectors are depicted. [96]	148
I.2 Sketch of arrangement of columnar electrodes in CMS pixel sensors of 2E type (left) and 4E type(right). [96]	148
I.3 I-V characteristics of four 3D CMS pixel sensors with different combinations of substrate thickness and electrode configuration as measured at wafer level and after wire-bonding. The convention used in naming is wafer_electrode_configuration_sensor number. [96]	149
I.4 S-curves of an edge pixel and a regular pixel in the sensor WB5_2E_2 at a reverse bias of 40 V. The threshold and noise values are in VCAL units. [96]	150
I.5 Noise map of the WB5_2E_2 chip at a reverse bias of 40 V (left). Gaussian noise distribution of the WB5_2E_2 chip at a reverse bias of 40 V (right). [96]	151
I.6 Noise as a function of reverse bias voltage for the four sensors featuring different substrate thickness and electrode configuration. [96]	152
I.7 Threshold distribution of the WB2-16_2E_6 chip at a reverse bias of 40 V before trimming (right) and after trimming (left). [96]	152

ABSTRACT

Kress, Matthew K. Ph.D., Purdue University, December 2013. Search for the Standard Model Higgs Boson in the decay channel $H \rightarrow ZZ \rightarrow \ell^+\ell^-q\bar{q}$ at CMS. Major Professor: Daniela Bortoletto.

A search for a standard-model-like Higgs boson decaying into two Z bosons with subsequent decay into two leptons and two quark-jets, $H \rightarrow ZZ \rightarrow l^+l^-q\bar{q}$, is presented. The CMS experiment collected 19.6 fb^{-1} of data in 2012 of pp collisions at $\sqrt{s} = 8 \text{ TeV}$. The analysis uses the kinematics of the final state and quark flavor tagging to select the Higgs boson signal in the mass range between 230 GeV and 650 GeV. No evidence of a Higgs boson signal is found and upper limits are set on the Higgs boson production cross section in that mass range.

1. The Standard Model of Particle Physics

This Chapter will give an introduction to the current theoretical framework in elementary particle physics. We will describe the Standard Model and the motivation behind the Higgs mechanism.

Natural units will be used, i.e. $\hbar = c = 1$, in this analysis unless otherwise specified.

1.1 Particles and Forces

The Standard Model describes matter as comprised of 3 families which each contain 4 elementary particles. Each of these particles are spin 1/2 fermions. Fermions are particles that follow the Pauli exclusion principle which states that the wave function of identical fermions is anti-symmetric in the exchange of the two particles [1]. The first family is the building blocks of all ordinary matter while the second and third families are heavier copies of the first. The corresponding particles that belong in the various families are said to have different flavor. There is a natural division of the fermions into two groups. These are leptons and quarks, and their classification can be seen in Table 1.1. Quarks are never found isolated in nature, but are constituents of composite particles called hadrons. The most common examples of hadrons are protons (two up quarks and one down quark) and neutrons (one up quark and two down quarks). There are over 100 different hadrons which have led particle physicists to refer to them and other particles collectively as the Particle Zoo.

Interactions between particles are mediated through the exchange of force carriers which are bosons. Bosons are particles which have integer spin and do not obey the Pauli exclusion principle which means they can occupy the same quantum state as other identical bosons. The force carrier bosons are summarized in Table 1.2.

Throughout this thesis, the gravitational interaction, which is mediated by the theorized graviton, will not be taken into account because at the mass and distance ranges studied the interactions are negligible. The W and Z bosons mediate the weak force which is responsible for both radioactive decay and nuclear fusion of subatomic particles. The term weak is used because the strength of the field is typically several orders of magnitude less than both the strong force and electromagnetism. Also, because the masses of the W and Z bosons are so large, the weak force has a very short range, around $10^{-17} - 10^{-16}$ m [2]. The strong force is mediated by the gluons and is around 100 times stronger than electromagnetism while working at the atomic scale. This force binds quarks together to form hadrons, and binds protons and neutrons together to form the nucleus of atoms. The electromagnetic force is mediated by the photon and works on an infinite scale but falls off proportional to the square of the distance.

The Standard Model describes these interactions using two theories. Quantum Chromodynamics (QCD) describes the strong force while the theory of the electroweak interaction [3] unifies the electromagnetic and weak interactions as described earlier. The following section will describe in more detail the electroweak interaction because it is the primary decay of interest to this work.

Table 1.1
The three generations of spin $\frac{1}{2}$ particles.

charge	-1	-2/3	-1/3	0	+1/3	+2/3	+1
1 st family	e ⁻	\bar{u}	d	$\nu_e, \bar{\nu}_e$	\bar{d}	u	e ⁺
2 nd family	μ^-	\bar{c}	s	$\nu_\mu, \bar{\nu}_\mu$	\bar{s}	c	μ^+
3 rd family	τ^-	\bar{t}	b	$\nu_\tau, \bar{\nu}_\tau$	\bar{b}	t	μ^+

Table 1.2

The four forces and their associated gauge bosons. Charge is in units of the proton charge.

Force	Boson	Charge	Mass
Gravitational	graviton(G)	0	?
Electromagnetic	photon(γ)	0	0
Weak	W boson(W^\pm)	± 1	81 GeV
	Z boson(Z)	0	92 GeV
Strong	gluon(g)	0	0

1.2 The Electroweak Interaction

Quantum Electrodynamics (QED) is a quantum field theory that describes the electromagnetic interaction. A problem in many field theories is that the amplitude of many processes needs to be calculated by integrating over all possible values of particle momentum and energy. This creates logarithmic divergences in these integrals, which are nonphysical. A process called re-normalization solves this problem [4]. Re-normalization involves separating the divergent parts and canceling out the non-physical parts. Many fields are not renormalizable, but in the early 1970's t'Hooft, Veltman, and others showed that gauge theories can be re-normalized [5] [6].

Gauge theories are theories that require their Lagrangian to be invariant under a group of local transformations. The possible invariant transformations, which are called gauge transformations, together form a Lie group. The group of local invariance is called a gauge group and has a corresponding gauge field which is included in the Lagrangian to ensure invariance under local group transformations. The quanta of gauge fields are gauge bosons [7]. In this work a detailed derivation of the electroweak Lagrangian will not be provided, but will simply be summarized.

The theory of electromagnetic interaction is based on the gauge group $U(1)_{EM}$. The quantum number in this theory that is conserved is the electric charge (Q).

Local invariance condition under the $U(1)_{EM}$ group leads to a massless vector boson which is the photon. To combine both the electromagnetic and weak interaction, the gauge symmetry is extended to the group $SU(2)_I \otimes U(1)_Y$. The three components of $t^a = \frac{1}{2}\tau^a$ (τ^a are the Pauli matrices), where t^a is the weak isospin operator, are the generators of the $SU(2)_I$ group. The weak hypercharge Y operator is the generator of the $U(1)_Y$ group. Using I_3 as the third component of the weak isospin, these quantum numbers satisfy equation 1.1.

$$Q = I_3 + \frac{Y}{2} \quad (1.1)$$

In table 1.3 the quantum numbers of the fermions are given where $u = u, c, t$, $d = d, s, b$, $l = e, \mu, \tau$, and $\nu = \nu_e, \nu_\mu, \nu_\tau$.

Table 1.3
Electric charge (Q), isospin (I_3), and hypercharge (Y) of the fermions.

	Q	I_3	Y
u	$2/3$	$1/2$	$1/3$
d	$-1/3$	$-1/2$	$1/3$
l	-1	$-1/2$	-1
ν	0	$1/2$	-1

Just like the requirement of local gauge invariance for the $U(1)_{EM}$ group gives a massless vector field, the group $SU(2)_I \otimes U(1)_Y$ now has four massless vector fields. These fields are $W_\mu^{1,2,3}$ and B_μ . These fields do not represent physical fields, but the physical fields are given by linear combinations of them. The W bosons, W^+ and W^- , are described in equation 1.2, the Z boson in equation 1.3, and the γ boson in equation 1.4.

$$W_\mu^\pm = \sqrt{\frac{1}{2}}(W_\mu^1 \mp iW_\mu^2) \quad (1.2)$$

$$Z_\mu = -B_\mu \sin\theta_W + W_\mu^3 \cos\theta_W \quad (1.3)$$

$$A_\mu = B_\mu \cos\theta_W + W_\mu^3 \sin\theta_W \quad (1.4)$$

The Weinberg angle (θ_W) is an open parameter of the standard model and can be determined empirically using the relation in equation 1.5, where m_W and m_Z are the respective masses of the W and Z bosons.

$$\cos\theta_W = \frac{m_W}{m_Z} \quad (1.5)$$

1.3 The Higgs Boson

The electroweak theory as described so far describes all particles as massless. Introducing a mass term for the gauge bosons would violate gauge invariance which is essential for re-normalization. To agree with experimental findings, some of the gauge bosons must have mass, as well as mass being needed to successfully describe the weak interaction phenomenology. By introducing the Higgs mechanism fermions and W^\pm , Z bosons are allowed to have mass [8]. Introducing a complex scalar $SU(2)$ doublet, Φ given in equation 1.6, allows the introduction of such a mechanism.

$$\Phi = \begin{pmatrix} \phi^+ \\ \phi^0 \end{pmatrix} \quad (1.6)$$

This field is introduced to the electroweak Lagrangian using the term in equation 1.7

$$\mathcal{L}_H = (D^\mu \Phi)^\dagger (D_\mu \Phi) + V(\Phi^\dagger \Phi), \quad (1.7)$$

where D_μ is the covariant derivative. The Φ field has the quantum numbers as seen in table 1.4 and has a potential that can be written as in equation 1.8. This potential can be seen graphically in Figure 1.1.

$$V(\Phi^\dagger \Phi) = -\mu^2 \Phi^\dagger \Phi - \lambda (\Phi^\dagger \Phi)^2 \quad (1.8)$$

Table 1.4
Electric charge (Q), isospin (I_3), and hypercharge (Y) of the Φ field.

Q	I_3	Y
ϕ^+	1	$1/2$
ϕ^0	0	$-1/2$

When $\mu^2 < 0$ and $\lambda > 0$, we get the minimum to be at $\frac{\nu^2}{2}$, where $\nu^2 = -\frac{-\mu^2}{\lambda}$ as seen in equation 1.9. The minimum of this potential does not correspond to a single value of Φ and these values are non-zero. The lowest energy state is arbitrary and is not invariant under rotations. This loss of rotational invariance is referred to as spontaneous symmetry breaking.

$$\Phi^\dagger \Phi = \frac{1}{2}(\Phi_1^2 + \Phi_2^2 + \Phi_3^2 + \Phi_4^2) = -\frac{\mu^2}{2\lambda} \equiv \frac{\nu^2}{2} \quad (1.9)$$

The spontaneous symmetry breaking introduces mass terms for the W^\pm and Z fields as well as a scalar field, which is the Higgs field. Spontaneously breaking a symmetry does not eliminate the symmetry but hides it under the choice of the ground state. Furthermore, the Higgs field is invariant under the $U(1)_{EM}$ group, leaving electromagnetic symmetry unbroken. The photon remains massless because it does not couple to the Higgs boson.

1.3.1 Higgs Boson Mass

The Higgs boson mass is the only one of the 18 free parameters of the Standard Model [10] that was still undetermined at the start up of the LHC. While the mass of the Higgs boson is dependent on the parameters ν and λ , only ν can be estimated from another parameter. Despite theoretically not being able to determine the Higgs boson mass, there are both theoretical and experimental constraints on the Higgs mass. These come from both direct and indirect searches at various colliders.

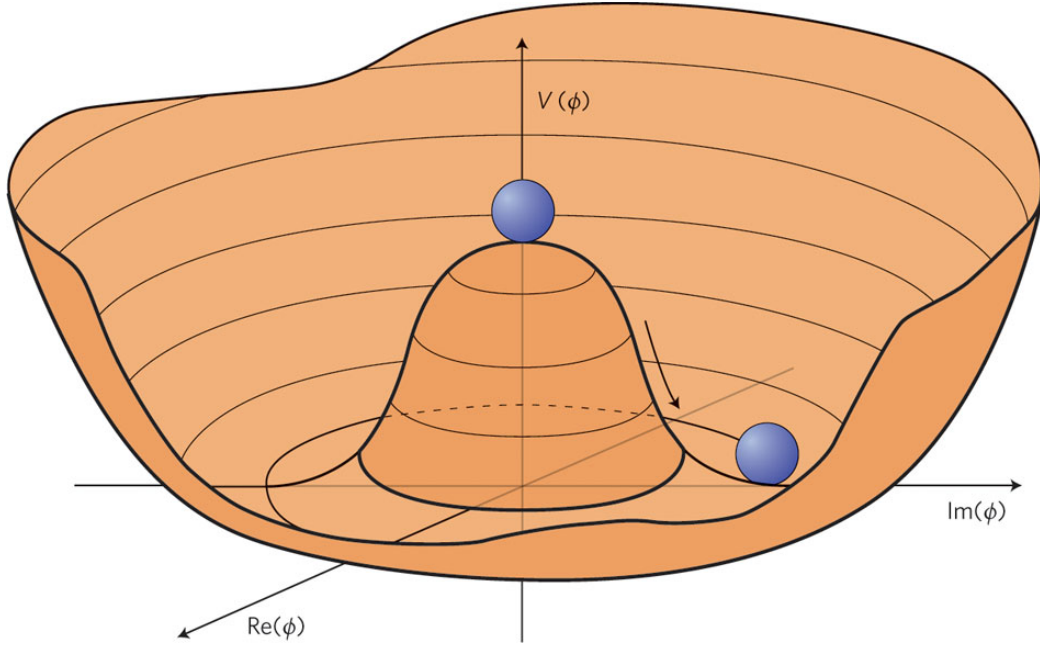


Figure 1.1. An effective potential, $V(\Phi)$, that leads to spontaneous symmetry breaking. [9]

Theoretical Constraints

The scalar potential needs to be bounded from below, even after including radiative corrections. This gives a lower bound on m_H as well. If the quartic coupling $\lambda(\mu)$ stays positive then this requirement is fulfilled. This is true at least until $\mu \sim \Lambda$ which is the maximum energy scale wherein the theory is still applicable [11]. The relation $m_H^2 \simeq 2\lambda(m_Z)v^2$ defines a Λ -dependent lower bound on m_H . This shows that for smaller values of $\lambda(m_Z)$ the Λ scale also becomes smaller. This leads to λ becoming negative which means the scalar potential is no longer bounded. The absolute minimum or vacuum stability is shown by the dashed line in figure 1.2. If the vacuum stability is only a local constraint we get a slightly looser lower bound as shown in the dot-dashed line in figure 1.2.

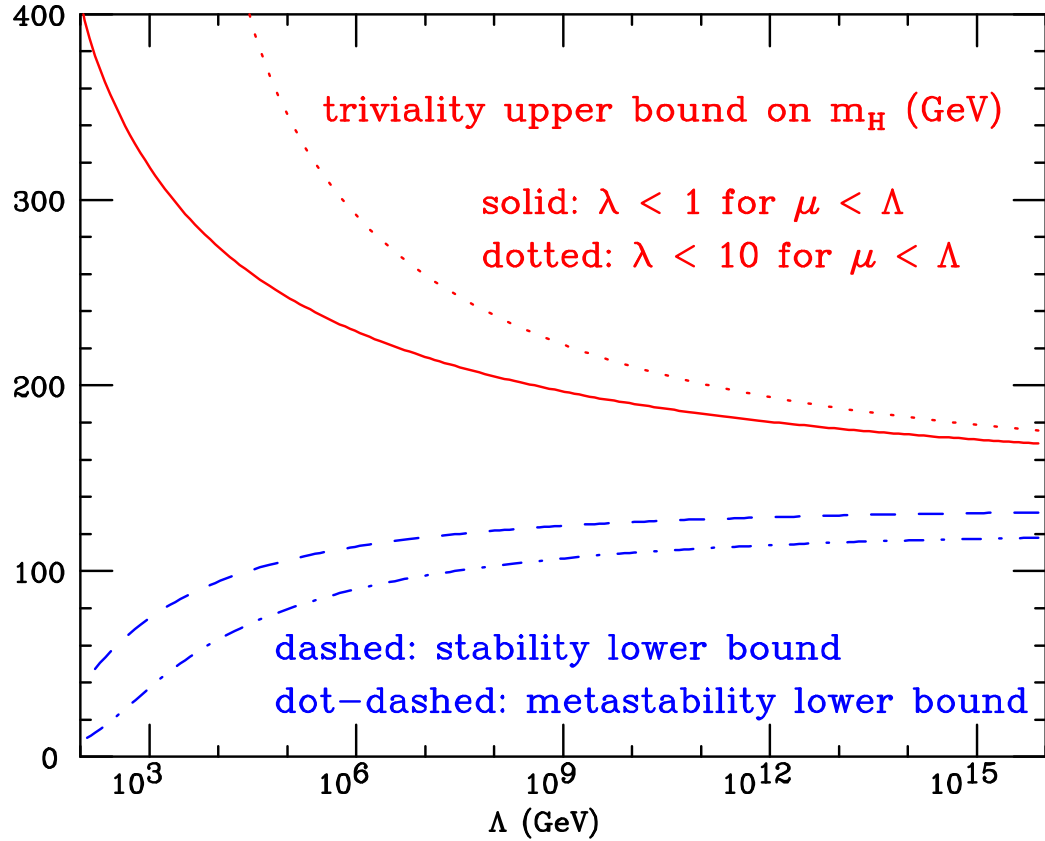


Figure 1.2. Upper and lower bounds on the Higgs mass. [11]

The unitarity of the scattering matrix gives an upper bound on the Higgs mass. This can be seen in the elastic scattering of Z bosons, $ZZ \rightarrow ZZ$. In the limit that $s \gg m_Z^2$ we have:

$$\mathcal{M} = -\frac{m_H^2}{v^2} \left[\frac{s}{s-m_H^2} + \frac{t}{t-m_H^2} + \frac{u}{u-m_H^2} \right] \quad (1.10)$$

Now with $J=0$ then the amplitude of \mathcal{M} gives us:

$$|\mathcal{M}_0|^2 \rightarrow \left[\frac{3}{16\pi} \frac{m_H^2}{v^2} \right]^2 < \frac{s}{s-4m_Z^2} \quad (1.11)$$

Since we said that $s \gg m_Z^2$ we get that $m_H < \sqrt{\frac{16\pi}{3}} v \sim 1$ TeV. Similarly if we look at $ZW \rightarrow ZW$ then the limit is ~ 800 GeV. There is another more restrictive constraint that is called the triviality bound. This is found by requiring that λ is finite all the way to the Λ scale. When these limits are taken to the grand unification

scale or Plank scale ($\Lambda \sim 10^{19}$ GeV) there is an extreme upper bound of 180 GeV [11]. Together with the extreme limits of the lower bound shows a Higgs mass should be in the range of somewhere 130 GeV to 180 GeV as seen in Figure 1.2. While this is a bit extreme, it does make sense for colliders to search up to a range of 1 TeV while focusing on the lower ranges.

Experimental Constraints before the LHC

In addition to the theoretical bounds, there were both direct and indirect measurements on the Higgs mass. Direct searches for the Higgs have mostly come from the Large Electron-Positron Collider (LEP) at CERN and the Tevatron at Fermilab [12]. This search has been a driving force in high-energy experiments for the last several decades. A brief overview of the constraints will be given below. Direct searches using data from LEP excluded the m_H below 114.4 GeV at a 95% C.L. [13]. LEP was an e^+e^- accelerator that ran from 1989 to 2000. The main production mechanism at LEP was $e^+e^- \rightarrow Z^* \rightarrow ZH$ where a Higgs is radiated by a virtual Z boson. This process is often referred to as “Higgs-strahlung”. The results can be seen in figure 1.3.

The Tevatron, at Fermilab, was a proton-antiproton collider which took data up until 2011. The center of mass energy of the Tevatron was 1.96 TeV. The main mode of Higgs production studied at the Tevatron was $p\bar{p} \rightarrow VH$ where V is a vector boson $V \equiv W^\pm, Z$. The decay products most studied is where the vector bosons decay into leptons. The most promising Higgs decay was $H \rightarrow W^+W^-$ if the Higgs had a mass above 135 GeV. The combination of the Tevatron results for the CDF and D \emptyset experiments can be seen in Figure 1.4 [14]. In addition to confirming part of the already excluded range from LEP, the range 149 to 182 GeV was excluded at the 95% confidence level.

Through fitting precision electroweak measurements, indirect measurements of the Higgs boson mass can be derived. Of particular usefulness is the changes in the vacuum polarization of the Z and W^\pm bosons through loop corrections. Figure 1.5 [15]

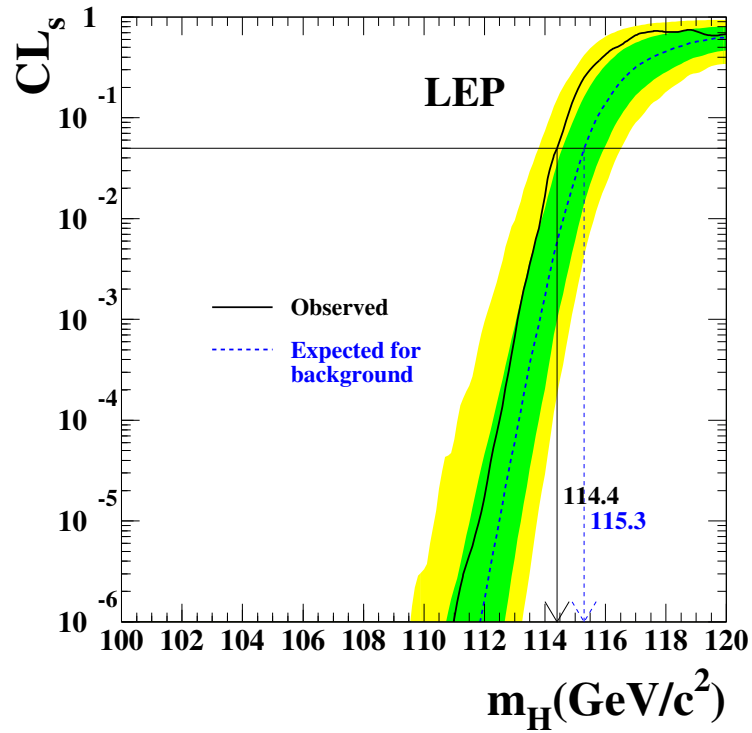


Figure 1.3. The ratio $CL_S = CL_{(S+B)}/CL_B$ for the signal plus background hypothesis. Solid line: observation; dashed line: median background expectation. The dark and light shaded bands around the median expected line correspond to the 68% and 95% probability bands. The intersection of the horizontal line for $CL_S = 0.05$ with the observed curve is used to define the 95% confidence level lower bound on the mass of the Standard Model Higgs boson. [13]

shows the $\Delta\chi^2$ variation of best fit to the combined data of LEP, Tevatron, and the Stanford Linear Accelerator (SLAC) accelerators, both with the pure indirect searches, and the combined direct and indirect searches. While the lower Higgs masses are favored, even the high mass ranges were not completely ruled out.

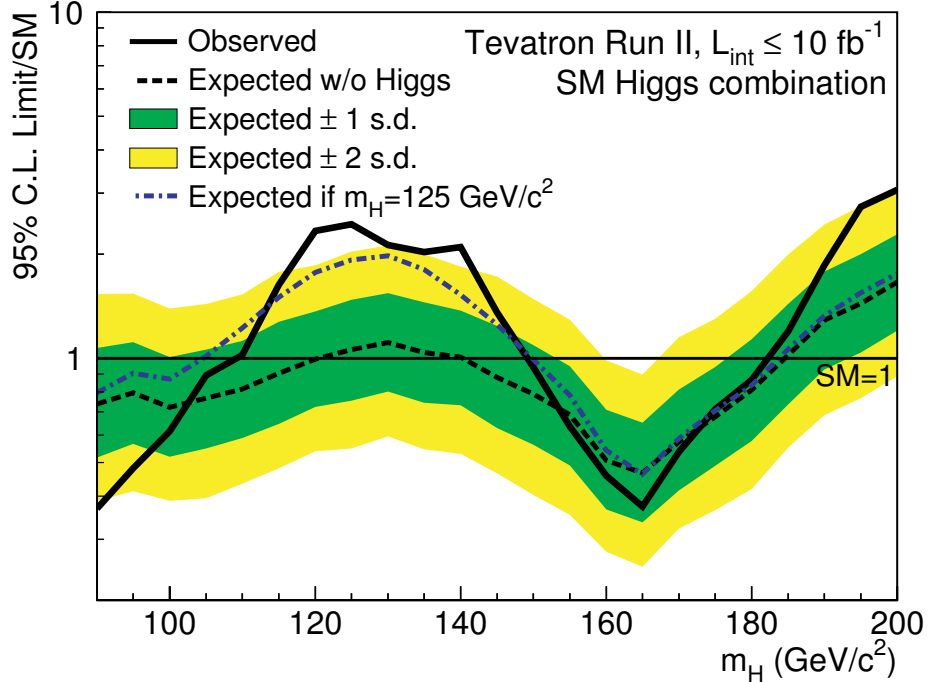


Figure 1.4. Observed and median expected (for the background-only hypothesis) 95% C.L. Bayesian upper production limits expressed as multiples of the SM cross section as a function of Higgs boson mass for the combined CDF and D0 searches in all decay modes. The dark and light shaded bands indicate, respectively, the 1 and 2 standard deviations probability regions in which the limits are expected to fluctuate in the absence of signal. The blue short dashed line shows median expected limits assuming the SM Higgs boson is present at $m_H = 125$ GeV. [14]

1.4 The LHC Higgs Boson Search

1.4.1 LHC Higgs Production

The Large Hadron Collider (LHC) at CERN is a proton-proton (pp) collider. It had a center of mass energy of 7 TeV in 2010-2011 which increased to 8 TeV in 2012. It reached an instantaneous luminosity of approximately $5 \times 10^{33} cm^{-2}s^{-1}$ [16] in 2012. There are four Higgs production processes at the LHC which are listed in Table 1.5 in order of decreasing cross section. The corresponding Feynman diagrams are in Figure 1.6 [17]. The cross sections for each of these processes at both \sqrt{s}

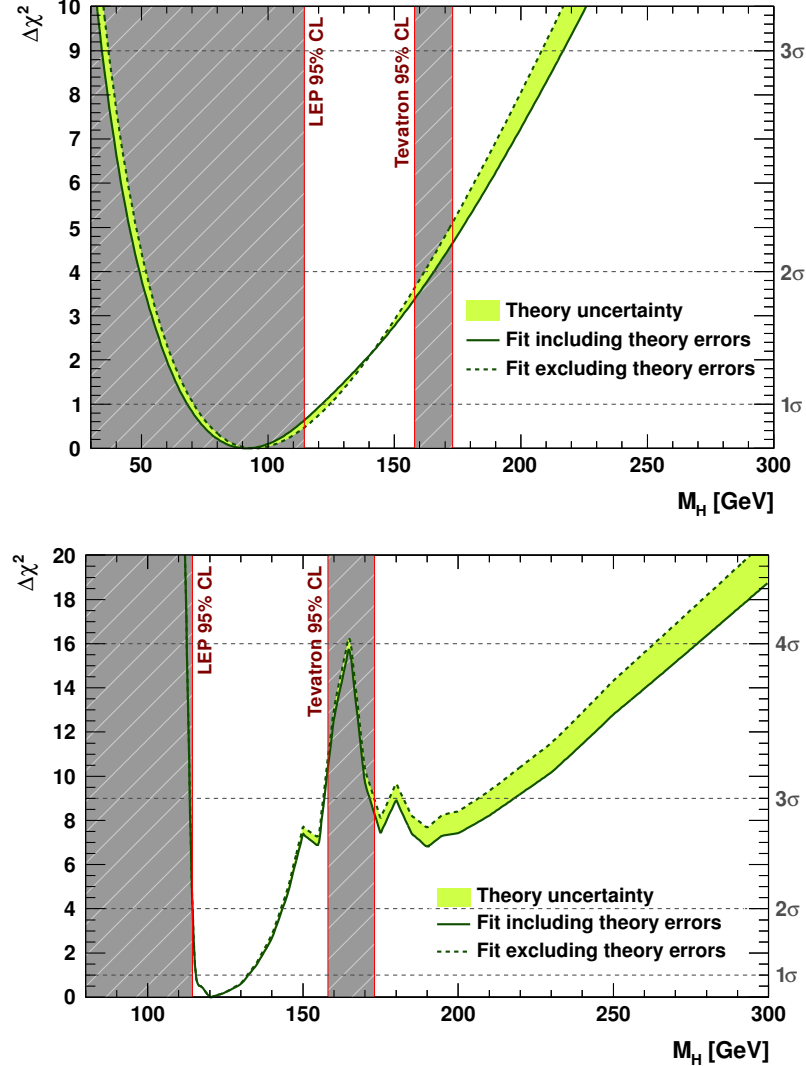


Figure 1.5. Indirect determination of the Higgs boson mass: $\Delta\chi^2$ as a function of M_H for the standard fit (top) and the complete fit (bottom). The solid (dashed) lines give the results when including (ignoring) theoretical errors. [15]

$= 7$ TeV and $\sqrt{s} = 8$ TeV can be seen in Figure 1.7 [18]. It is important to note that changing from 7 TeV to 8 TeV increased the inclusive Higgs boson production cross-section at $m_H = 125$ GeV by about 25%.

Gluon-gluon fusion is the dominant Higgs production process at the LHC center of mass energies. Vector boson fusion (VBF) is the second largest production cross

section and is about one order of magnitude less than gluon gluon fusion. In the very high mass region the processes become more comparable. Despite this lower cross section, VBF is extremely powerful because of the two spectator jets that have a large invariant mass. This signature allows good background discrimination. The following analysis mainly deals with these two processes.

Table 1.5
Higgs production processes at the LHC.

gluon gluon fusion	$gg \rightarrow H$
vector boson fusion	$q\bar{q} \rightarrow Hqq$
associated production	$q\bar{q} \rightarrow WH, ZH$
associated production with top quarks	$gg, q\bar{q} \rightarrow t\bar{t}H$

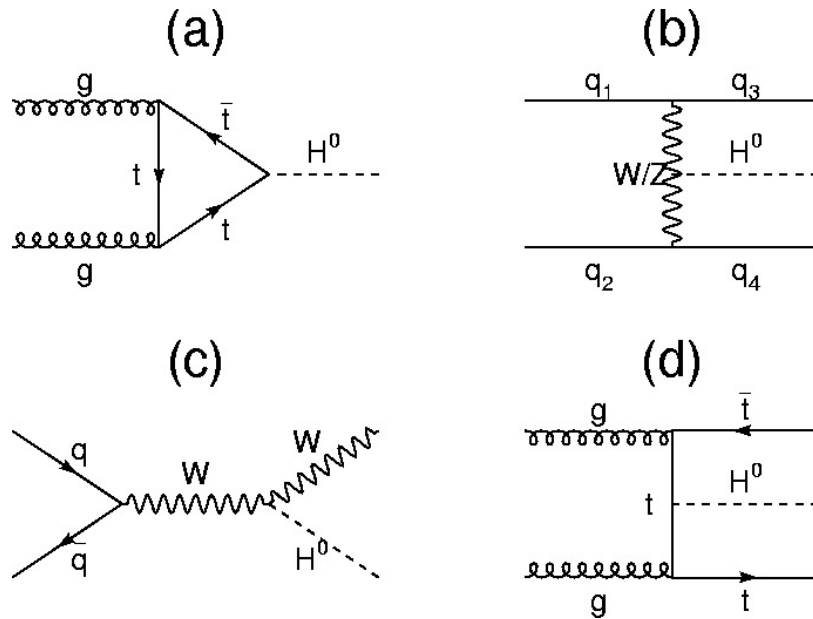


Figure 1.6. The most important processes for Higgs production at hadron colliders. Gluon fusion (a), vector boson fusion (b), Associative production with W (c) and an example of the diagrams having associative production with a top pair (d). [17]

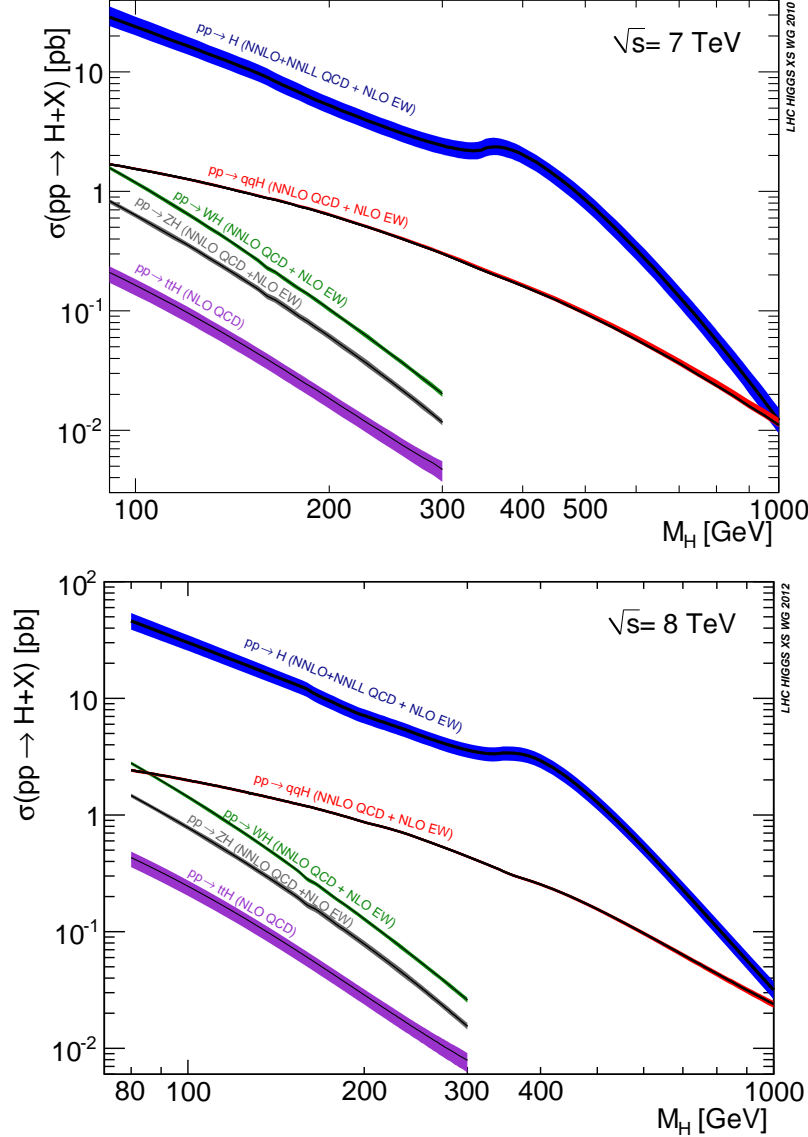


Figure 1.7. Standard Model Higgs boson production cross sections at $\sqrt{s} = 7, 8$ TeV. Transition for VBF at $M_H=300$ GeV at 8 TeV is due to change from ZWA to complex-pole-scheme. [18]

1.4.2 Higgs Decay

The Higgs boson can decay into a variety of other particles. The branching ratios of this decay are shown in Figure 1.8 [18]. From these images we can see that in the low mass region the most important decays are the fermions with $H \rightarrow b\bar{b}$. This

is most important because the b quark is the heaviest fermion into which the decay is kinematically allowed. As soon as it is possible to create vector boson pairs they begin to dominate the branching fraction. Also in the high mass region (above 350 GeV) $t\bar{t}$ pairs are created. An important thing to note is that the best Higgs decay channels are not only those with large branching ratios, but also those in which a good signal to background ratio can be achieved. There are three Higgs mass regions that have different properties in this respect.

In the low mass region ($m_H < 120$ GeV), even though the dominant decay is $H \rightarrow b\bar{b}$, the bb di-jet backgrounds make this channel extremely difficult to use. The most promising channel is the $H \rightarrow \gamma\gamma$. The reason this channel works well is because the signature is so clear and there are only the $q\bar{q} \rightarrow \gamma\gamma$ and the $Z \rightarrow e^+e^-$ backgrounds. In the mid mass region (120 GeV $< m_H < 135$ GeV) $H \rightarrow \gamma\gamma$ is still available but also $H \rightarrow WW^*, ZZ^*, Z\gamma$. The real winner of these is the $H \rightarrow ZZ^* \rightarrow 4\ell$ because even though it has a lower branching ratio than WW^* , it has a very clear decay signature and is able to fully reconstruct the Higgs mass. In the high mass region ($m_H > 135$ GeV) both the WW and ZZ channels begin to dominate. Despite the lower branching ratio of the $H \rightarrow ZZ$ decay, the clean signature allows good background rejection.

1.4.3 $H \rightarrow ZZ \rightarrow l^+l^-q\bar{q}$ Channel

In the high mass region for a Higgs boson discovery the predominant Higgs decay is to vector boson pairs, $H \rightarrow WW$ and $H \rightarrow ZZ$. The signatures from the fully leptonic decay modes for these two processes are easily reconstructible and can be distinguished from the background processes. The fully leptonic decay modes are $H \rightarrow WW \rightarrow l^+\nu l^-\bar{\nu}$ and $H \rightarrow ZZ \rightarrow l^+l^-l^+l^-$. The $H \rightarrow ZZ \rightarrow l^+l^-l^+l^-$ channel is particularly interesting because the decay chain can be fully reconstructed with a narrow invariant mass peak and almost no Standard Model background. The rate of

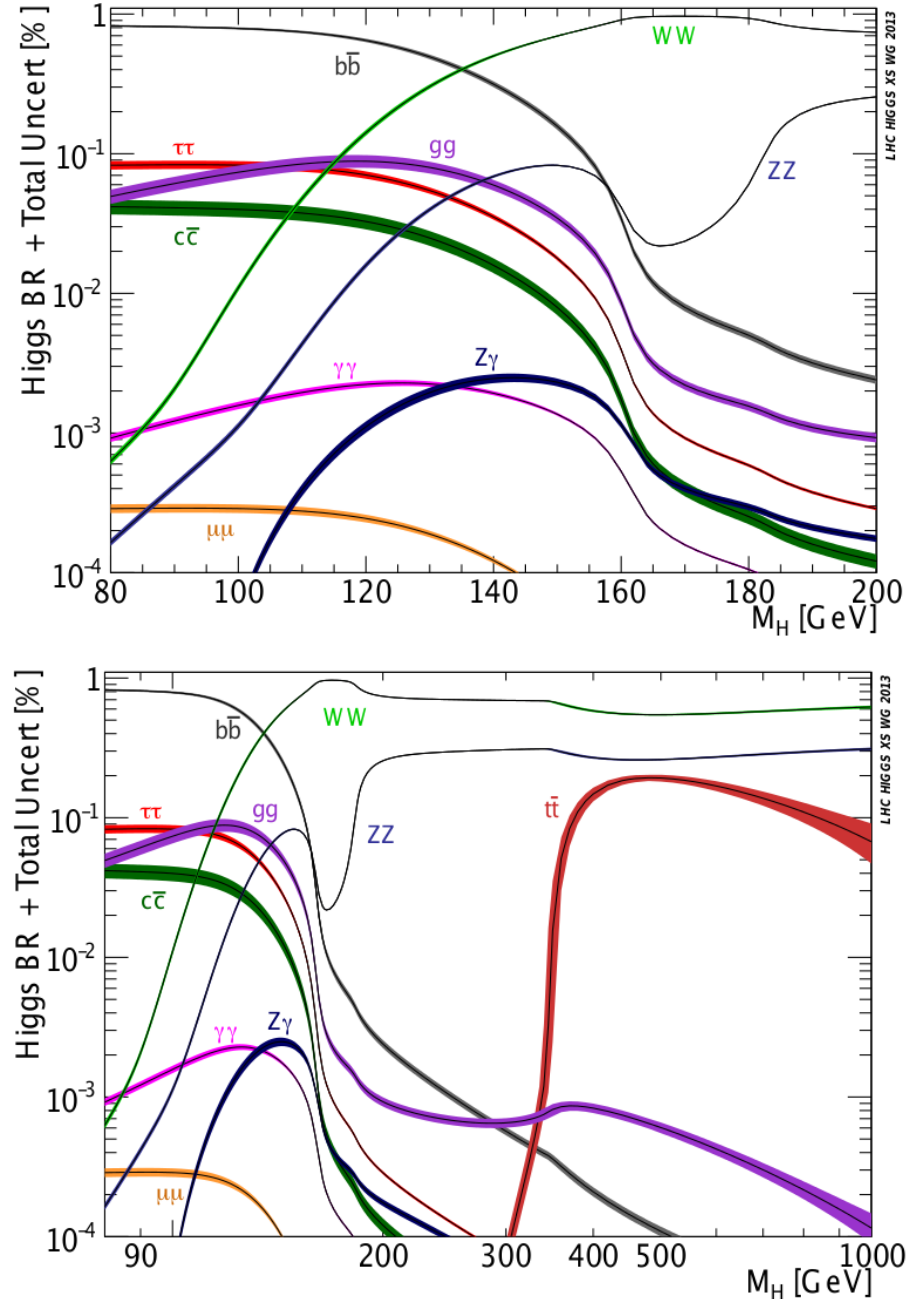


Figure 1.8. Standard Model Higgs boson decay branching ratios for two different m_H ranges. [18]

decay of $Z \rightarrow l^+l^-$ is only 3.37% [19] so for $l = e, \mu$ there is only a 0.45% chance of $ZZ \rightarrow l^+l^-l^+l^-$.

The largest Z branching ratio is 69.9% for $Z \rightarrow q\bar{q}$ [19]. Furthermore, $ZZ \rightarrow q\bar{q}q\bar{q}$ has a decay probability of just under 50%. The problem is that while this maximizes the branching ratio, this final state is indistinguishable from Standard Model background processes, like QCD.

The semi-leptonic final state in $H \rightarrow ZZ \rightarrow l^+l^-q\bar{q}$ produces a number of benefits over the previous two decay channels. The branching ratio of $ZZ \rightarrow l^+l^-q\bar{q}$ is 9.4%, or more than 20 times as large as $ZZ \rightarrow l^+l^-l^+l^-$. This can be seen in the plots of Higgs decay cross section multiplied by the final state branching ratio for both 7 TeV and 8 TeV in Figure 1.9 [18]. In comparison to $ZZ \rightarrow q\bar{q}q\bar{q}$ the leptonic decay of one of the Z bosons significantly reduces the Standard Model background in the final state.

Some of the difficulties in this channel compared to the fully leptonic decay are increased difficulty in event selection, the final reconstruction efficiency is approximately half of the fully leptonic final state, the backgrounds are significantly higher and dominated by Z+jets final states, and the resolution is worse. Despite these difficulties, this channel has improved sensitivity over the fully leptonic final state at high masses because of the higher branching ratio that the semi-leptonic final state enjoys, and at high masses the Z+jets background is not as significant.

$l^+l^-q\bar{q}$ Background Contamination

The background processes for this channel are processes which have a pair of oppositely charged leptons with large transverse momentum that are associated with two jets. The main backgrounds are listed in Table 1.6.

The dominant background in the $H \rightarrow ZZ \rightarrow l^+l^-q\bar{q}$ analysis is the Z+jets background, or more specifically, the inclusive Z production with QCD jets. The cross section of Z production at the LHC is more than 10^4 larger than the Higgs signal.

Table 1.6

The main Standard Model background processes for the $H \rightarrow ZZ \rightarrow l^+l^-q\bar{q}$ channel and their cross sections at 8 TeV [20].

Background Process	Cross Section [pb] at 8 TeV
$Z + jets$	3503.71
$t\bar{t}$	225.197
ZZ	17.654
WZ	22.88
WW	57.1097

Events containing top quarks are another significant source of background. There are two top processes that result in the same final state as the signal we are studying. They include $t\bar{t}$ pair production and top quark associated production with a W boson.

$$t\bar{t} \rightarrow (W^+ \rightarrow \ell^+\nu)b(W^- \rightarrow \ell^-\bar{\nu})\bar{b}$$

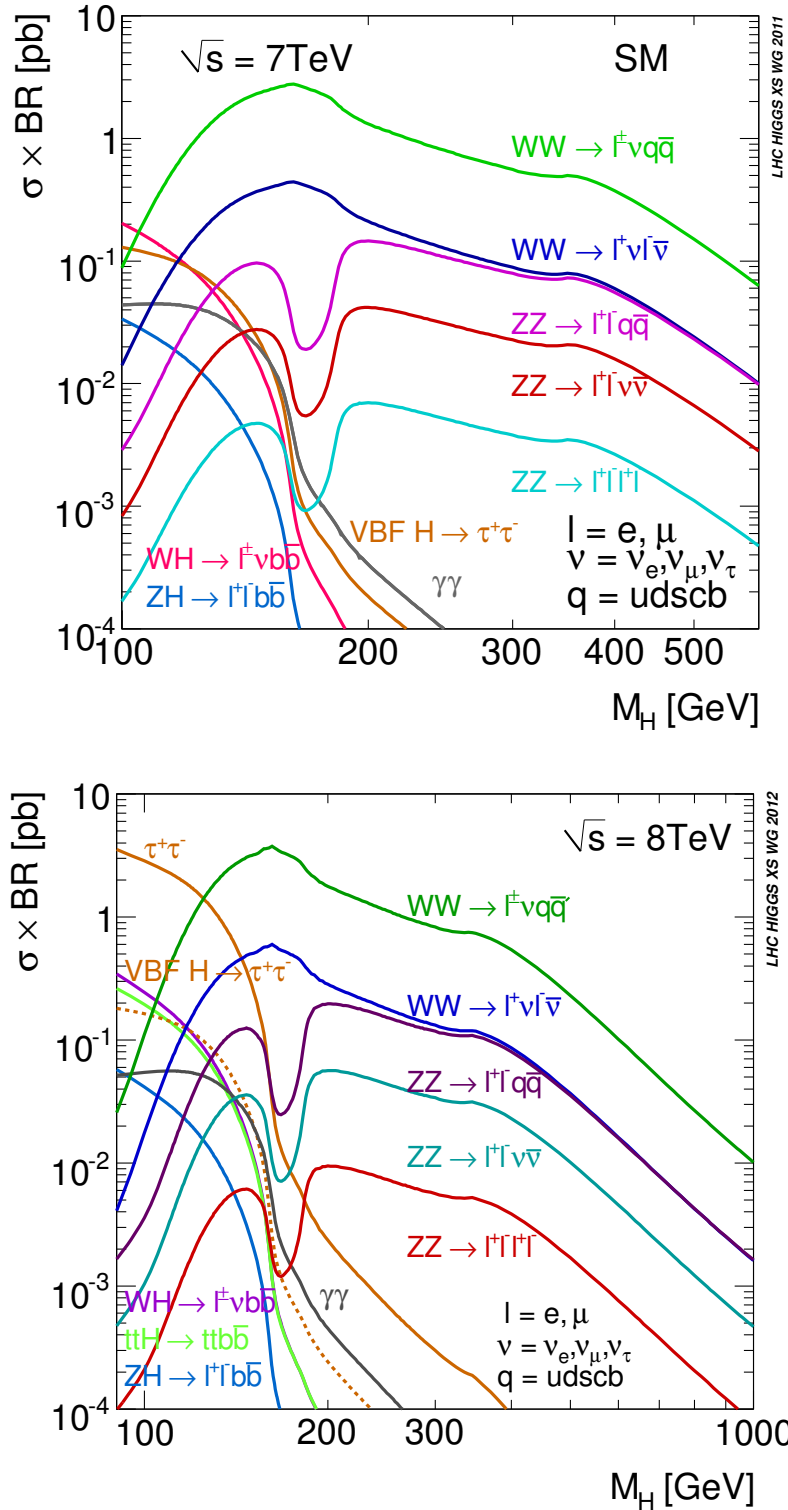


Figure 1.9. Standard Model Higgs boson production cross section times branching ratio at $\sqrt{s} = 7$ TeV and 8 TeV. [18]

2. Experimental Apparatus

This chapter describes the Large Hadron Collider (LHC) and the Compact Muon Solenoid (CMS) detector.

2.1 The Large Hadron Collider

Some of the parts of the Standard Model that we do not fully understand are the electroweak spontaneous symmetry breaking and the Higgs field. As referred to in the previous sections, direct searches for the Higgs boson in the past have failed. The verification of the full Standard Model, including the discovery of the Higgs boson, is one of the main goals of physics. Despite this being an important goal, the LHC has many other processes that it is sensitive to, including new physics. Figure 2.1 shows the predictions for some important Standard Model cross sections at $p\bar{p}$ and pp colliders [21].

The LHC accelerator is 26.7 km long and occupies the tunnel where the LEP collider was originally built. This tunnel is located approximately 100 meters underground and spans the French and Swiss boarders near Geneva, Switzerland. It is a proton-proton collider. The LHC is the world's largest and most powerful particle accelerator [22].

The LHC injection starts with a linear accelerator to bring protons to 50 MeV. After the Proton Synchrotron (PS) accelerates them to 1.4 GeV, the Super Proton Synchrotron (SPS) then injects the protons into the LHC at an energy of 450 GeV. To finish, the LHC increases the energy 0.5 MeV per cycle until they are at 4.0 TeV. This can be seen schematically in Figure 2.2 [23]. The LHC can also accelerate lead ions.

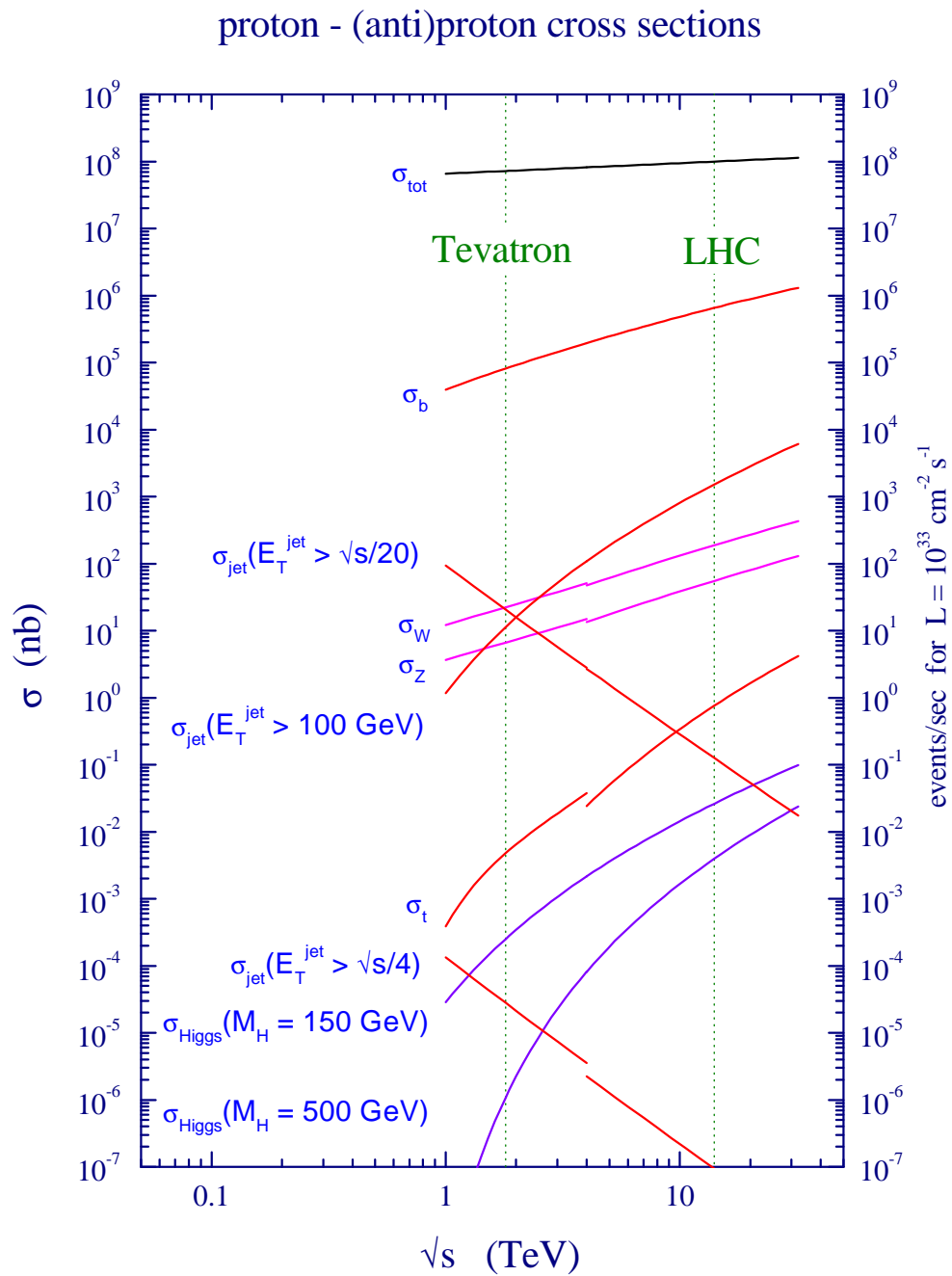


Figure 2.1. Standard Model cross sections at the Tevatron and LHC colliders. [21]

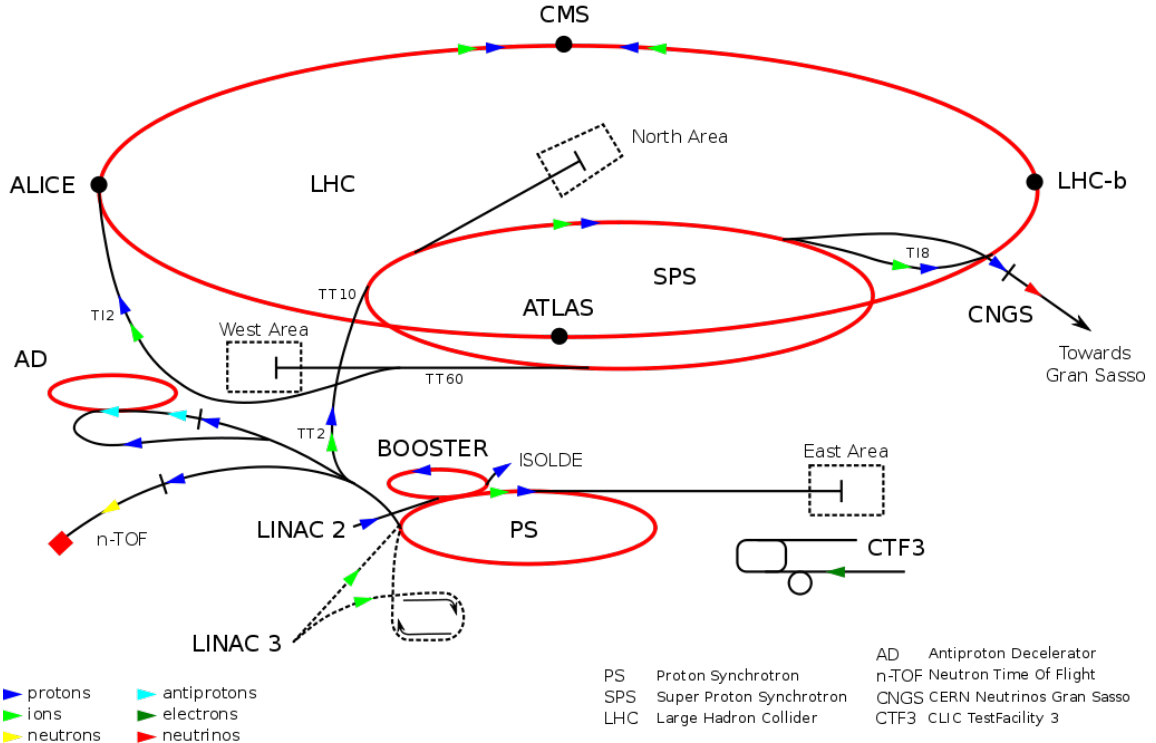


Figure 2.2. Map of the CERN accelerator complex. [23]

Because the protons being collided have the same electric charge, there are two vacuum chambers for acceleration with two different magnetic fields. There are 1,232 superconducting Niobium-Titanium magnets. Each one is 14.2 meters long and is cooled to 1.9 K with liquid Helium. The magnetic field produced is approximately 8.3 Tesla. These magnets are placed in 8 separate curved sections.

There are 4 interaction points in the LHC. Two are high luminosity points at the general purpose experiments of A Toroidal LHC Apparatus (ATLAS) [24] and CMS. The other two are for the A Large Ion Collider Experiment (ALICE) [25] and LHCb [26] experiments. These experiments can be seen in Figure 2.3.

On November 23, 2009, the first proton-proton collisions were generated. After a few runs at 450 GeV and 1.18 TeV beam energies, the first 7 TeV center-of-mass energies were achieved on March 30, 2010. This was the highest ever reached at a man-made particle collider. At 7 TeV approximately 47 pb^{-1} of integrated luminosity

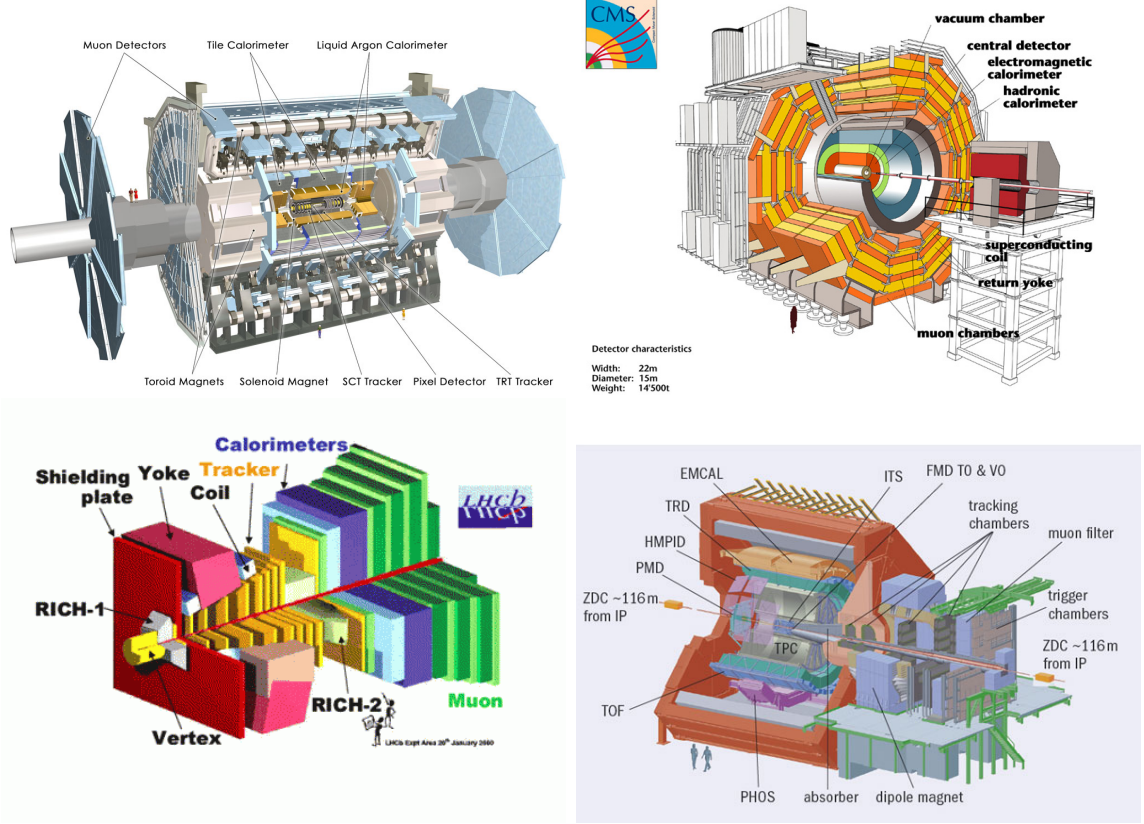


Figure 2.3. Top left: ATLAS experiment [27]. Top right: CMS experiments [28]. Bottom left: LHCb experiment [29]. Bottom right: ALICE experiment [30].

were delivered in 2010 (see Figure 2.4). The maximum instantaneous luminosity was $2 \times 10^{32} \text{ cm}^{-2} \text{s}^{-1}$.

During 2011 the machine was only off line for short amounts of time. On October 26, 2011 the highest ever instantaneous luminosity was reached with a peak value of $3.5 \times 10^{33} \text{ cm}^{-2} \text{s}^{-1}$. This was 1,331 bunches per beam with collisions every 50 ns. The total integrated luminosity delivered was 5.73 fb^{-1} (see Figure 2.4). In 2012 the beam energy was increased to 4 TeV and the LHC continued to perform amazingly, ultimately delivering over 23 fb^{-1} (see Figure 2.4).

In the coming years the LHC will continue to increase its energy and instantaneous luminosity. Eventually it will reach larger energies around 13 TeV collisions and

an instantaneous luminosity of $10^{34} \text{ cm}^{-2} \text{s}^{-1}$. This is seven times the energy of the highest Tevatron energy and two orders of magnitude more luminosity of any previous experiment.

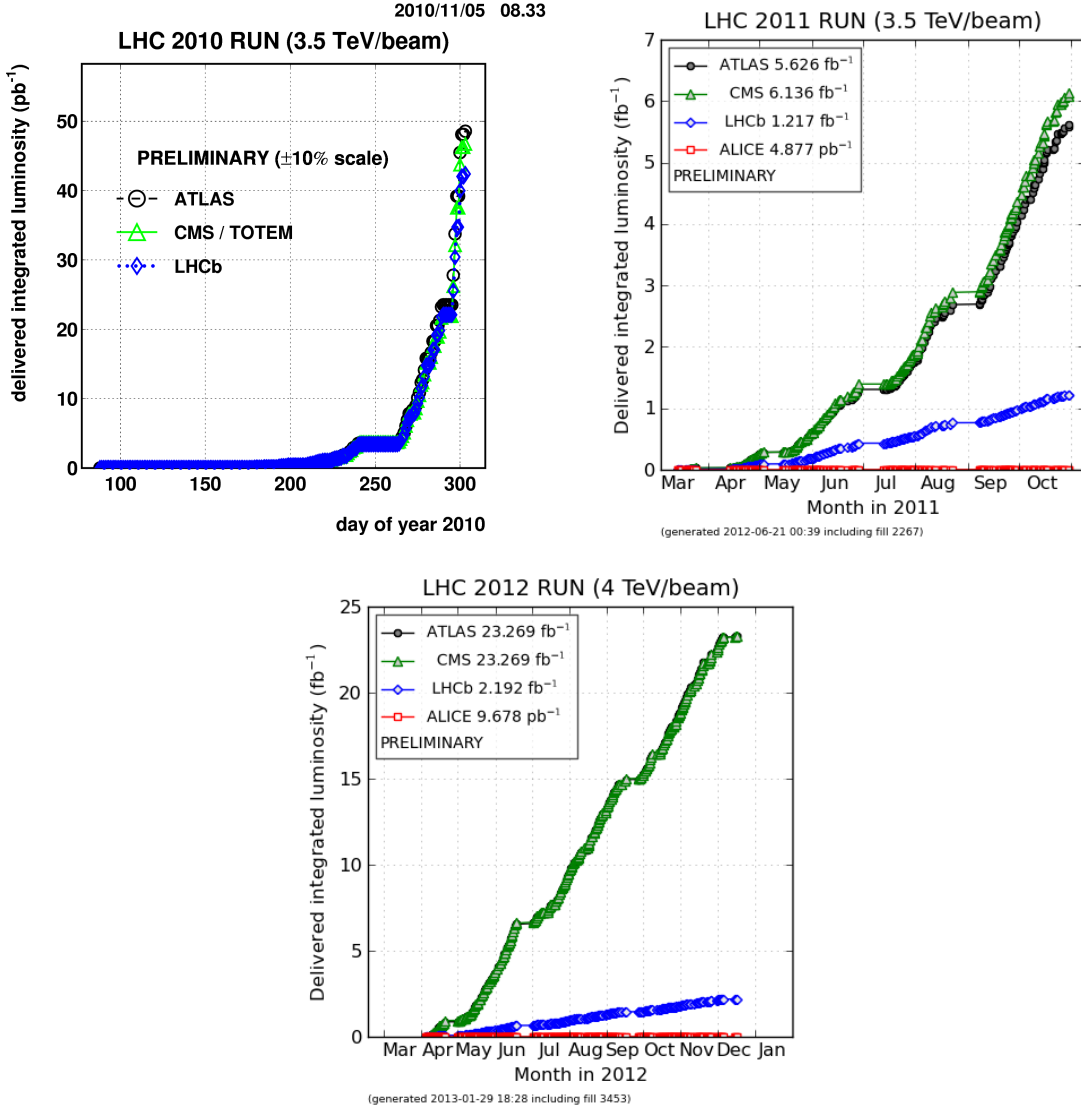


Figure 2.4. Integrated luminosity delivered by the LHC to each experiment in 2010 to 2012. [31]

2.2 The Compact Muon Solenoid

As one of the two general purpose detectors at the LHC, the Compact Muon Solenoid (CMS) has a wide range of physics goals, with its main focus on the Higgs boson search. Also important are physics beyond the Standard Model, precision measurement of known physics processes, and more. With these goals in mind, there are a number of requirements that a detector must have that are present in the CMS detector [32]. These are summarized below:

- High efficiency in muon, electron, and photon identification with excellent momentum resolution in the pseudo-rapidity region $|\eta| < 2.5$.
- Mass Resolution of approximately 1% for di-muon, di-electron, and di-photon events.
- The ability to determine the charge of muons and electrons.
- Charged particle momentum resolution and reconstruction efficiency in the inner tracker.
- Ability to identify the primary and secondary vertices for off line tagging b-jet and τ .
- π_0 rejection and efficient photon and lepton isolation.
- High performance trigger system to reduce the event rate to amounts that can be stored in real-time.
- A tracking detector with sufficient precision to limit the effects of event pile-up.

The main parts of the CMS detector include the 3.8 T superconducting solenoid, muon system, electromagnetic calorimeter, and the tracking system [33]. The CMS experiment has a number of cylindrical layers which are perpendicular to the beam axis (these are referred to as the barrel), and at both ends there are detector disks

which are orthogonal to the beam axis (referred to as the endcaps). A more detailed picture of the detector can be found in Figures 2.5 and 2.6. Figure 2.7 shows the data collection efficiency of the CMS detector for 2010 to 2012 [34].

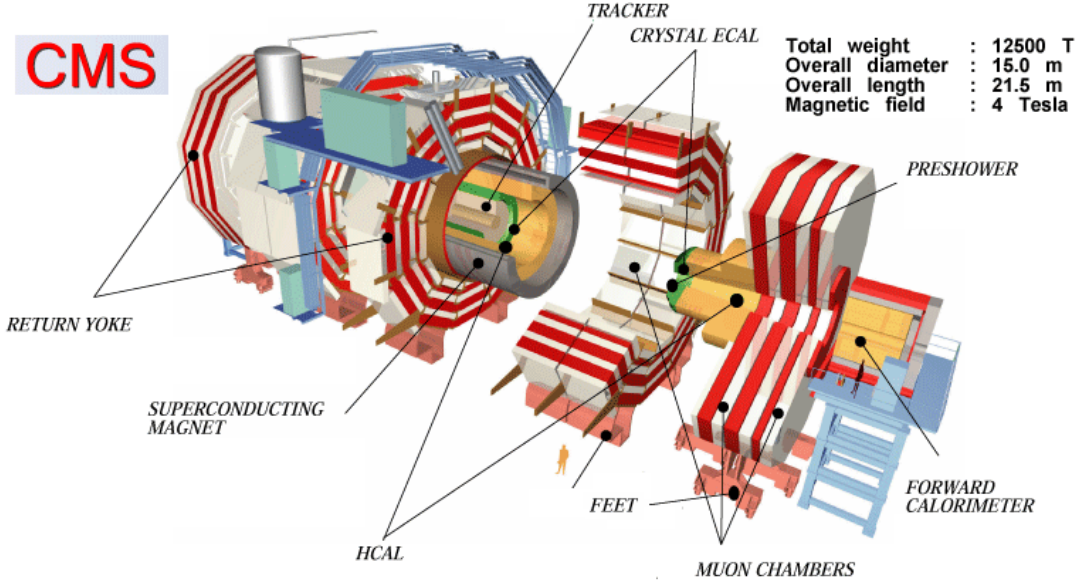


Figure 2.5. The CMS experiment. HCAL stands for hadron calorimeter and ECAL stands for Electromagnetic calorimeter.

2.2.1 CMS Subsections

In the following sections a coordinate system will be used as illustrated in Figure 2.8 [35]. Since the detector has a cylindrical shape around the beam axis, the beam axis is referred to as the z axis and a cylindrical coordinate system is used.

It is useful to use the projection of momentum in the transverse plain because the net transverse momentum of collisions is close to zero. We write:

$$E_T = E \sin \theta = \frac{E}{\cosh \eta} \quad (2.1)$$

When a particle is massless $E_T = p_T$. Similarly, for the energies considered, the masses are negligible and we assume that $E_T = p_T$.

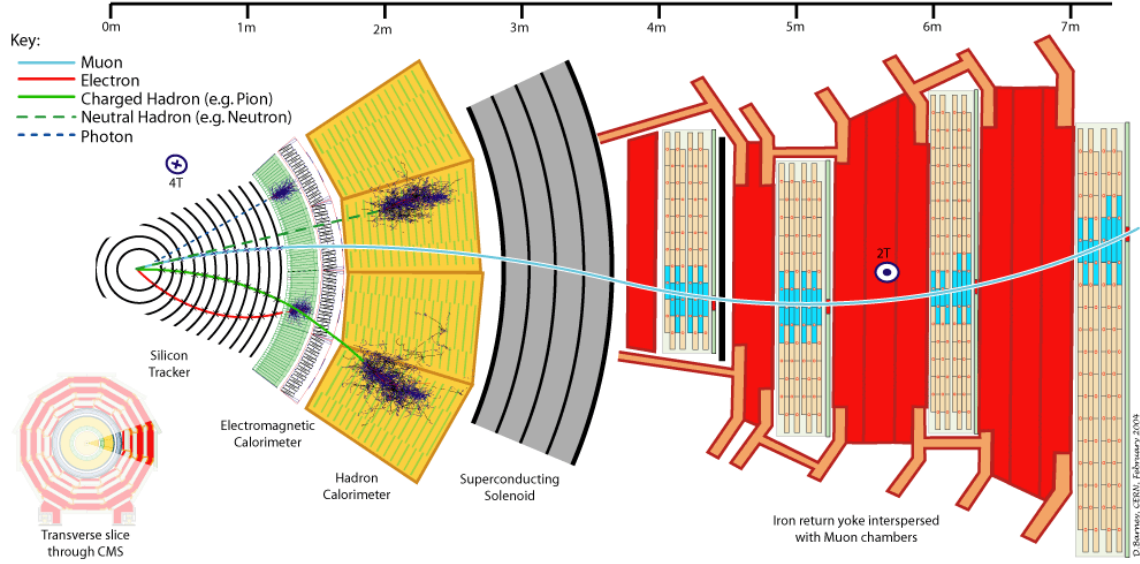


Figure 2.6. A graphical slice of the CMS experiment.

Magnet

To gain the resolution needed for the muon system, a large bending power of the detector is needed. One way to achieve this goal is to use a solenoid. The magnet in CMS is a 13 m long superconducting cylindrical Niobium-Titanium coil. This coil has a diameter of 5.9 m with a uniform magnetic field of 3.8 T at its center. The magnetic flux is returned by a double duty iron yoke support structure [36]. This magnet can be seen in Figure 2.9 [37].

Tracker

The tracker is the detector system that is closest to the primary interaction. Its primary goal is to reconstruct the tracks of charged particles with extremely high precision both in position and momentum. The goal is greater than 95% for electrons and muons and greater than 90% for jets. It is also able to identify both the primary and secondary vertices. Vertices are defined as the origin that a group of tracks share

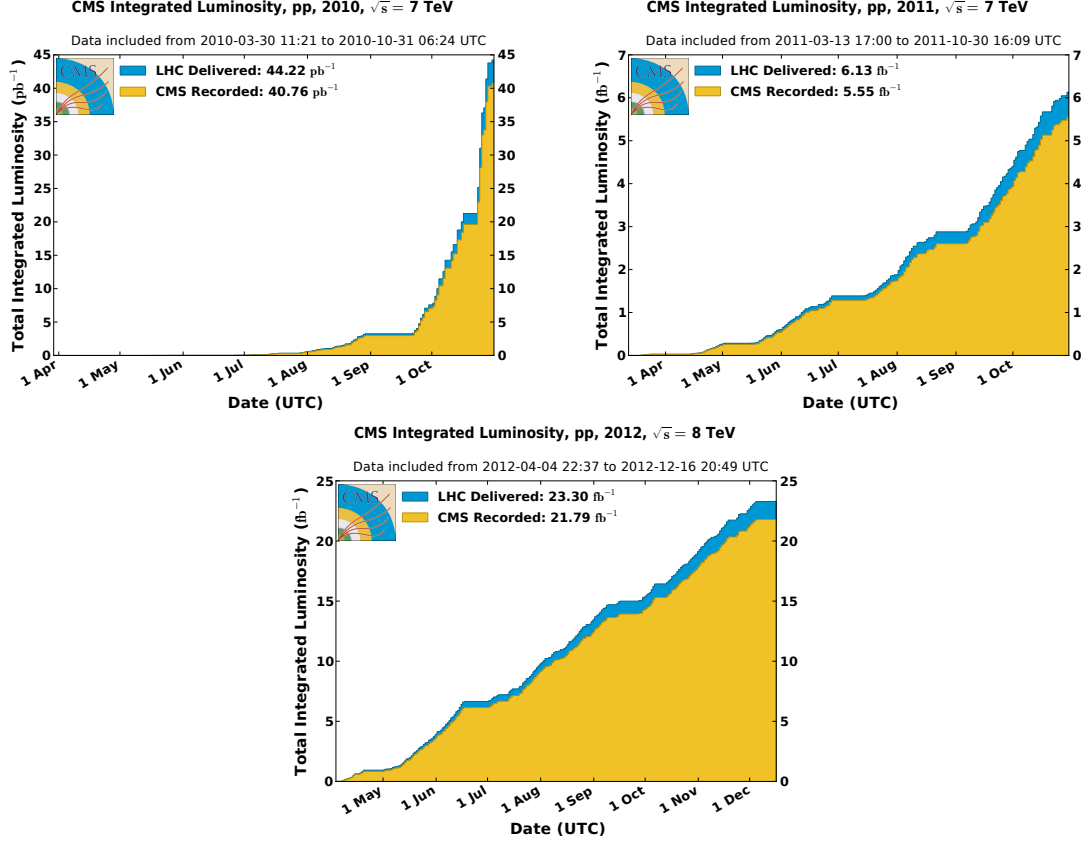


Figure 2.7. Total integrated luminosity for 2010 to 2012 delivered by the LHC and recorded by CMS. [34]

together. All these must be achieved in the extreme environment that is created by the LHC collisions [38].

The previous requirements facilitated the choice of using a large silicon tracker [38]. The tracker has three regions that are built differently because of the change in particle flux. The closest region is the pixel detector where the particle flux is at a maximum. In the intermediate regions, the flux has dropped sufficiently to be able to use silicon micro-strips. In the outer region, again the particle flux is even lower which allows larger silicon micro-strips to be used. This layout of the tracker can be seen in Figure 2.10 [39].

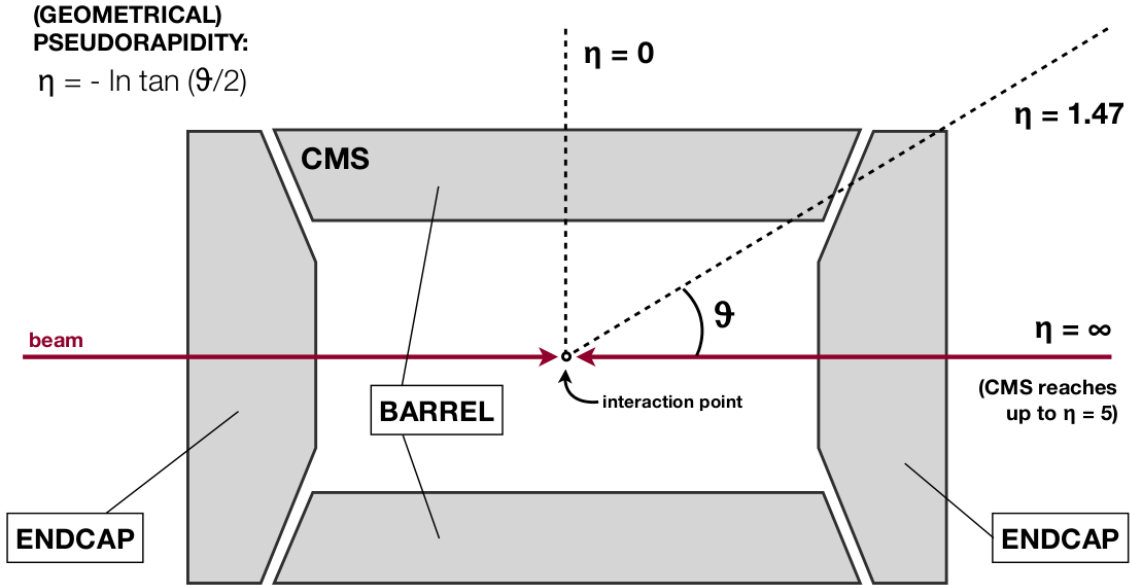


Figure 2.8. A CMS detector glossary of the cylindrical coordinate system used in this paper [35].

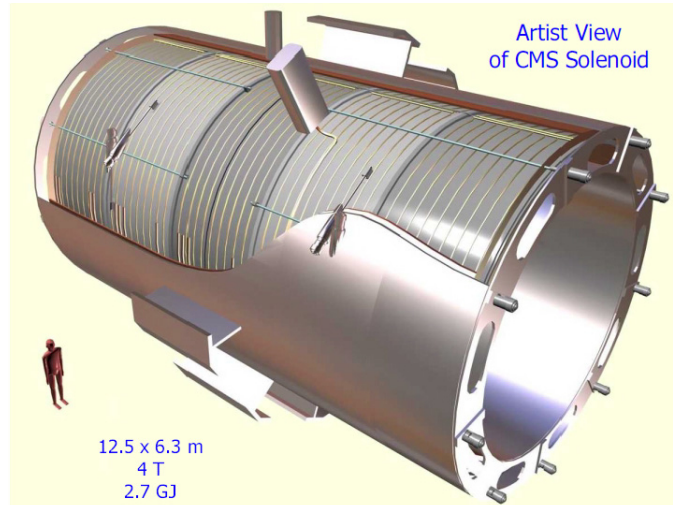


Figure 2.9. CMS solenoid magnet. [37]

The Calorimeters

The CMS detector has two calorimeters, an electromagnetic calorimeter and a hadronic calorimeter. The electromagnetic calorimeter allows the precise measure-

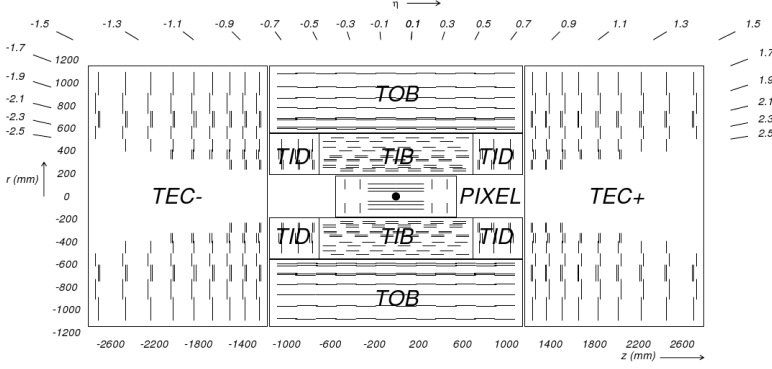


Figure 2.10. View of the CMS tracker in the rz-plane. Each line in the strip tracker represents a silicon strip detector, whereas lines in the pixel detector represent ladders and petals on which the detectors are mounted in the barrel and endcaps, respectively. [39]

ment of both photon and electron energies. The electromagnetic calorimeter is hermetic and homogeneous and made of 61,200 lead tungstate scintillating crystals in the barrel and 7,324 crystals in the two endcaps [40].

The lead tungstate crystals have a number of important features as listed below:

- Short radiation length (0.89 cm) that allows a compact calorimeter into the small space available.
- Very fast light emission (5 ns for primary and 15 ns for secondary) since LHC bunch crossings are 25 ns.
- Radiation hard at a level to allow several decades of high luminosity operation.
- Excellent position tracking because of the small shower containment.

One downside is that light yield is low and therefore photo detectors with a high gain must be used. Figure 2.11 [40] shows a longitudinal cross section of the ECAL. Any dead areas where there is not detection significantly degrades the total energy measurement and hurts the missing transverse energy (MET) calculations. Figure 2.12 shows the gap which was designed to minimize these problems [40]. The

overlap region $1.4442 < |\eta| < 1.566$ is excluded for certain measurements in the analysis for electrons.

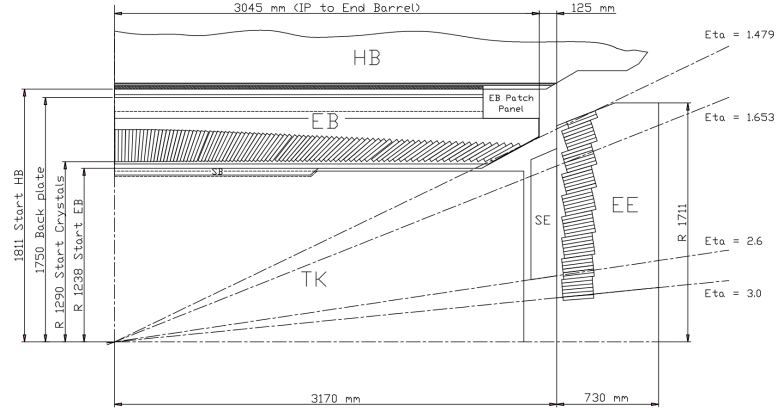


Figure 2.11. Longitudinal section of the electromagnetic calorimeter (one quadrant). [40]

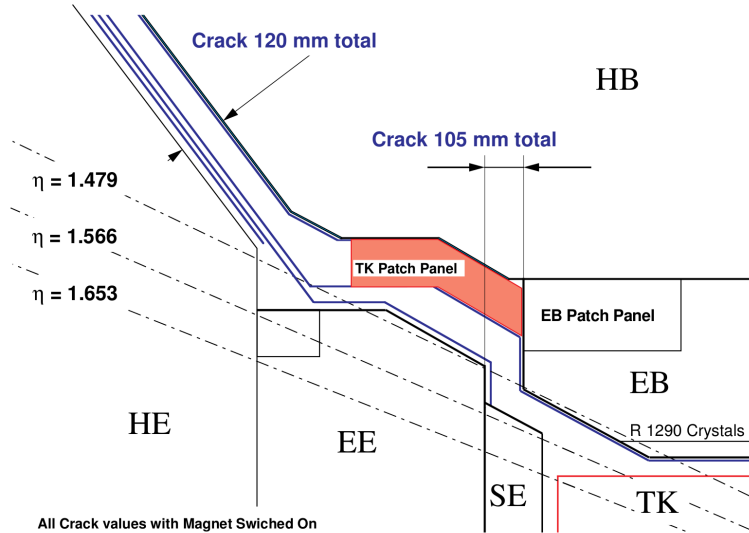


Figure 2.12. The barrel and endcap transition region. [40]

The hadronic calorimeter [41] detects quarks, gluons, and neutrinos. This is done by measuring the energy and position of particle jets as well as the missing transverse energy (MET). In conjunction with the other systems, it also helps with the

identification of electrons, photons, and muons with the ECAL and muon systems. The central hadron calorimeter is a sampling calorimeter. The hadron calorimeter is made of 4mm thick plastic scintillator tiles. It uses brass as the absorber material. A quarter slice of the HCAL can be seen in Figure 2.13 [42].

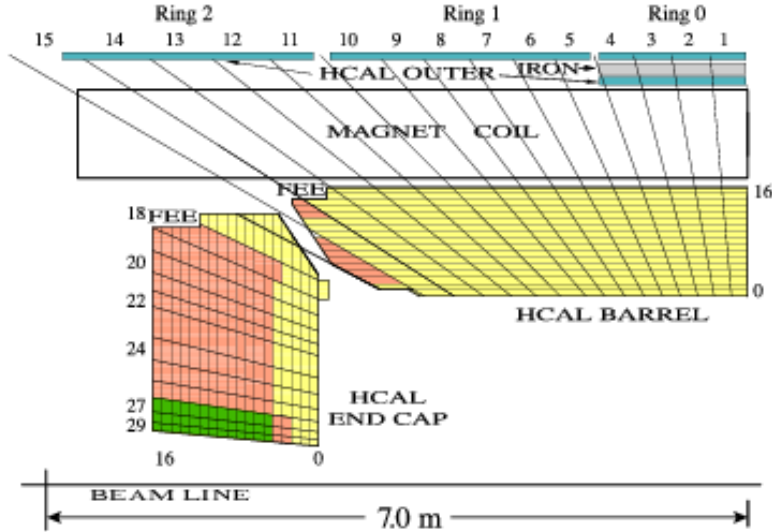


Figure 2.13. A quarter slice of the CMS HCAL detectors. The right end of the beam line is the interaction point. FEE denotes the location of the Front End Electronics for the barrel and the endcap. In the diagram, the numbers on the top and left refer to segments in η , and the numbers on the right and the bottom refer to scintillator layers. Colors/shades indicate the combinations of layers that form the different depth segments, which are numbered sequentially starting at 1, moving outward from the interaction point. The outer calorimeter is assigned depth 4. [42]

2.2.2 The CMS Trigger System

At the high luminosity achieved at the LHC, there is the drawback that several of the interactions overlap in the same bunch crossing. Also there is overlap from different bunch crossing because of the limited speed of the detector response and data read-out. These effects are known as pile-up. In addition to pile-up difficulties,

there is an extreme amount of data produced from the collisions at CMS. With a luminosity of $10^{34} \text{ cm}^{-2} \text{ s}^{-1}$, there are roughly 10^9 interactions per second. With the typical event size of 1 MB, all collisions cannot be recorded and with the majority of interactions not interesting for the CMS physics program, there needs to be a way to choose which events to record. This is done with the triggering system to reduce the recorded rate to approximately 100 Hz. There are technical difficulties in the handling, processing, and storing of this data. These difficulties make the real time selection and recording of important events (the trigger) very important [43].

The CMS trigger has two levels. The Level 1 (L1) trigger is a hardware trigger. The full data is stored in the pipelines for processing while waiting for the trigger decision. If the L1 accepts the decision, then the data is moved to the software based High Level Trigger (HLT). The HLT reduces the output rate to around 100 Hz. The HLT software has a set of algorithms which give complete freedom in deciding which data to access. To free up processing, there are three virtual trigger levels. The first only uses the muon and calorimeter data, the second adds the pixel seeds, and the final step uses the full event information. Both L1 and HLT triggers have changed as the LHC environment changed during the luminosity increases.

The Level 1 trigger is used to choose hard scattering from processes like Higgs decays, WW scattering, supersymmetry, and more. This system is based on custom electronics. It uses the identification of photons, electrons, muons, jets, and missing transverse energy. A diagram of the L1 trigger system is shown in Figure 2.14 [43]. The physics requirements for the L1 trigger are as follows [43]:

- The CMS trigger system should be capable of selecting leptons and jets over the pseudo-rapidity range $|\eta| < 2.5$, with an efficiency which is very high, above a selected threshold in transverse momentum.
- For the single lepton triggers, it is required that the trigger is fully efficient ($> 95\%$) in the pseudo-rapidity range $|\eta| < 2.5$, with a threshold of $p_T > 40 \text{ GeV}$.

- For the dilepton trigger, it is required that the trigger is fully efficient ($> 95\%$) in the pseudo-rapidity range $|\eta| < 2.5$ with thresholds of $p_T > 20$ and 15 GeV for the first and second leptons respectively.
- Single photon and diphoton triggers are required to have thresholds similar to those of the leptons.
- Single and multiple jet triggers are required with a well defined efficiency over the entire rapidity range $|\eta| < 5$ in order to reconstruct jet spectra that overlap with data attainable at lower energy colliders, such as the Tevatron. For higher transverse momenta, the jet trigger should also be fully efficient.
- A missing transverse energy trigger with a threshold of about 100 GeV is required.

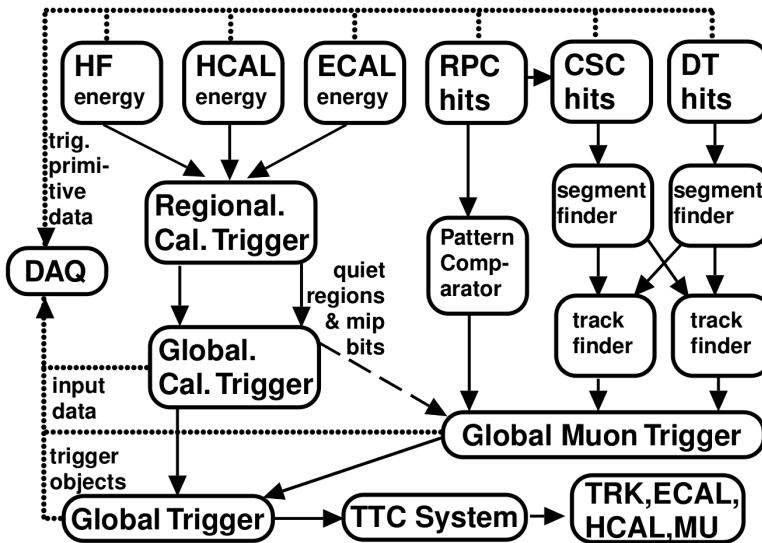


Figure 2.14. Overview of Level 1 Trigger. [43]

The High-Level trigger is a software system with maximum flexibility for selection and the changing environment of the LHC [44]. It takes the output from the Level 1 trigger to do a rough event reconstruction. With this rough reconstruction the HLT

makes the decision to either reject the event or pass it through to a more detailed reconstruction. This is decided by a number of criteria that are collectively used to create data sets. These are designed to meet the various physics' goals that CMS was designed to study. Common requirements are high p_T lepton pairs, or large amounts of MET.

3. Electron, Muon, and Jet Reconstruction

3.1 Electron Reconstruction

Electrons are reconstructed from the tracks they form in the silicon tracker and from their energy which is deposited in the ECAL. An electron passing the silicon tracker loses energy through ionization and the emission of a photon (this process is called bremsstrahlung). This energy loss has to be taken into account. Electron reconstruction needs to join both the tracks in the tracker and the energy deposit in the ECAL while successfully identifying the particle as an electron. All this must happen while being careful not to identify other charged particles (like pions) as electrons. A particle incorrectly identified as an electron is called a fake electron. To take this and other problems into account, there are two different clustering algorithms that are used [45].

The energy that is collected in the calorimeter is grouped together into super-clusters. This is done along the ϕ direction by taking the most energetic cluster and collecting the other nearby clusters together. Once a super-cluster is created, a minimum of two hits is needed in the pixel detector in order to start the electron trajectory reconstruction. Using the trajectory, momentum, and the loose geometrical matching with the super-cluster, the tracks are matched to the appropriate super-cluster. There are four different electron classes that are corrected in different ways for bremsstrahlung and other effects. The four types are as listed [46]:

- Golden electrons. This class represents electrons least affected by radiation emission, with a reconstructed track that matches the super-cluster.
- Big Brem electrons. This class contains electrons with a good match between the energy calculated in the super-cluster algorithms and the momentum recorded

coming in, but the super-cluster does not directly match with the reconstructed track. Also, there must be no energy loss effects from secondary photon conversion. Electrons for which all the bremsstrahlung is radiated in a single step can fall in this category.

- Narrow electrons. In this intermediate class, electrons have a large bremsstrahlung fraction but not has high as Big Brem electrons. There is a well behaved super-cluster (i.e. the bremsstrahlung photons are merged inside a single cluster), but like Big Brem, it doesn't have a clean match between the tracks and the super-cluster.
- Showering electrons. This class contains electrons which failed to enter any of the above classes. It includes electron super-cluster patterns involving one or several identified bremsstrahlung sub-cluster(s), or cases where a bad energy-momentum E/p matching is observed. This is very likely in cases of secondary conversion of some early radiated bremsstrahlung for electrons having radiated a large fraction of their initial energy.

Once the electrons are corrected, the Gaussian-sum filter (GSF) algorithm for electron reconstruction is used to model the bremsstrahlung energy loss distribution by a Gaussian mixture rather than by a single Gaussian [47]. Further cuts can be done as part of an analysis or for preselection to reduce fake electrons.

3.2 Muon Reconstruction

In the CMS detector muon tracks are reconstructed both in the tracker and in the muon chambers. The muons must transverse a large amount of material before they reach the muon chambers, which lowers the resolution because of the scattering that has happened. This places a great importance on the tracker measurements both for the fine resolution and the intense magnetic field.

First, the muon tracks are reconstructed from the muon chambers. Then in a two step process these tracks from the muon chambers are linked to the corresponding tracks found in the tracker. First, a set of tracks that match the momentum and direction of the muon chamber tracks is found. After that, a matching algorithm is applied using kinematics and angular variables to find the most accurate tracker/muon chamber track pair.

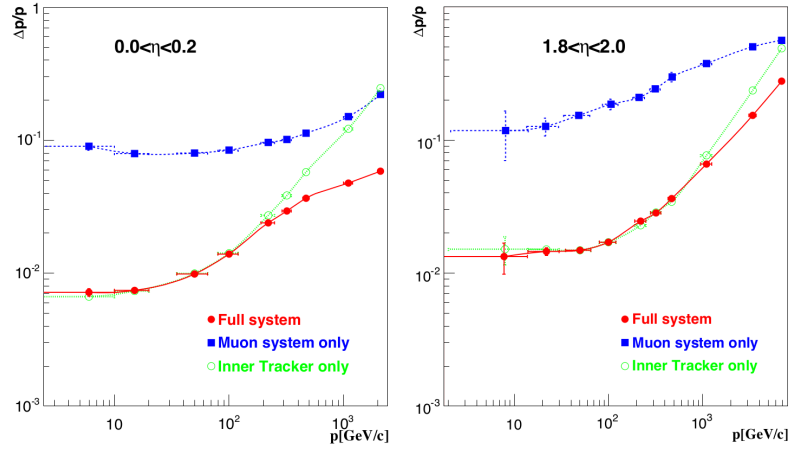


Figure 3.1. Muon momentum resolution when using the muon spectrometers only (blue), the tracker only (green), and the full system (red): barrel ($|\eta| < 0.2$) results are shown on the left, endcaps ($1.8 < |\eta| < 2.0$) on the right. [48]

A muon candidate made from the muon chambers and tracker information is called a global muon. If a global muon cannot be reconstructed, then using only the tracker information a tracker muon is created. Similarly, if only a track from the muon systems is found, it is reconstructed to be a stand alone muon. The High-Level trigger uses additional criteria for a selection, like isolation and momentum, to create datasets for later analysis.

3.3 Jet Reconstruction

At proton colliders, the reactions are primarily from the interaction of partons, which is the name given to the constituents that make up a hadron. Hadronization gives rise to columns of particles that we call jets. Jets are difficult for both theorists and experimental physicists because they are composite objects that cannot be uniquely specifically defined. The jet reconstruction that is used is based on how particle candidates cluster using the particle flow (PF) algorithms which are described below. This composite nature causes the detector response to vary jet to jet. This becomes a problem for the determination of the jet's energy and necessitates careful calibrations.

Light particles make up of the bulk of hadronization. The typical breakdown of a jets energy is as follows:

- about 65% of a jet energy is carried by charged particles, predominantly charged pions and kaons;
- 20% is converted into high-energy photons, mainly from the electromagnetic decay of neutral mesons such as π 's and η 's;
- the remaining 15% is stored in long-lived neutral hadrons, mainly neutral kaons, neutrons, and Λ baryons [48].

With only 20% of the jet energy being purely electromagnetic, the remaining measurements are taken through the hadronic calorimeter which leads to additional energy measurement difficulties.

The clustering of the particles that make up the jets is done with the anti- k_t algorithm. This algorithm is described in the following section.

We first define d_{ij} and d_{iB} [49]:

$$d_{ij} = \min(k_{ti}^{2p}, k_{tj}^{2p}) \frac{\Delta_{ij}^2}{R^2}, d_{iB} = k_{ti}^{2p} \quad (3.1)$$

$\Delta_{ij}^2 = (y_i - y_j)^2 + (\phi_i - \phi_j)^2$ and k_{ti} , y_i and ϕ_i are respectively the transverse momentum, rapidity, and azimuth of particle i . First we find the minimum of all the

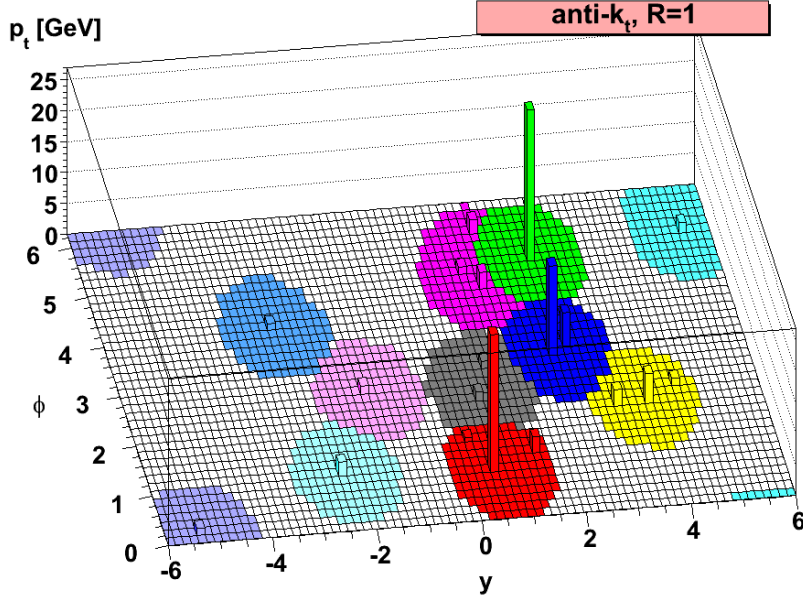


Figure 3.2. A sample parton-level event (generated with Herwig [50]), together with many random soft “ghosts”, clustered with the anti- k_t algorithm, illustrating the “active” catchment areas of the resulting hard jets. This shows the cylindrical jets all with radius of R=1 or less. [49]

distances d_{ij} and d_{iB} . If the minimum is one of the d_{iB} , then it is called a jet and if it is a d_{ij} , we combine i and j into a new particle by summing over the momentum. We continue to do this until we only have jets.

One of the benefits of this algorithm is that the distance parameter R only allows particles to be merged into jets of that specific radius or smaller. This also results in conical jets that have radius equal to or smaller than this distance parameter. This can be seen in figure 3.2 [49]. In this analysis the R value is 0.5.

3.4 Particle Flow Reconstruction

At CMS, particle-flow event reconstruction tries to reconstruct and identify all stable particles in the events. This includes all the electrons, muons, charged and

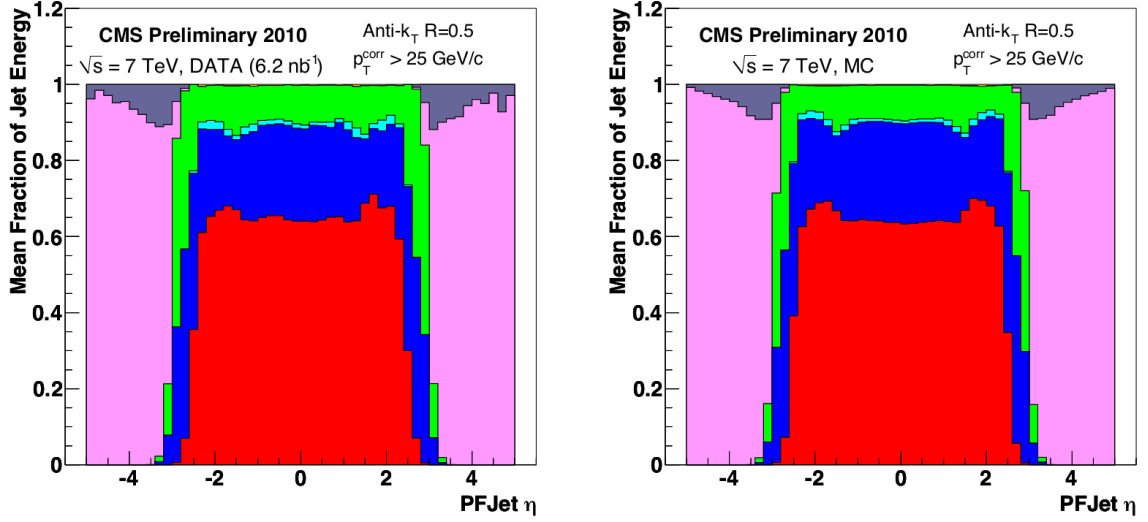


Figure 3.3. Reconstructed jet energy fractions as a function of jet pseudo-rapidity. In the central region, bottom to top: charged hadrons (red), photons (blue), electrons (cyan), neutral hadrons (green). In the forward region: HF hadrons (pink), HF electromagnetic particles (gray). [48]

neutral hadrons, and photons. It also uses information from all the sub-detectors like the tracker, both calorimeters, muon chambers, etc. After detection, these particles are used as if they were Monte Carlo generated events to build the jets, MET, taus, lepton isolation, tag b-jets, and more [51].

This is possible because the CMS detector has such a large silicon tracker fully immersed in the magnetic field and the large pseudo-rapidity range. This allows particle detection for particles that have a transverse momenta as low as 150 MeV. As previously mentioned, jet energy is only 15% in the hadronic calorimeter. Figure 3.3 [48] shows the energy fractions as a function of pseudo-rapidity for the reconstructed jets on MC simulation.

The Particle Flow algorithm works as follows. The hits in each part of the detector are independently reconstructed and formed into blocks. These include tracks in the tracker and calorimeter energy deposit clusters. After the blocks are formed, a linking algorithm connects the ones with compatible topology to create Particle

Flow Candidates (PFCandidates). There are various types of candidates as described below [52].

- Muons: a global muon, reconstructed from the combination of a track in the tracker and a track in the muon system, gives rise to a PF muon. After the identification, the corresponding track is removed from the block.
- Electrons: the link between a charged-particle track and one or more ECAL clusters identifies PF electrons. The corresponding track and ECAL clusters are removed from further processing.
- Charged hadrons: The remaining tracks give rise to PF charged hadrons and the momentum of the particle is taken directly from the track momentum. Tracks can be linked to ECAL and HCAL clusters if they are not identified as electrons, and the momentum is redefined taking into account information from calorimeters.
- Photons and Neutral hadrons: ECAL clusters not compatible with charged-tracks give rise to PF photons, while unaccounted HCAL deposits are interpreted as PF neutral hadrons.

When the full list of PFCandidates is populated, the PF Jets are reconstructed using the anti- k_t algorithm as described above. The traditional method of reconstructing jets is to use only the calorimeters. These jets are called Calo-Jets. The difference in the jets response given by the two algorithms can be seen in figure 3.4 [51]. As seen in these figures, Particle Flow jets have a higher response throughout the entire detector. Further, if we look at the reconstruction between the two types of jet algorithms as a function of the transverse momentum of the jets, we see an even more divergent picture. This can be seen in figure 3.5 [51]. The improvement due to the Particle Flow algorithm is impressive, particularly the large improvement at the lower end of the p_T spectrum.

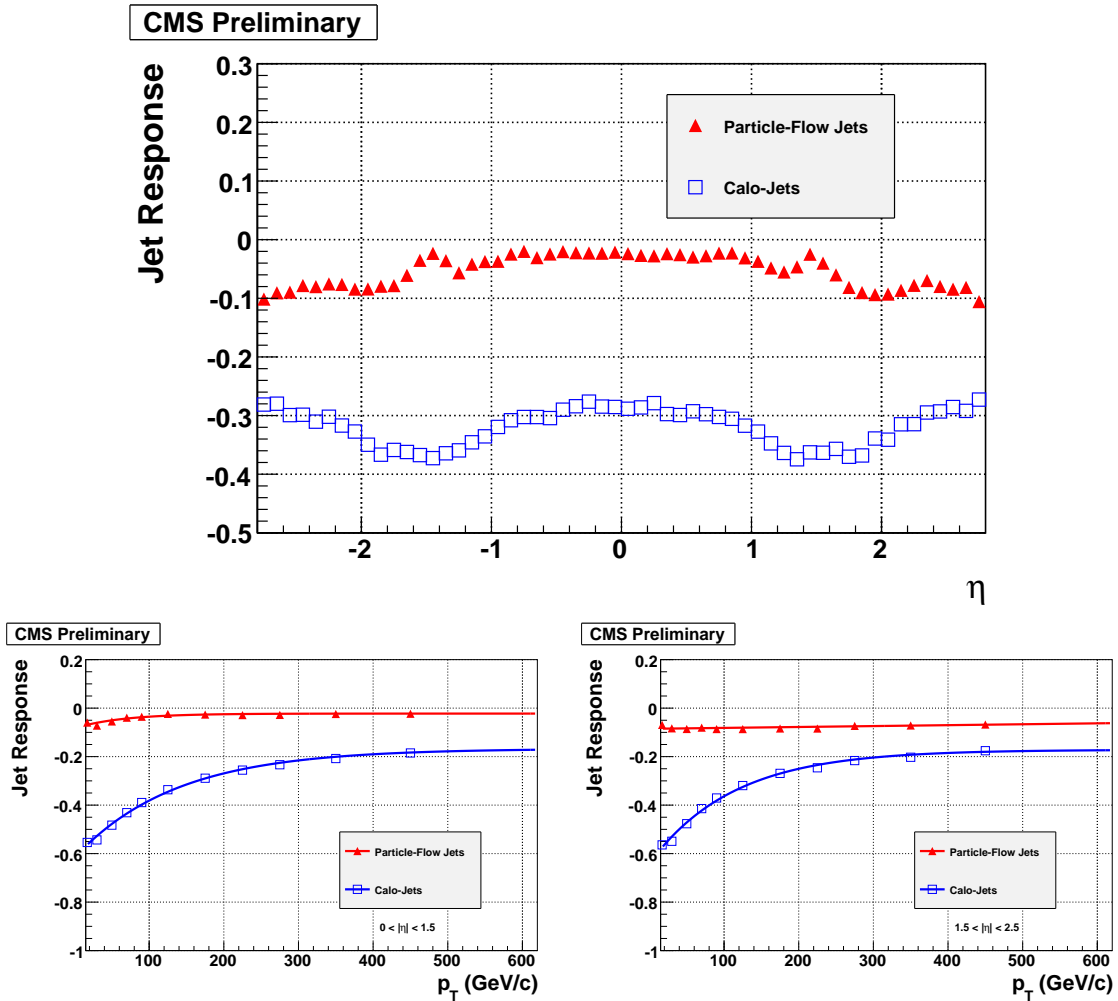


Figure 3.4. Jet response as a function of η integrated over all p_T 's below 750 GeV (top) and as a function of p_T , in the barrel (left) and in the endcaps (right). The response curves are fit with exponential functions of p_T . [51]

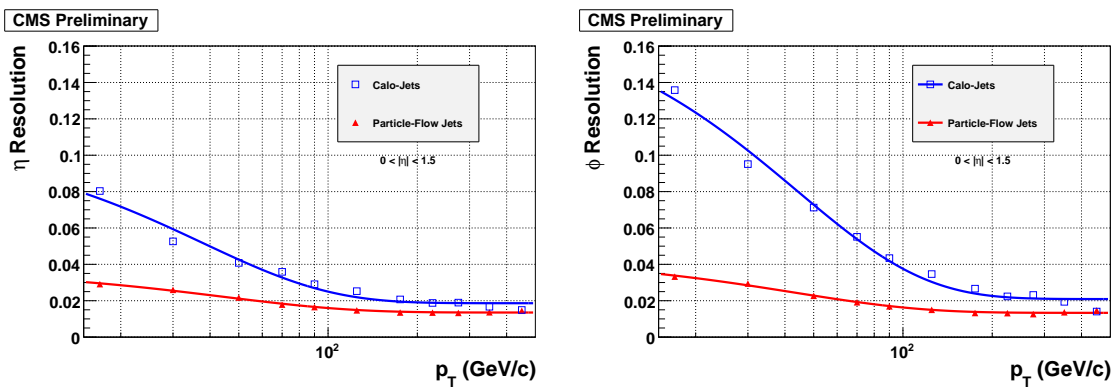


Figure 3.5. Jet-energy resolutions as a function of p_T for corrected calo-jets and for particle-flow jets (upwards triangles) in the barrel (left) and in the endcaps (right). The resolution curves are fit to the sum of a constant term, a stochastic term and a noise term. [51]

4. Event Selection

This Chapter outlines the event selection that we use for the analysis. A list and brief description is given of both the data and the Monte Carlo generated events. Also the cuts and motivation for the analysis preselection is given.

4.1 Datasets

The focus of this analysis is on a massive Higgs boson which is above the ZZ production threshold of 200 GeV. Because of this high energy, the decay of one of the Z bosons will produce a pair of high p_T leptons. This will primarily fire the double-lepton HLT paths and be stored in one of the two primary datasets: DoubleElectron or DoubleMuon. For 2012 we are using the double lepton primary datasets corresponding to 19.6 fb^{-1} at 8 TeV. The data samples for 2012 are listed in Appendix A. Each block of data undergoes data quality monitoring (DQM) both in real-time and after the data is recorded. Only the data recorded under good conditions for each sub-detector is certified. Subsequently, only data that is certified as good is used in this analysis. This analysis is done on the 2012 datasets but is combined with the previous results (2011) at the end.

The data that is used in this analysis is run over centrally produced datasets that are called primary datasets. Primary datasets are filled with events that pass the high-level triggers that are identified with that dataset. The three primary datasets that we are concerned with are the DoubleMu, DoubleElectron, and MuEG. The DoubleMu must have two muons that fire a specific muon HLT, DoubleElectron must fire two specific electron HLT, and MuEG must have an electron and muon that fire one of the MuEG HLTs. More details will be given later in this chapter.

4.1.1 Simulated Events

Monte Carlo (MC) simulations are useful for studying the properties of the SM Higgs boson and the backgrounds that are relevant to this analysis. The dominant background in this analysis is the inclusive Z production with jets. Particularly those jets coming from b-quarks. The Z+Jets sample uses the MADGRAPH generator [53]. MADGRAPH is a Next-to-Leading-Order (NLO) matrix element generator. Other backgrounds are $t\bar{t}$, ZZ, WW and WZ. The main portion of the top background is from $t\bar{t} \rightarrow 2l2\nu2b$ and the sample for this is generated using POWHEG [54–56] which is interfaced with PYTHIA 6 [57] to do the final parton showering and hadronization. For ZZ, WZ, and WW, they are fully generated with PYTHIA 6. The Monte Carlo samples for these processes are listed in Appendix A.

The signal Monte Carlo samples used in this analysis were generated using POWHEG and vary for M_H from $230\text{ GeV}/c^2$ up to $1000\text{ GeV}/c^2$. These samples can also be seen in Appendix A. Each sample has 3×10^{-5} events. The cross-sections multiplied by the branching ratio for $H \rightarrow ZZ \rightarrow 2l2q$ are listed as well. The $H \rightarrow ZZ$ branching fraction is provided as a function of the Higgs boson mass by the LHC Higgs cross section working group [58, 59]. The branching ratios of $Z \rightarrow \ell^+\ell^-$ and $Z \rightarrow q\bar{q}$ are from the Particle Data Group (PDG) [60]. These numbers can be found in Appendix A.

4.2 Pile-Up

In the extreme intensities at the LHC, many pp interactions overlap each other. These extra interactions are known as pile-up with respect to the interaction of interest. When simulations are generated, the pile-up conditions of the detector are one of the input parameters, but these conditions can change and produce a mismatch between Monte Carlo and data. To correct this, we use scale factors to re-weight the simulated events in both the muon and electron channels [34]. The 2012 distributions and their corrections can be seen in Figure 4.1. All following sections have the pile-up re-weighting applied to all simulated samples.

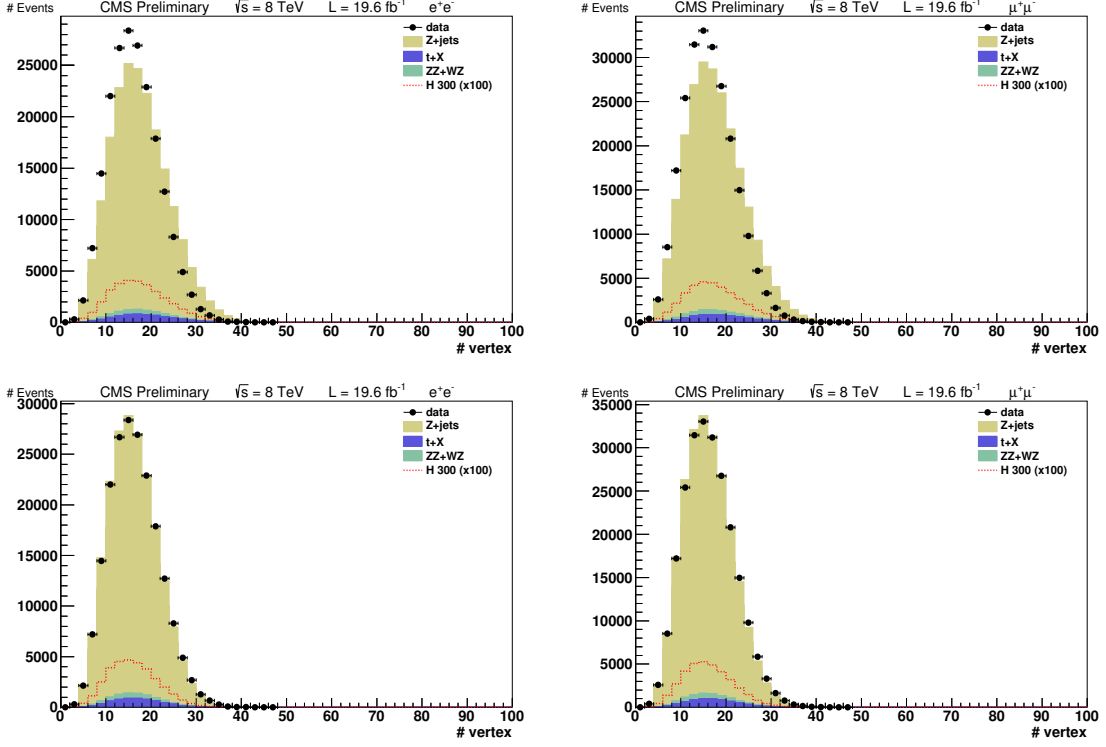


Figure 4.1. Top Left: Number of interaction in the 2012 data and the simulated samples for electrons. Top Right: Number of interaction in the 2012 data and the simulated samples for muons. Bottom Left: Electron Monte Carlo pile-up corrected. Bottom Right: Muon Monte Carlo pile-up corrected.

4.3 Preselection

The Higgs boson signal events we are searching for have a signature of a lepton pair and a quark pair. Both pairs will have an invariant mass that peaks around the Z boson mass. M_{lljj} is the invariant mass of the $\ell^+\ell^-q\bar{q}$ system which corresponds to the hypothetical Higgs boson mass. This is the main discriminating variable that we have to differentiate signal from background.

As mentioned above, particles are reconstructed from the measured detector interactions using the particle flow algorithm. We analyze events in the DoubleMu and DoubleElectron datasets. In each of these datasets, there is at least one un-prescaled

trigger with looser requirements than the off-line selections. Only events which satisfy the lowest threshold un-prescaled trigger for the dataset are considered for the analysis. The trigger requirements are summarized in Table 4.1.

For muons in 2011, the `HLT_DoubleMu7` HLT was used and required that there were two muon candidates reconstructed at the HLT level. Both of these had to have a transverse momentum larger than 7 GeV. As the luminosity of the LHC increased, this HLT was prescaled (only a fraction of the events passing were recorded) and we began to use `HLT_Mu13_Mu8`. This required the transverse momentum of one of the muons to be 13 GeV or larger and the other to be 8 GeV or larger. Again this trigger was then prescaled because of increasing luminosity and the `HLT_Mu17_Mu8` trigger was used for the final parts of 2011. Also the `SingleMu` dataset was added with the `HLT_IsoMu24` trigger to give a complete picture of the events. In 2012 only the `HLT_Mu17_Mu8` trigger on the `DoubleMuon` dataset was used requiring one muon to have a transverse momentum above 17 GeV and another muon with transverse momentum above 8 GeV.

Similar to the muon, HLT electrons are required to have one transverse momentum above 17 GeV and another electron with transverse momentum above 8 GeV. In addition to this, there are a number of other requirements on isolation to reduce the number of fake electrons.

Since the level of precision of the trigger emulation in simulation is not well known, no trigger is applied on MC samples. Instead, proper event weights are assigned to MC events according to the probabilities of lepton candidates to pass the trigger. The trigger efficiency tables for leptons satisfying the same identification criteria as in the analysis are computed in bins of (pt, η) from data using tag & probe techniques [61].

4.3.1 Lepton Selection

$Z \rightarrow e^-e^+$ and $Z \rightarrow \mu^-\mu^+$ candidates are constructed from pairs of same-flavor, opposite-charge lepton candidates, which satisfy kinematic and identification criteria.

Table 4.1
Event trigger requirements for data.

Dataset	2011 trigger requirement
DoubleMu	HLT_DoubleMu7 HLT_Mu13_Mu8 HLT_Mu17_Mu8
SingleMu	HLT_IsoMu24
DoubleElectron	HLT_Ele17_CaloIdL_CaloIsoVL_Ele8_ CaloIdL_CaloIsoVL HLT_Ele17_CaloIdT_TrkIdVL_CaloIsoVL_TrkIsoVL_ Ele8_CaloIdT_TrkIdVL_CaloIsoVL_TrkIsoVL
2012 trigger requirement	
DoubleMu	HLT_Mu17_Mu8 HLT_Mu17_TkMu8
DoubleElectron	HLT_Ele17_CaloIdT_TrkIdVL_CaloIsoVL_TrkIsoVL_ Ele8_CaloIdT_TrkIdVL_CaloIsoVL_TrkIsoVL

Electron candidates are reconstructed with the GSF algorithm and in order to assure good electron reconstruction a cut is applied: the η of the electron super-cluster must be inside the ECAL acceptance volume ($|\eta| < 2.5$) but outside the ECAL barrel-endcap overlap region ($1.4442 < |\eta| < 1.566$). Muon candidates must have been reconstructed by both the GlobalMuon and the PF muon reconstruction algorithms and must satisfy the acceptance cut $|\eta| < 2.4$.

Electron candidates must satisfy the standard “Loose” working point of the cut-based electron identification for 2012 analysis. The cuts are listed in Appendix C and comprise proper electron identification requirements, an isolation cut, and conversion rejection criteria. Muon candidates must satisfy the standard “Tight” working point

of the cut-based muon ID for 2012 analysis. The cuts are listed in Appendix C and comprise proper muon identification requirements plus an isolation cut.

Given a lepton candidate, the PF isolation is defined as the sum of deposits (i.e. p_T or E_T) of charged hadrons (I_{ch}), neutral hadrons (I_{nh}), and photons (I_{ph}), computed in a ΔR cone around the lepton direction. In order to assure independence of the isolation from the number of PU interactions, a corrected PF isolation definition is used as follows:

$$I_{PF, corr} = I_{ch}(PFnoPU) + \max(I_{nh} + I_{ph} - \rho \cdot A_{eff}, 0) \quad (4.1)$$

In the above corrected definition, only deposits from charged hadrons not coming from PU vertexes ($I_{ch}(PFnoPU)$) are considered. From these we subtract an overall PU energy contribution which is estimated as the average energy density in the event (ρ) multiplied by an effective area A_{eff} . This is strictly following the recommendations of egamma and muon POGs (Physics Object Group). The POGs are special groups within the CMS collaboration that define optimal methods of working with physics objects. The isolation cone for electrons is defined as $\Delta R < 0.3$, while for muons is defined as $\Delta R < 0.4$. The proper A_{eff} values are provided by the POGs in bins of lepton η . A cut is applied on the relative PF isolation ($I_{PF, corr}/p_T$) as reported in Appendix C.

$Z \rightarrow ee$ and $Z \rightarrow \mu\mu$ candidates are constructed from pairs of opposite-charge leptons. The leading lepton of the pair must have $p_T > 40 GeV$, while the next-to-leading lepton must have $p_T > 20 GeV$. The invariant mass of the pair must be $70 < m_{\ell\ell} < 110 GeV$. The di-lepton invariant mass for the selected $Z \rightarrow \ell\ell$ candidates is shown in Fig. 4.2.

4.3.2 Jet Selection

The PF jets are reconstructed with the anti- k_T algorithm [62] with radius parameter set to $R = 0.5$. Jets are required to be inside the tracker acceptance ($|\eta| < 2.4$) thus allowing high reconstruction efficiency and precise energy measurements using

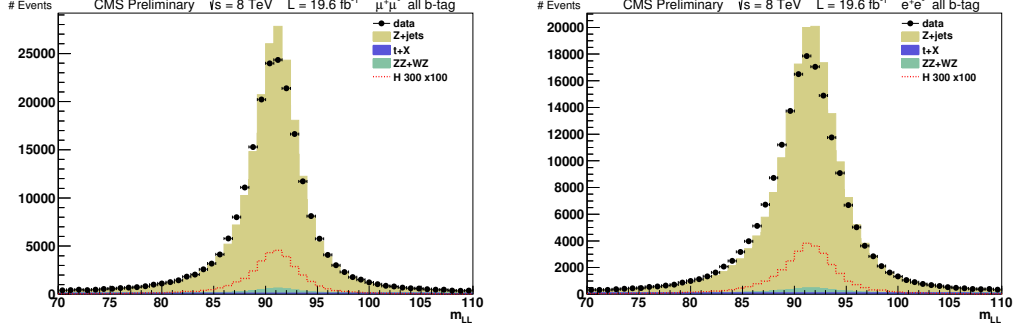


Figure 4.2. Di-lepton invariant mass in data and MC of $Z \rightarrow \ell\ell$ candidates after lepton selection. Left: Muon channel. Right: Electron channel. The selection described in preselection is applied except for the cut on m_{jj} .

PF techniques. Jet-energy corrections are applied to data and Monte Carlo [63]. Correction for PU energy is applied at the first level, by using the Fastjet algorithm [64]. In order to remove jets which originate from PU interactions, only jets with $\beta \geq 0.2$ are selected, where β is defined as the sum of transverse momenta of all charged particles in the jet coming from the primary vertex, normalized to the total sum of transverse momenta of all charged particles in the jet. The β distribution and efficiency can be seen in Figure 4.3 [65]. $Z \rightarrow q\bar{q}$ candidates are reconstructed from jet-jet pairs. In order to reject fake candidates made by low- p_T jets from QCD background, both jets of the pair must have $p_T > 30 \text{ GeV}$.

A loose jets identification is applied to the jets to remove fake jets that arise from calorimeter noise. These requirements are summarized in table 4.2. In the analysis a cut around the Z mass is done for $75 < m_{jj} < 105 \text{ GeV}$ to help control the Z+jets background. The m_{jj} distributions for electron and muon channels can be seen in Figure 4.4.

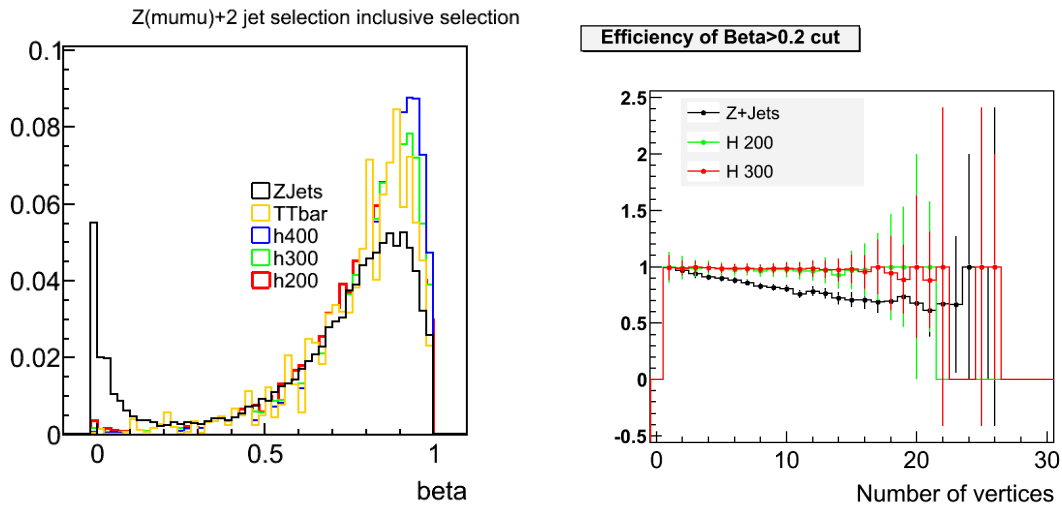


Figure 4.3. β fraction of the total transverse momentum of charged particles in a jet that is computed from particles pointing to the primary interaction for different background and signal samples (left) and efficiency of a cut in $\beta < 0.2$ for signal with Higgs mass of 200 GeV and 300 GeV and Z+Jets background, as a function of the number of reconstructed vertices in an event(right). [65]

Table 4.2
Jet cuts to remove fakes.

Variable	Cuts
fraction of energy due to neutral hadron	< 0.99
fraction of energy due to neutral EM deposits	< 0.99
number of constituents	> 1
number of charged hadrons candidates	> 0
fraction of energy due to charged hadron candidates	> 0
fraction of energy due to charged EM deposits	< 0.99
β	≥ 0.2

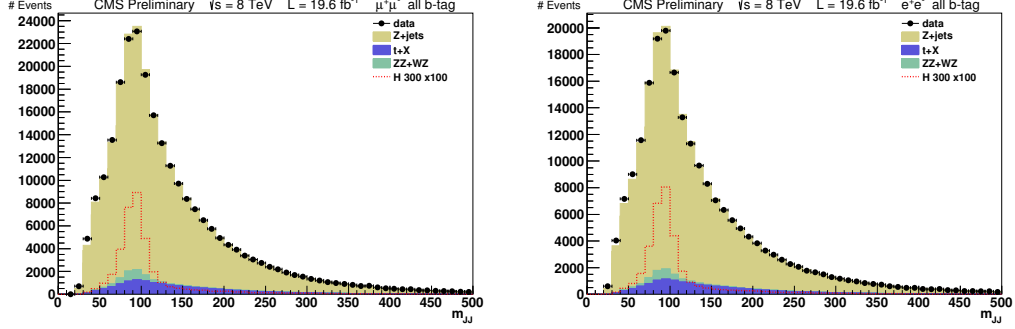


Figure 4.4. Di-jet invariant mass in data and MC for $\ell\ell jj$ candidates which have passed the preselection. Left: Muon channel. Right: Electron channel.

4.3.3 B-tagging of jets

Due to the relatively large branching fraction of the Z -bosons decaying into a pair of bottom-anti-bottom quarks, compared to the abundance of light-quark or gluon jets in $Z+jets$ background events, we use a b-tagging algorithm in order to identify jets originating from heavy-flavor quarks. However, no selection of candidates based on b-probabilities is employed in the analysis. Instead, the b-tagging information is used to classify $\ell\ell jj$ candidates into three categories, each one characterized by a certain signal-to-background ratios, and an optimized selection is applied on candidates belonging to different categories [61]. This exploits as much information as possible from the data increasing the analysis sensitivity.

With $Z+jets$ as the main background, this is primarily described by a Z boson that decays leptonically in conjunction with the production of high p_T jets. These jets are primarily produced from gluon radiation as well as light quark hadronization. These light quarks come from the fact that u and d quarks make up the valence partons of the proton. One of the main differences for signal and background is that the signal will not contain gluons, and relative to the background, will have a large contribution of heavy flavor quarks.

We are using the CMS Jet Probability (JP) tagging algorithm for b-jets [66]. This uses the relative long lifetime of bottom hadrons with the tracks from the PF algorithms to estimate if the jet came from the primary vertex. If this probably is low then the jet has a larger probability of being a b-jet. The good performance of this b-jet identification is possible because of the the precision tracking of charged particles and lepton identification at CMS.

The output of the JP algorithm is a discriminator for each jet in the event. This distribution for data and simulated events can be seen in Figure 4.5 for electrons and muons. To discriminate between jets that are coming from heavy flavor quarks (c,b) with those coming from light flavor quarks (d,u,s) we use two separate values from the JP algorithm. The first point, called the loose working point (L), is set at a value of the output of the JP algorithm equal to 0.0275. This working point corresponds to a mis-identification probability that the jet is a light flavored jet of 10%. The medium working point (M) has a value of 0.545 and has a mis-identification probability of 1%. These are abbreviated as JPL and JPM for the loose and medium working points respectively.

A summary of all the selection can be found in section 5.6.

4.3.4 Higgs candidates

All the leptons and jets that satisfy the above requirements are combined to form both leptonic and hadronic Z bosons. For each event, the dilepton and dijet pairs are combined to create $\ell\ell jj$ events or Higgs candidates. A $\Delta R > 0.5$ cut is applied between each lepton and jet within a candidate in order to avoid double counting of the same object reconstructed in different collections (for instance leptons inside a jet). An example event with a Higgs boson candidate decaying to two muons and two jets can be seen in Figure 4.6 [67]. In the following sections, the previous requirements on Higgs candidates and their constituent particles will be referred to as preselection.

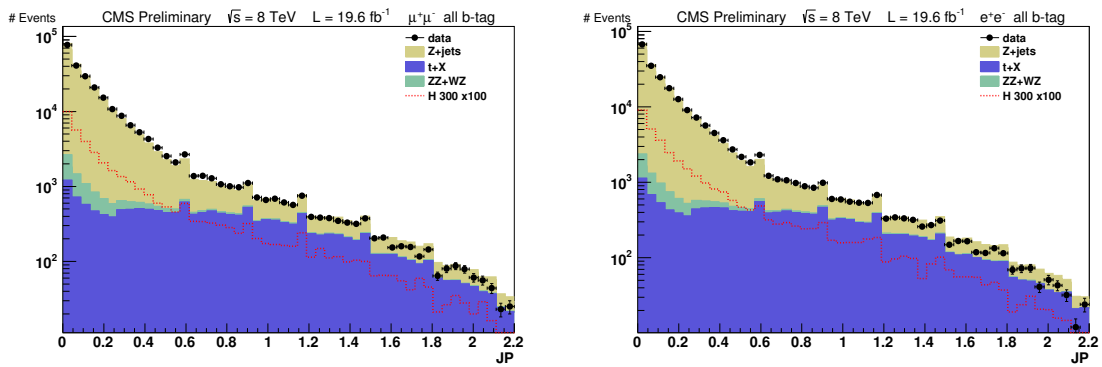


Figure 4.5. Distribution of the jet probability (JP) discriminator that is used for b-tagging. Right: Muons. Left: Electrons. The peaks in the distribution come from calculating the jet probability non-continuously in η bins. This phenomenon is well understood and expected.

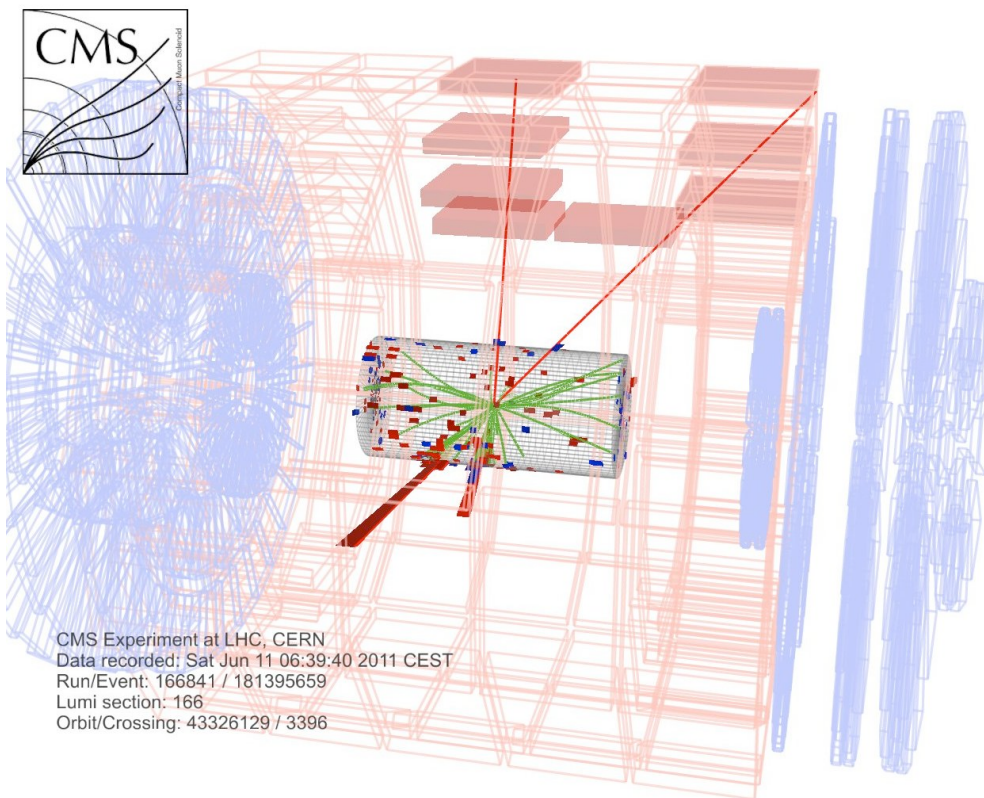


Figure 4.6. An event display of a Higgs event candidate decaying to two muons and two jets. [67]

5. Signal Optimization

After the preselection, additional selection criteria is performed to optimize the discrimination power for a Higgs signal.

5.1 Tagging Classification

Once the events are preselected as described in the previous sections, they are classified according to the b-tagging (see section 4.3.3) of the jets associated to the Higgs candidate. Events are classified as “two tags” if the two jets are b-tagged with at least one medium-tag and one loose-tag. Events failing that requirement are classified as “one tag” if at least one of the two jets satisfy the loose-tag condition. Events failing this requirement are finally classified as “no-tag”. These three categories are mutually exclusive. A summary can be seen in Table 5.1.

Table 5.1
B-tag categories.

Tag Region	Description
0-tag	jet is not tagged loose; other jet is not tagged loose
1-tag	jet is tagged loose; other jet is not tagged medium
2-tag	jet is tagged medium; other jet is tagged loose

As these three categories present very different signal-to-background ratios they are treated separately in the final optimization. In addition, some differences in the selection are also needed due to the different background compositions, especially in the case of the “two tags” sample, in which the $t\bar{t}$ background starts to be noticeable. On the other hand, since the optimization is based mostly on the intrinsic properties

of the final state under investigation, there are analysis strategies that are shared by the three categories. The main differences between the categories are that the 2 b-tag category has the highest purity, but has very low signal yield. Opposed to that, the 0 b-tag category has the largest signal yield but is dominated by Z+jets background. The 1 b-tag category is affected by both issues and therefore has the least discriminating power.

There are differences in the b-tagging between data and those predicted by Monte Carlo. These differences are corrected by b-tagging scale factors. These are used to adjust two different problems. The first is the efficiency that the JP algorithm will not recognize a b-jet even if it is from a heavy flavored quark. Second, the light quarks or gluons are incorrectly identified as b-jets.

The efficiency (SF_{hf}) (from non tagging of heavy quarks) and the mis-identification rate (SF_{lf}) (labeling light quarks and gluons as b-jets) are defined as the ratio of tagging efficiency between heavy and light flavor jets in data and simulations. These are typically functions of p_T and the pseudo-rapidity of the jets. Typically SF_{hf} is smaller than one because in data the successful tagging of heavy quarks is better than in simulation. Oppositely, SF_{lf} is typically larger than one because tagging light quarks in data as b-jets is more common than in simulation. In general, all jets regardless of flavor are tagged as b-jets more frequently in data than jets in simulation. An explanation of this mismatch can be found in the b-jet identification analysis [66].

The b-tagging performance is corrected between data and simulation, but we must take additional steps than simply scaling the JP distribution. This is because our classification of events is based on the jet flavor of both tagged and non-tagged jets. The process to correctly distribute candidates between the categories is as follows. As the scale factors change the jets' momentum, there is a percentage of jets that will migrate to a different b-tagged category. Using a random number generator, candidates are upgraded or downgraded between the different b-tagging categories according to the scale factor percentages. This gives jets that are tagged a non zero chance of being lowered to another category or non-tagged jets to be raised to a

higher category. For example, a medium-tagged jet can be lowered to a loose-tagged jet, or a loose-tagged jet can be lowered to a non-tagged jet. Also, a non-tagged jet can be promoted to a loose-tagged jet, or a loose-tagged jet can be promoted to a medium-tagged jet [65].

5.2 Helicity Likelihood

There are a number of kinematic differences between the $H \rightarrow ZZ \rightarrow 2l2q$ decay and the Z + jets background. When a heavy Higgs boson is produced and decays into two Z bosons, those Z bosons have boosted kinematics. The p_T of the Z bosons increases with the mass of the parent particle, the Higgs boson. Another powerful variable to separate signal from background is the ΔR spacing between the two jets, leptons, and Z bosons. This space decreases as the boost of the Z bosons increases and is similarly correlated to the reconstructed Higgs mass as can be seen in Figure 5.1. Since we use the invariant mass of the reconstructed Higgs candidate as the main discriminating variable, these kinematic variables are problematic to use. Also, the variable selection criteria would need to be parameterized as a function of the reconstructed di-boson invariant mass.

The signal topology is affected by the production of a heavy Higgs. These topological features are not limited to only the kinematics of the final state particles but have other manifestations as well. This is because the decay of a spin-0 boson decays to a pair of identical spin-1 bosons which decay to fermions. For us, the spin-0 boson is the Higgs and the spin-1 bosons are the Z bosons. This well defined spin correlation will be seen in the angular distribution of the final state particles. The probability density functions of the angles can be computed analytically for Higgs signals [68]. The background is not resonant so there is no spin correlation and thus there are different angular distributions for the final states between Z+Jets and the signal. This topology difference is not unique to the Higgs boson and can also help in the search for other particles [69].

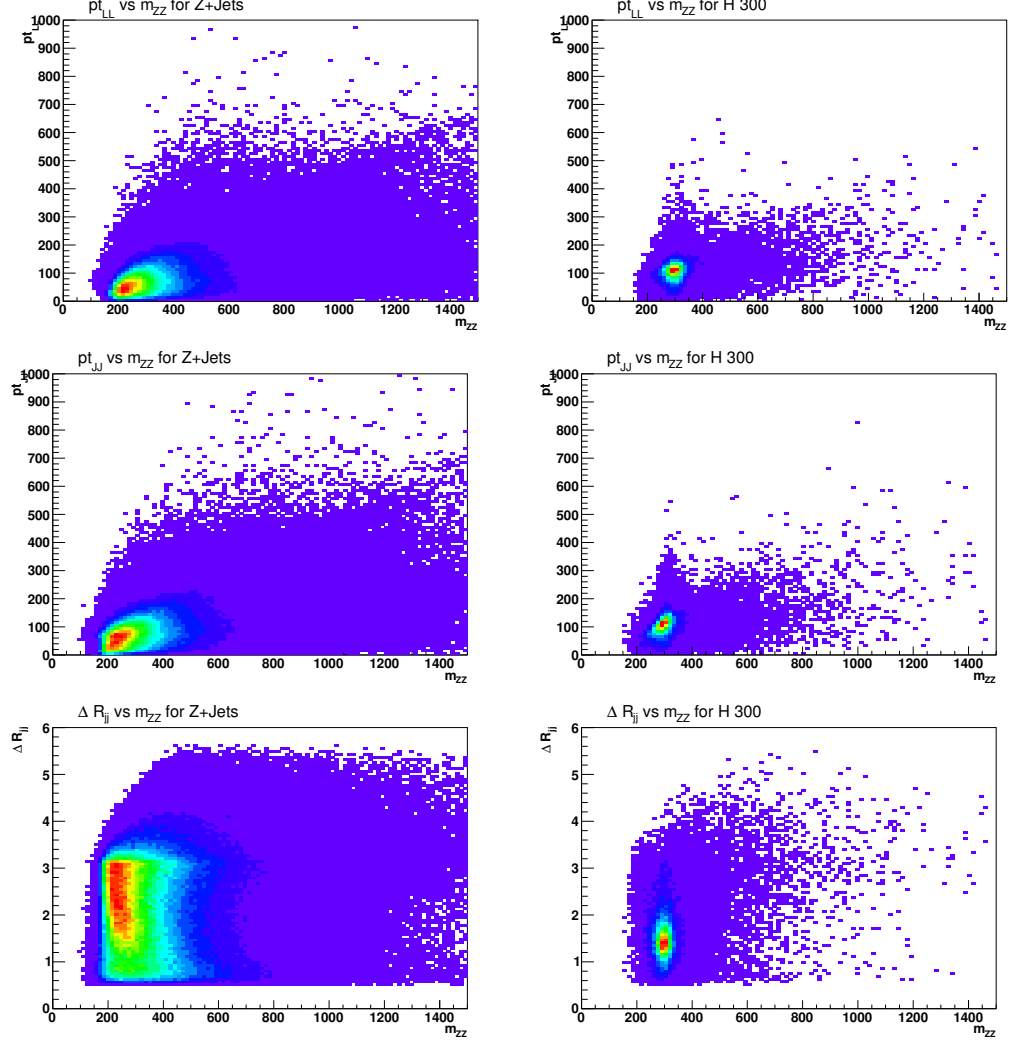


Figure 5.1. Various kinematic variables comparing Z+Jets background and Higgs of 300 GeV simulations to demonstrate the correlation between the kinematics and m_{ZZ} . (Top Left) $p_T(l\bar{l})$ vs m_{ZZ} for Z+Jets. (Top Right) $p_T(l\bar{l})$ vs m_{ZZ} for Higgs 300. (Middle Left) $p_T(j\bar{j})$ vs m_{ZZ} for Z+Jets. (Middle Right) $p_T(j\bar{j})$ vs m_{ZZ} for Higgs 300. (Bottom Left) ΔR_{jj} vs m_{ZZ} for Z+Jets. (Bottom Right) ΔR_{jj} vs m_{ZZ} for Higgs 300.

The decay kinematics in the signal $H \rightarrow ZZ \rightarrow 2l2q$ have several distinct features that can be used to discriminate against background. Five angular observables fully describe the angular distribution of the decay products in $2 \rightarrow 1 \rightarrow 2 \rightarrow 4$ as in $ab \rightarrow X \rightarrow ZZ \rightarrow 2l2j$ [70, 71]. There are three helicity angles θ_1, θ_2 , and Φ , as well

as two production angles θ^* and Φ_1 . These quantities are uncorrelated to the invariant mass of the X and the two Z and are uncorrelated to the longitudinal and transverse momentum of X . The observables are useful for event selection beyond using them as raw kinematic observables. The definitions of these variables can be found in Table 5.2. Fig. 5.2 illustrates the angular distribution in the production and decay chain $ab \rightarrow X \rightarrow P_1 P_2 \rightarrow p_{11} p_{12} p_{21} p_{22}$ with an example of the $ab \rightarrow X \rightarrow ZZ \rightarrow 2\ell 2q$ chain with two partons a and b , such as gg or $q\bar{q}$.

Table 5.2
Definitions of the 5 angular variables describing events of the form
 $ab \rightarrow X \rightarrow ZZ \rightarrow 2\ell 2j$ as seen in Figure 5.2.

Variable	Definition
θ_1	The angle between the direction of the ℓ^- (from $Z \rightarrow \ell^+ \ell^-$) and the direction opposite the X in the Z rest frame.
θ_2	The angle between the direction of the q (from $Z \rightarrow q\bar{q}$) and the direction opposite the X in the Z rest frame.
Φ	The angle between the decay planes of the two Z decays.
θ^*	The angle between the parton collision axis (z) and the decay axis in the rest frame (z').
Φ_1	The angle between the production plane and the $Z \rightarrow \ell^+ \ell^-$ decay plane.

The angular distributions for data and simulations can be found in Figures 5.3, 5.4, and 5.5 for electrons and in Figures 5.6, 5.7, and 5.8 for muons. These figures show the differences between the samples in each of the b-tag regions. Because the background does not have spin correlation, there is a difference between the simulated signal, the background simulation, and data. Also, you can see similar performance between electrons and muons, as well as between different b-tag categories. This similarity between muons and electrons, as well as between b-tag categories, is expected and

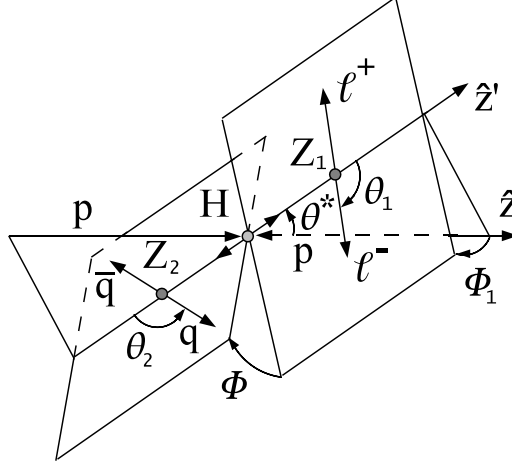


Figure 5.2. Diagram depicting the decay $X \rightarrow ZZ \rightarrow 2l2q$ and the 5 decay angles which describe it.

will be used to simplify the analysis by doing common final selection between lepton types and b-tag categories.

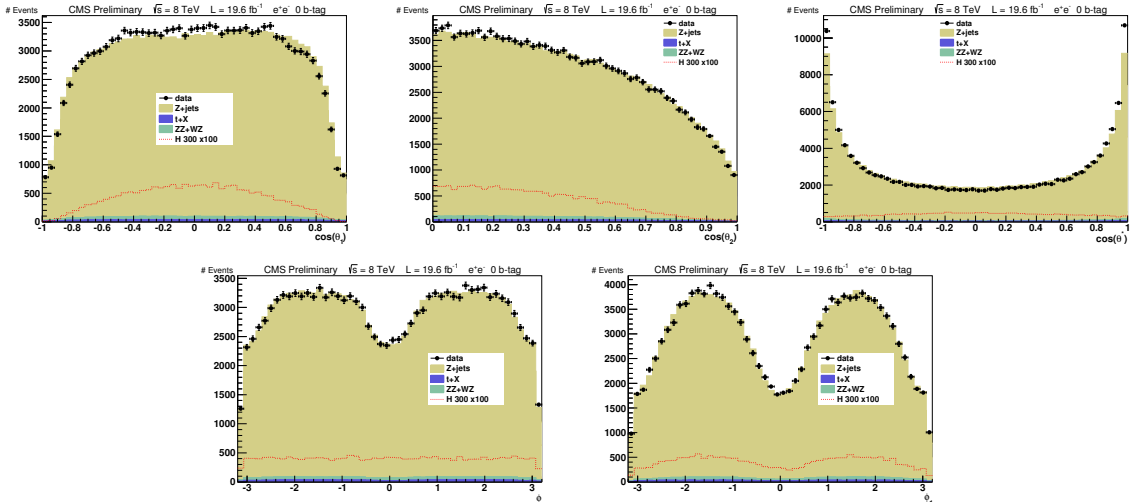


Figure 5.3. Five angular distributions of $\cos\theta_1$, $\cos\theta_2$, $\cos\theta^*$, Φ , Φ_1 and the helicity likelihood discriminant for 2012 electron data (points) and Summer 2012 Monte Carlo samples (histogram) in the 0 b-tag category. The red line is the expected distribution for a Higgs boson with mass 300 GeV. The selection is as described in preselection.

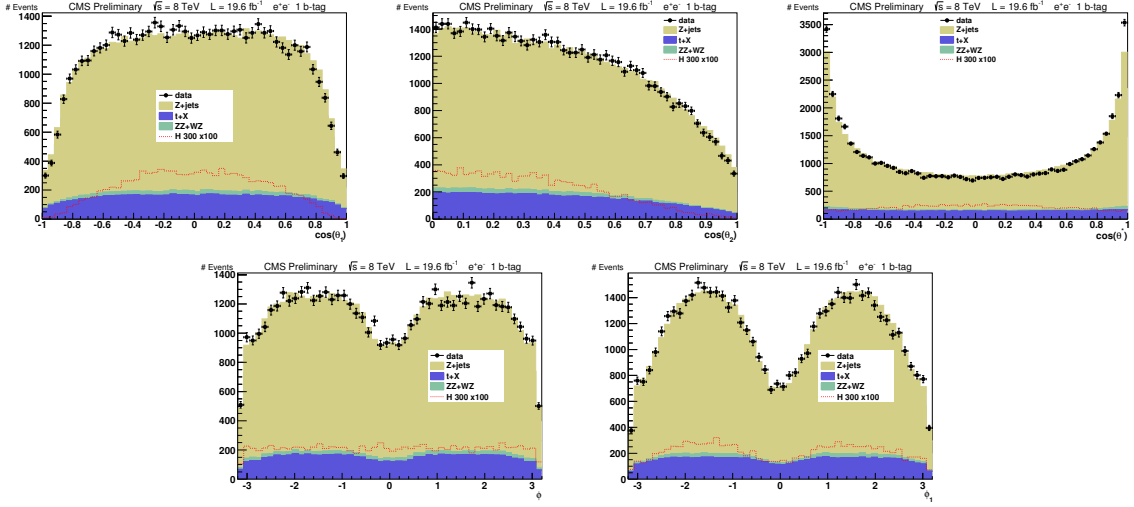


Figure 5.4. Five angular distributions of $\cos \theta_1$, $\cos \theta_2$, $\cos \theta^*$, Φ , Φ_1 and the helicity likelihood discriminant for 2012 electron data (points) and Summer 12 Monte Carlo samples (histogram) in the 1 b-tag category. Open histograms indicate the expected distribution for a Higgs boson with mass 300 GeV. The selection is as described in preselection.

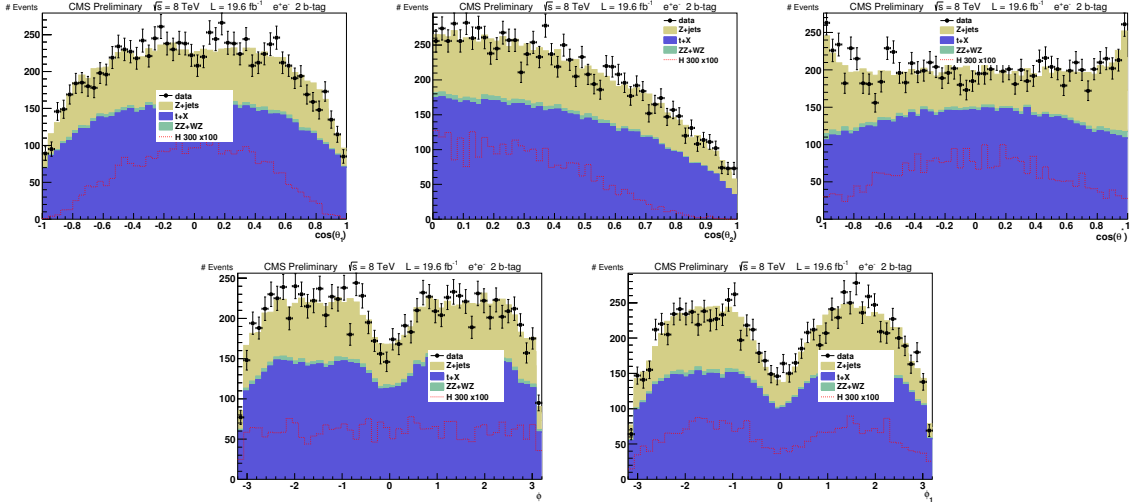


Figure 5.5. Five angular distributions of $\cos \theta_1$, $\cos \theta_2$, $\cos \theta^*$, Φ , Φ_1 and the helicity likelihood discriminant for 2012 electron data (points) and Summer 12 Monte Carlo samples (histogram) in the 2 b-tag category. Open histograms indicate the expected distribution for a Higgs boson with mass 300 GeV. The selection is as described in preselection.

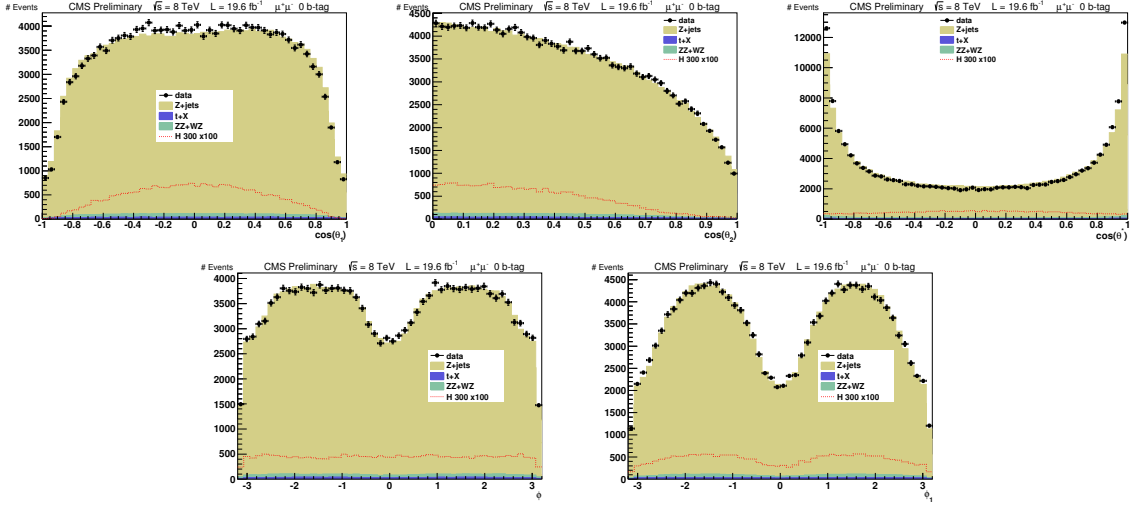


Figure 5.6. Five angular distributions of $\cos \theta_1$, $\cos \theta_2$, $\cos \theta^*$, Φ , Φ_1 and the helicity likelihood discriminant for 2012 muon data (points) and Summer 12 Monte Carlo samples (histogram) in the 0 b-tag category. The selection is as described in preselection.

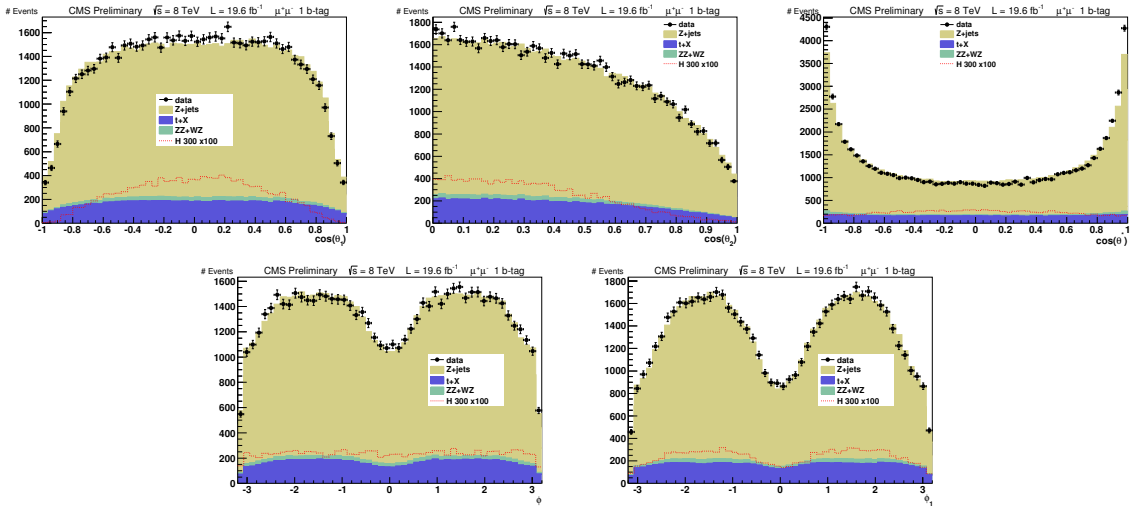


Figure 5.7. Five angular distributions of $\cos \theta_1$, $\cos \theta_2$, $\cos \theta^*$, Φ , Φ_1 and the helicity likelihood discriminant for 2012 muon data (points) and Summer 12 Monte Carlo samples (histogram) in the 1 b-tag category. Open histograms indicate the expected distribution for a Higgs boson with mass 300 GeV. The selection is as described in preselection.

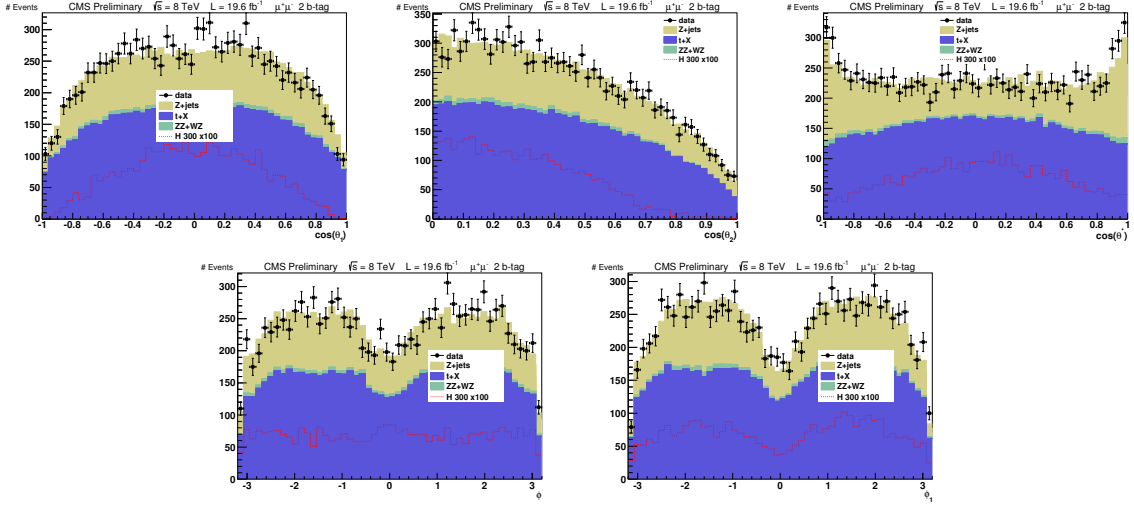


Figure 5.8. Five angular distributions of $\cos \theta_1$, $\cos \theta_2$, $\cos \theta^*$, Φ , Φ_1 and the helicity likelihood discriminant for 2012 muon data (points) and Summer 12 Monte Carlo samples (histogram) in the 2 b-tag category. Open histograms indicate the expected distribution for a Higgs boson with mass 300 GeV. The selection is as described in preselection.

5.2.1 Angular Discriminant

The information from the angular variables in the final state particles can be used to define a likelihood discriminant. This likelihood discriminant allows us to select the topology that is consistent with a Higgs decay. The first step in creating the likelihood discriminant is to build the probability density functions for both the signal and background events. After these have been defined, we use them to get a likelihood ratio as seen in Equation 5.1 where LD is the likelihood discriminant, P_{sig} is the probability the candidate is signal, and P_{BG} is the probability the candidate is background.

$$LD = \frac{P_{sig}}{P_{sig} + P_{BG}} \quad (5.1)$$

This definition puts candidates that have a topology like the signal to have a LD value close to 1 and those candidates with a topology similar to those of the background will have a LD value closer to 0. This allows us to use this LD variable

(in the future referenced to as helyLD) for event selection by requiring candidates to have a value higher than a certain threshold.

The function P_{sig} (Equation 5.2) is defined as the theoretically calculated probability function [69] (P_{ideal}) multiplied by four 1D acceptance functions.

$$P_{sig} = P_{ideal}(\theta_1, \theta_2, \theta^*, \Phi, \Phi_1; M) G_{\theta_1}(\theta_1; M) G_{\theta_2}(\theta_2; M) G_{\theta^*}(\theta^*; M) G_{\Phi_1}(\Phi_1; M) \quad (5.2)$$

In Equation 5.2, M is the mass of the reconstructed Higgs candidate and the acceptance functions ($G_{\theta_1}, G_{\theta_2}, G_{\theta^*}, G_{\Phi_1}$) are empirically calculated by fitting each of the signal Monte Carlo simulations separately.

Similar to data, the probability distribution function for background is given in Equation 5.3.

$$P_{BG} = P_{\theta_1}(\theta_1; M) P_{\theta_2}(\theta_2; M) P_{\theta^*}(\theta^*; M) P_{\Phi_1}(\Phi_1; M) P_{\Phi^*}(\Phi^*; M) \quad (5.3)$$

Each probability function is obtained entirely empirically from the fits to the simulation background Monte Carlo samples.

The acceptance functions are created for each angular variable through a number of steps. First we define a number of bins around a central Higgs mass that we are looking at. Then, using signal samples in these bins, we fit each angular variable to a polynomial. The list of polynomials can be seen in Table 5.3. An example of fitting the acceptance functions as a function of the reconstructed Higgs mass for a 500 GeV sample can be seen in Figure 5.9.

After the polynomials are fit for the range of reconstructed Higgs masses, coefficients of the polynomials are then fit with a polynomial to parameterize the fits as a function of the ZZ invariant mass. This allows the acceptance functions to be a function of only the ZZ invariant mass and extends the function to be continuous for the Higgs mass values that we do not have Monte Carlo simulations for. An example of calculating the parameters can be seen in Figure 5.10 for $\cos(\theta_1)$. Similar fitting is done for the other angular variables. Figure 5.11 shows the differences for the acceptance function $G_{\theta^*}(\theta^*; 450)$ between a direct fit and using the extrapolation used to get the parameterization of the polynomial coefficients.

Table 5.3
The polynomials used for fitting each angular variable.

Variable	Polynomial
$\cos(\theta_1)$	$a_2x^2 + a_4x^4$
$\cos(\theta_2)$	$a_2x^2 + a_4x^4$
$\cos(\theta^*)$	$a_2x^2 + a_4x^4 + a_6x^6$
Φ	$1 + a_0\cos(x) + a_1\cos(2x)$
Φ_1	$1 + a_0\cos(x) + a_1\cos(2x);$

With these functions defined, we can then calculate the helicity likelihood discriminant as a function of the ZZ invariant mass. Figure 5.12 shows the distributions for the HelyLD in the 2012 data for both electrons and muons as well as an example of the shape of signal for a Higgs mass of 300 GeV. This is shown for each of the 3 b-tag regions. We can see that particularly in the 0-tag and 1-tag regions this is a powerful discriminating variable for the Z+Jets background. In the 2-tag region the $t\bar{t}$ background is much more prevalent, but this selection is still powerful against the Z+Jets.

There is a discrepancy between the data and Monte Carlo simulated samples, in that the data is more background like than simulation suggests. This is caused by the simulated Z+Jets samples not correctly representing data in the $\cos(\theta^*)$ samples. This discrepancy can be seen in Figure 5.13 and is in the range of $0.8 < |\cos(\theta^*)| < 1.0$. If we keep only events in which $|\cos(\theta^*)| < 0.8$ then the HelyLD distribution between data and simulation is within good agreement, as can be seen in Figure 5.14. Similar studies have been done scaling the simulation to data resulting in a correction of the HelyLD distribution. While these measures will correct the distribution, this region of disagreement is rejected from the analysis later and there is no significant difference on the final yields between correcting the $\cos(\theta^*)$ distribution or not. Because of these reasons, we do not apply any corrections to the HelyLD distribution.

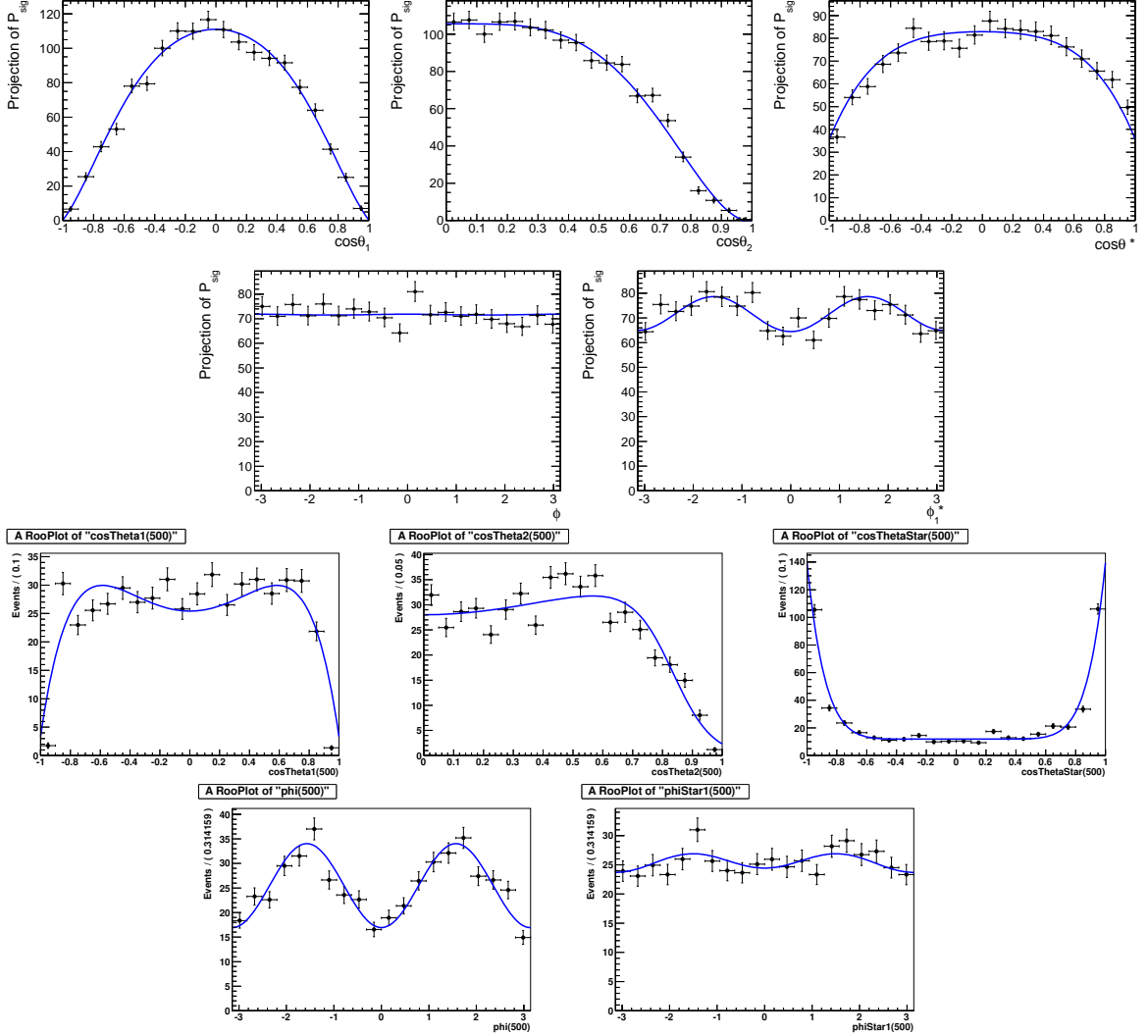


Figure 5.9. Fitting the angular variables for a reconstructed Higgs mass of 500 GeV in signal Monte Carlo samples (first 5 plots) and for the Z+Jets background samples (bottom 5 plots). These are taken in a mass window of 450 GeV to 550 GeV in the ZZ invariant mass distribution.

5.3 Signal Optimization Based on Helicity Neural Network

The helicity LD is such an important part of the analysis that a cross check on its performance is performed. For this, a Neural Network is applied to separate Higgs signal from background using the five helicity angles of the final objects in the analysis

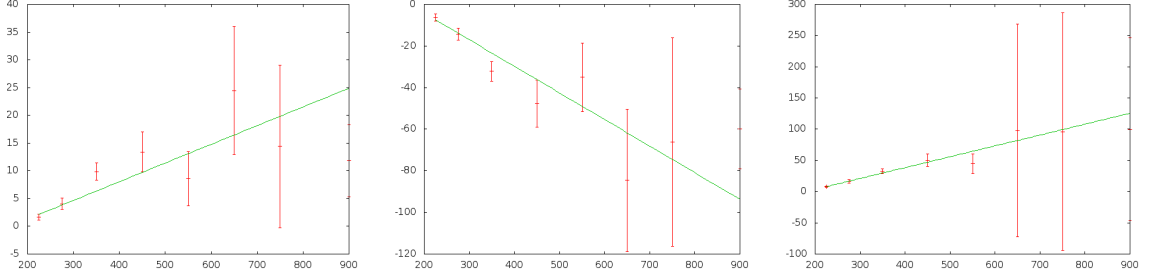


Figure 5.10. Fitting the parameters a_2 (left), a_4 (middle), a_6 (right) for $\cos(\theta_1)$ to calculate the acceptance function $G_{\theta_1}(\theta_1; M)$ as a function of the reconstructed Higgs mass. The same fitting is done for the other angular variables.

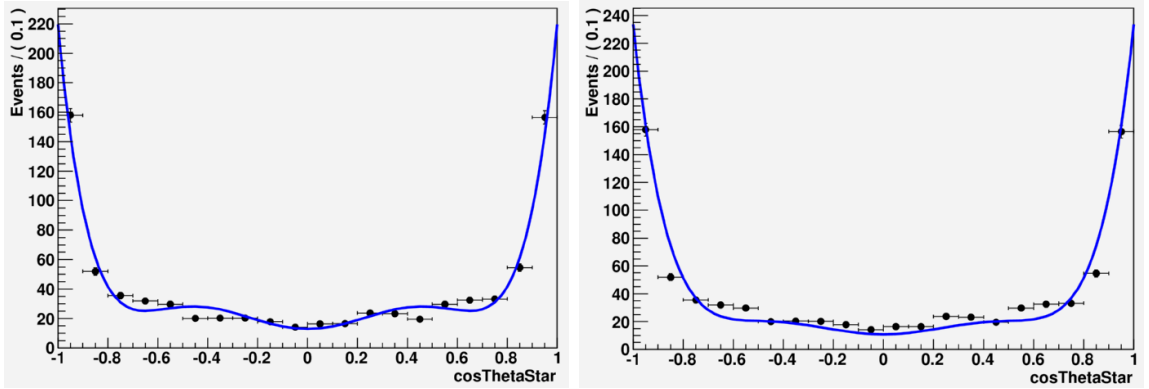


Figure 5.11. A $\cos(\theta^*)$ comparison for the 450 GeV reconstructed Higgs mass signal simulations fitting the acceptance function $G_{\theta_1}(\theta_1; M)$ directly to data (right), and plotting $G_{\theta_1}(\theta_1; 450)$ from the extrapolated polynomial coefficients (left). There is very good agreement between the fitting and extrapolation.

as inputs. A training and test evaluation has been performed with the framework of the TMVA package [72] using the true event weight mix of Monte Carlo processes as background and Higgs Monte Carlo. Both the training and testing samples for both background and signal are constructed and events randomly mixed outside of the Neural Network. There are 37,874 signal events and 38,378 background events evenly split between testing and training. The Neural Network was trained on the

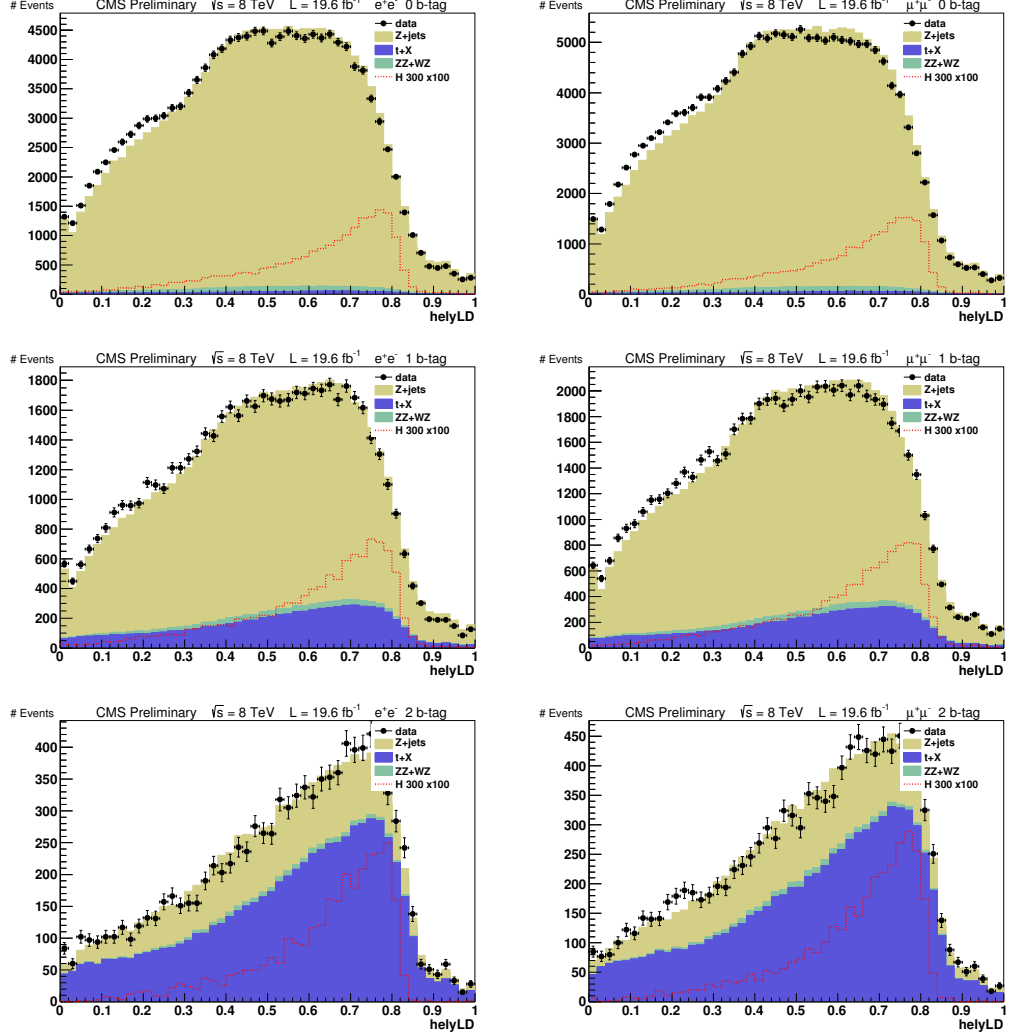


Figure 5.12. HelyLD for electrons (right) and muons(left) for the 3 b-tag categories, 0-tag (top), 1-tag (middle), 2-tag (bottom). The preselection is applied to this data and the 300 GeV signal Monte Carlo is scaled by 100 to get a better picture of the comparison.

Monte Carlo simulation generated for a hypothetical Higgs mass of 400 GeV. This training was on events that passed the previously explained preselection and the Z boson mass window selection, but before the selection on MET significance, which will be examined in more detail later in this section.

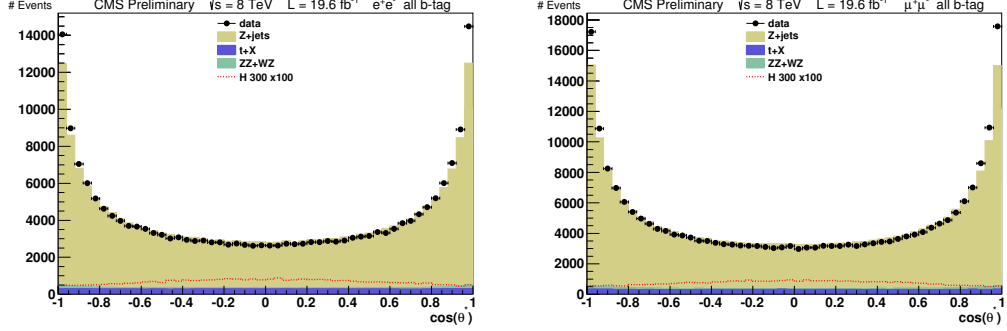


Figure 5.13. $\cos(\theta^*)$ distributions for electrons (right) and muons (left). The mismatch between simulation and data can be seen in the range $0.8 < |\cos(\theta^*)| < 1.0$.

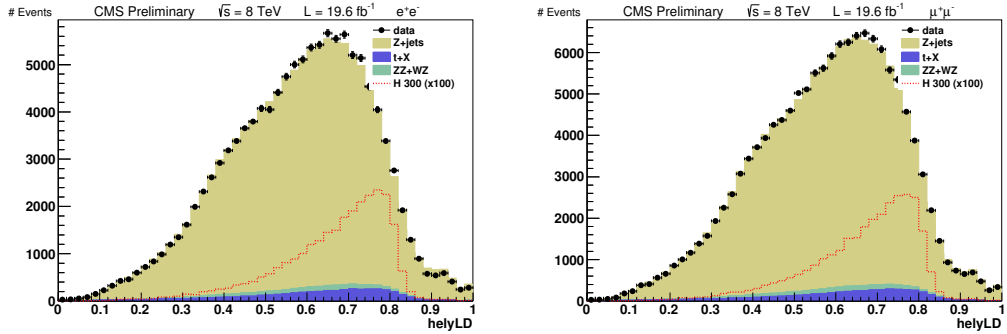


Figure 5.14. HelyLD distribution after applying the selection $0.8 < |\cos(\theta^*)|$ showing much better agreement between Monte Carlo simulation and data.

5.3.1 Neural Network Architecture

The architecture of the Neural Network consists of two hidden layers with N and N neurons respectively, where N is the number of variables, and one output node as shown in Figure 5.15.

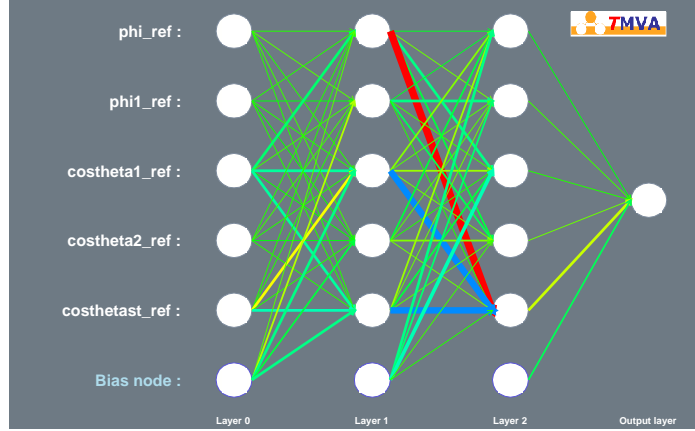


Figure 5.15. Neural Network architecture used for the training.

5.3.2 Helicity Neural Network

The training and testing of the Neural Network can be seen in Figure 5.17. While there is separation between the signal and background and good agreement between testing and training, there is a definite spike in background at the same place as the signal spikes in the MLP (Multilayer perceptron neural network) training. The training was done with Monte Carlo generated for a hypothetical Higgs mass of 400 GeV, but then applied to the Monte Carlo for hypothetical Higgs masses of 300, 400, 500, and 600 GeV. This is because the angular components should not depend on Higgs mass. The distribution for all b-tag regions and multiple signal simulated samples can be seen in Figure 5.19, showing good discrimination between signal and background as well as good performance of the single 400 GeV training on the various signal samples.

In addition to the MLP neural network, a likelihood discriminant was calculated using the TMVA package to check the MLP performance using the same input parameters. Figure 5.18 shows the receiver operating characteristic (ROC) curve for the helicity LD, MLP, and likelihood discriminators. These show that when looking

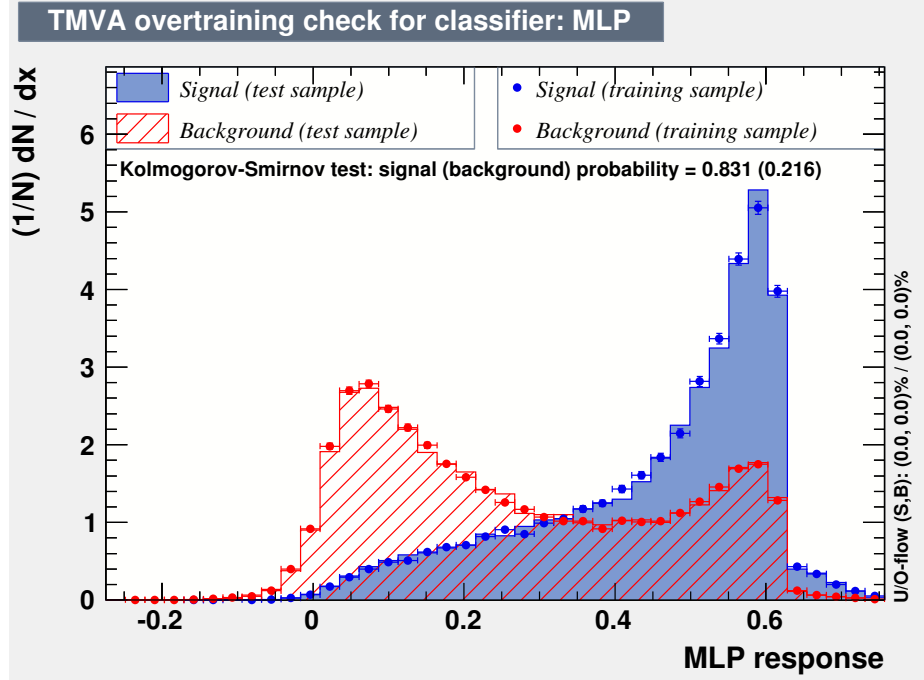


Figure 5.16. The training is done after preselection and mixing electrons and muons. Additionally we require at least one JP medium jet with training 400 GeV Higgs boson with a MLP neural network.

at the performance between the three after preselection requirements, the MLP performs significantly better than the helicity LD. However, after looking in windows of $-6\%/+10\%$ around the generated Higgs mass, we see the improvement drop away and we get very similar performance. This shows that the MLP is training on additional information than the helicity LD is using, but that this information is correlated to the mass of the reconstructed Higgs candidate.

In the 0-tag region the separation between signal and background looks similar to the training for Higgs 300, 400, and 500 GeV, but does not have much discrimination power for a Higgs of 200 GeV. The discrimination power is virtually the same after applying an additional selection of $-6\%/+10\%$ of the Higgs mass for all four cases. When comparing background rejection versus signal efficiency between the neural

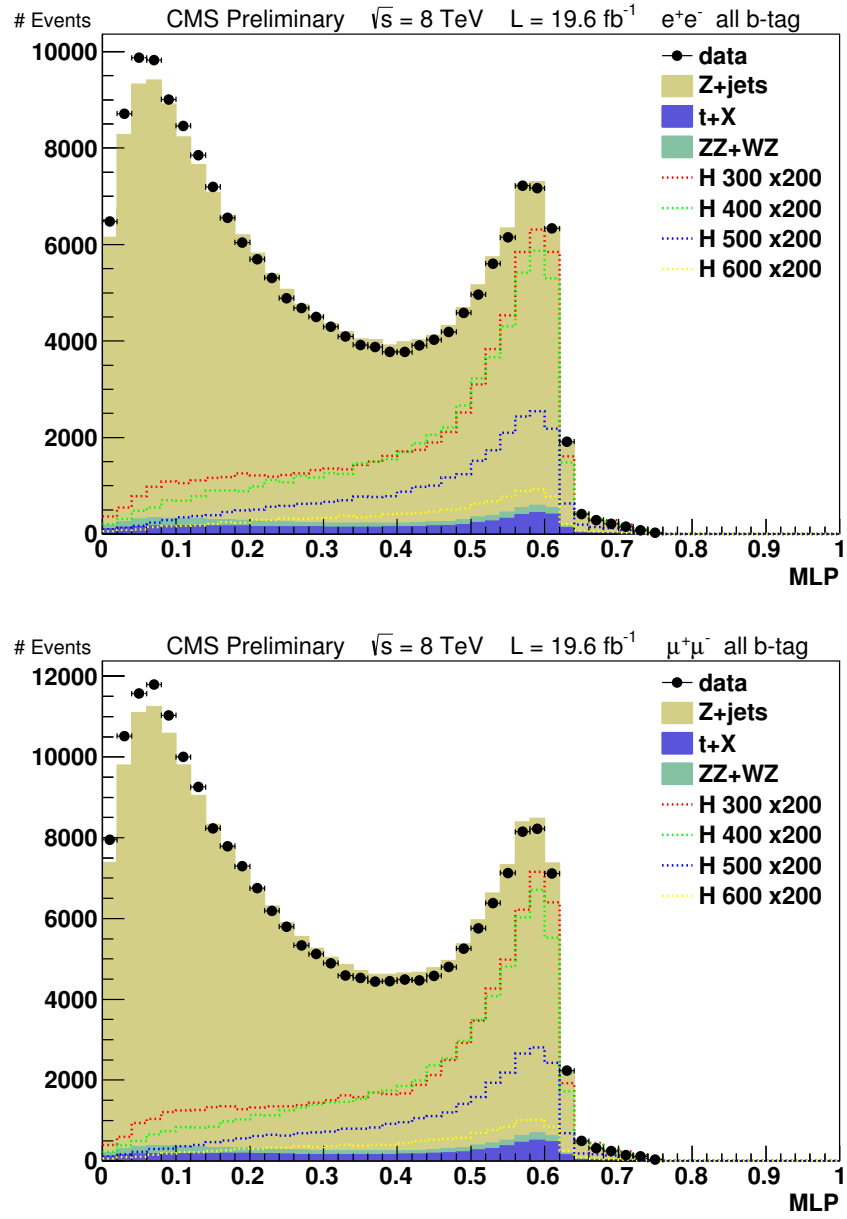


Figure 5.17. The MLP neural network distribution for electrons (top) and muons (bottom). This training was done on the 400 GeV signal simulations, but applied to the 300, 400, 500, and 600 GeV samples to display the discriminating power over the entire mass range. The signal simulations are scaled for ease of reading.

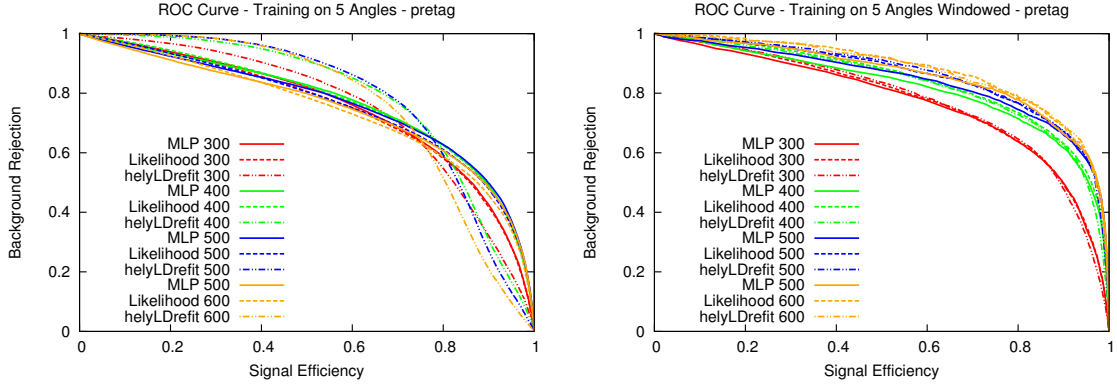


Figure 5.18. The ROC curve for signal and background comparing the HelyLD, MLP, and an alternate training for a likelihood discriminant using the TMVA package after preselection (right). The same curve is given with additional selection of $-6\%/+10\%$ of the Higgs mass to give a better estimation of performance for the final shape analysis.

network and likelihood discriminant, the performance is for all practical purposes the same.

In the 1-tag region the separation between signal and background looks similar to the training for Higgs 300, 400, and 500 GeV, but does not have much discrimination power for a Higgs of 200 GeV. The discrimination power is virtually the same after applying an additional selection of $-6\%/+10\%$ of the Higgs mass for all four cases. When comparing background rejection versus signal efficiency between the neural network and likelihood discriminant, the performance is for all practical purposes the same. See Figure 5.20.

In the 2-tag region, after applying a selection of $-6\%/+10\%$ of the Higgs mass, the discriminating power of the neural network is similar to the 1-tag case with poor performance for a Higgs of 200 GeV, but good separation for Higgs of 300, 400, and 500 GeV. When comparing background rejection versus signal efficiency between the neural network and likelihood discriminant the performance is roughly the same, except for the Higgs of 200 GeV case where the neural network is consistently better than the likelihood discriminant. This is shown in Figure 5.21.

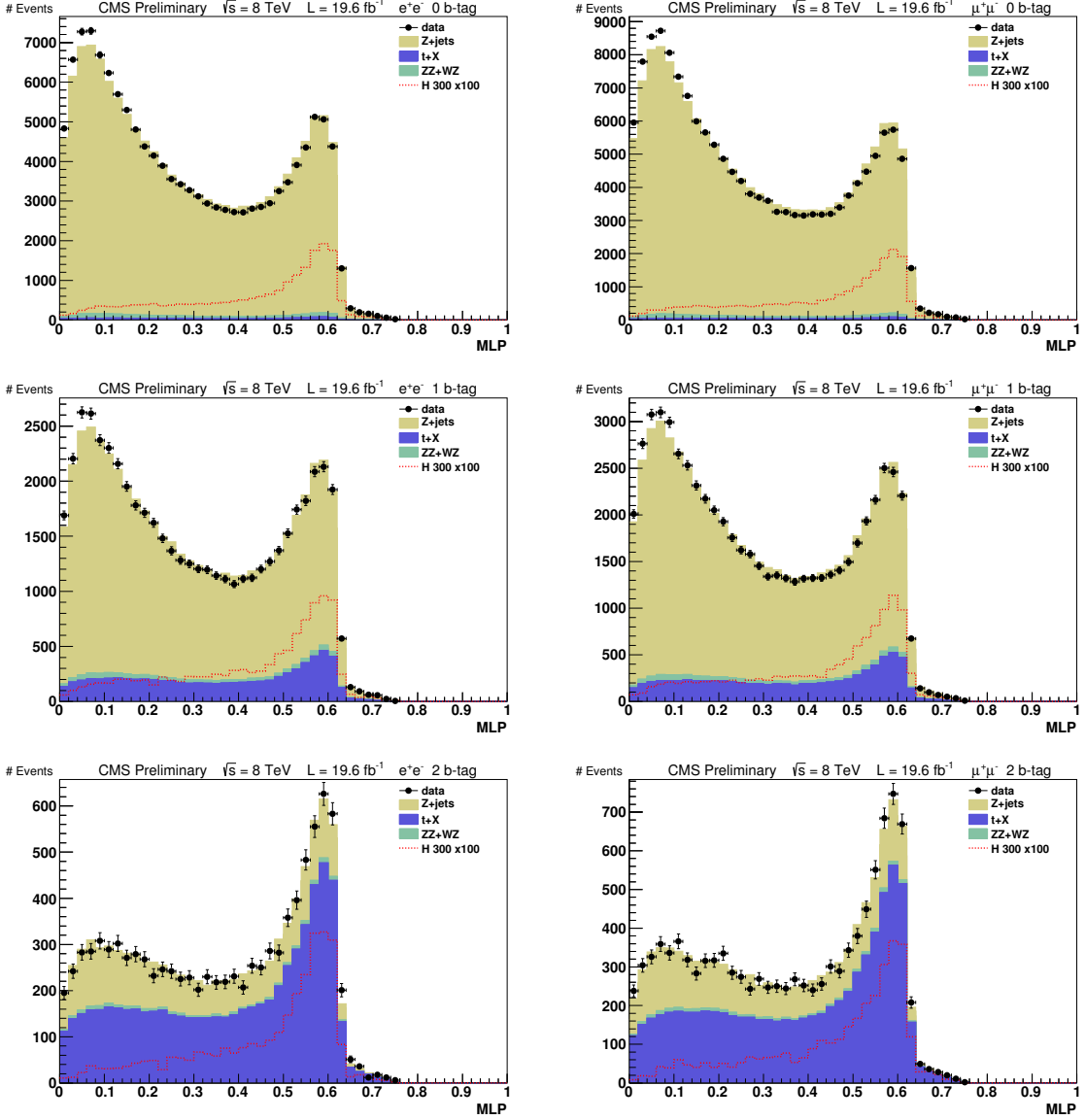


Figure 5.19. The MLP neural network output for electrons (right column) and muons (left column) for the 0 b-tag region (top row), 1 b-tag region (center row) and 2 b-tag region (bottom row). This is after preselection and also has a 300 GeV signal sample superimposed on the graphs multiplied by 100 for better visibility.

5.3.3 Extended MVA Variables

A neural network or likelihood should be able to take advantage of more information than simply using the 5 decay angles as previously shown. One such variable

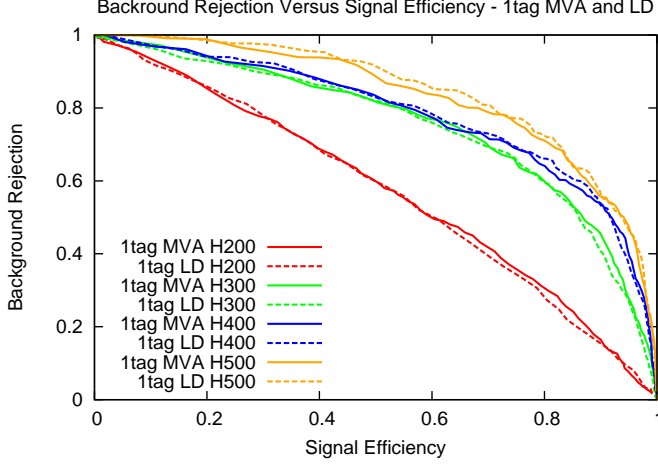


Figure 5.20. Background Rejection Versus Signal Efficiency in the 1tag region comparing the Multi Variant Analysis output to the helicity likelihood discriminant for a Higgs mass of 200, 300, 400, and 500 GeV. This is calculated after preselection, Z boson mass requirements, and requirements on MET significance, in a $-6\%/+10\%$ Higgs mass window.

that offers good discrimination power in the preselection region is $Z_{lupt} / \sum pt$, where $\sum pt$ is the sum of the two leptons, two jets, and the met. Z_{lupt} and $\sum pt$ are scalar quantities. This variable distribution is shown in Figure 5.22. While adding this variable to a MLP training improves the discrimination power in the inclusive pretag region, once we look in a mass window of $-6\%/+10\%$ around 400 GeV this actually lowers the discrimination power of the neural network. This same performance drop is seen when training is done with the addition of the reconstructed Higgs mass as well.

This under-performance of adding additional information to the MLP neural network is due to over training in the regions where the background will not contribute (outside of the mass window of $-6\%/+10\%$ around Higgs). We should be able to gain additional performance by training the samples after only looking around the Higgs mass, but the sample sizes get too small to do a multi-variate analysis. This can be seen by looking at the high correlation between the additional variables and the

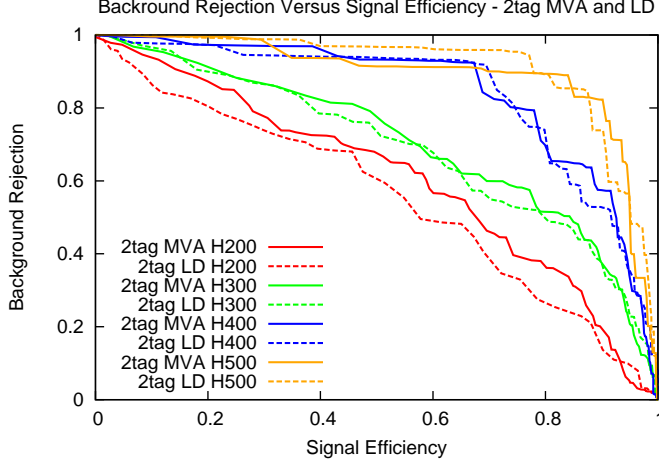


Figure 5.21. Background Rejection Versus Signal Efficiency in the 2tag region comparing the Multi Variant Analysis output to the helicity likelihood discriminant for a Higgs mass of 200, 300, 400, and 500 GeV. This is calculated after preselection, Z boson mass requirements, and requirements on MET significance, in a -6%/+10% Higgs mass window.

reconstructed ZZ invariant mass, whereas the 5 helicity angular variables are orthogonal to the ZZ , Z_{ll} , and Z_{qq} invariant masses. The $Z+jets$ samples are approximately 25 million events when we start so increasing these samples by an order of magnitude is not computationally feasible.

5.4 Helicity Optimization

The helicity likelihood discriminant is optimized using a Punzi equation [73] as seen in Equation 5.4.

$$\frac{sig_{eff}}{0.98 + \sqrt{B}} \quad (5.4)$$

sig_{eff} is the signal efficiency defined as $\frac{\text{number of signal events selected}}{\text{total number of signal events}}$ and B is the number of background events. This Punzi equation is used instead of more traditional functions like $\frac{S}{B}$, $\frac{S}{\sqrt{B}}$, and $\frac{S}{\sqrt{S+B}}$ because we are optimizing the analysis

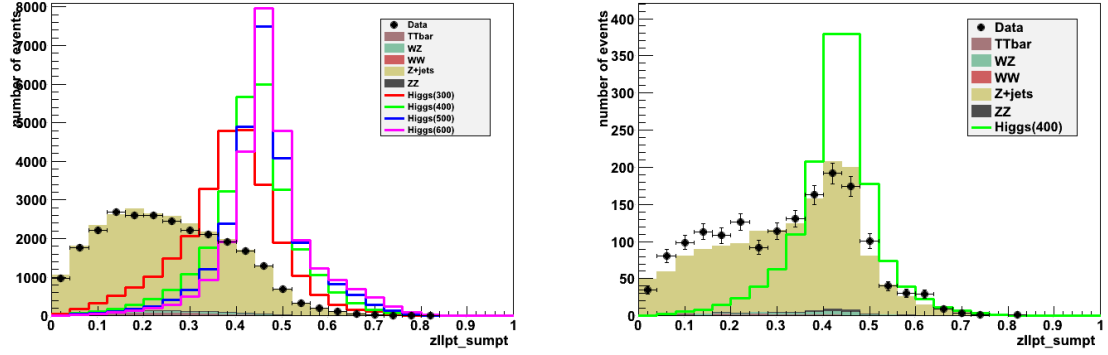


Figure 5.22. Signal samples are normalized to background. Left: $\frac{Z_{up}}{\sum pt}$ after preselection. Right: $\frac{Z_{up}}{\sum pt}$ after preselection and $376 < m_{ZZ} < 440$ GeV.

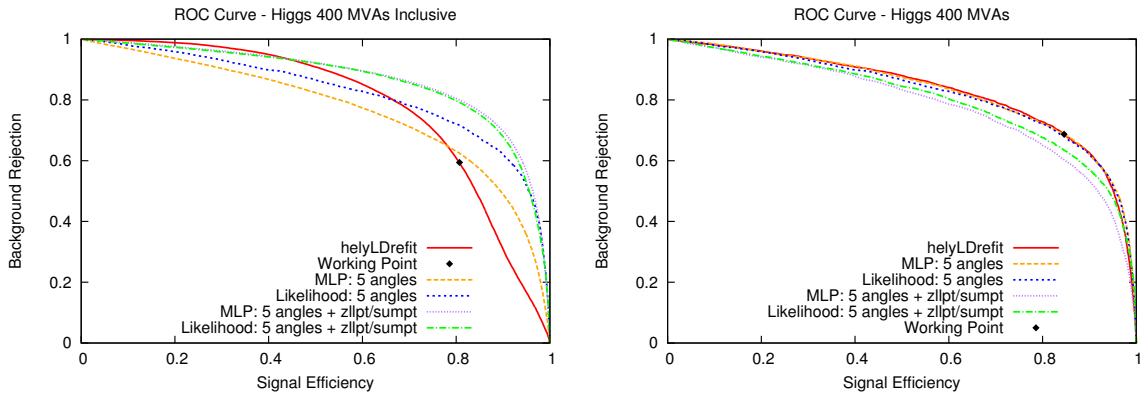


Figure 5.23. Applying a MLP training to preselection and at least one JP medium jet. The working point is the equivalent performance of current analysis that we apply in the two tag region. The helyLD variable is shown for comparison. Left: ROC curves after preselection. Right: ROC curves after preselection and $376 < m_{ZZ} < 440$ GeV.

for exclusion over discovery. This optimization is done for the MLP neural network that is trained on the helicity angles as well. A selection on 0.5 in all the regions is within 5% of the optimal value. So instead of making our selection as a function of reconstructed ZZ invariant mass, we simply apply 0.5 for all mass ranges and for

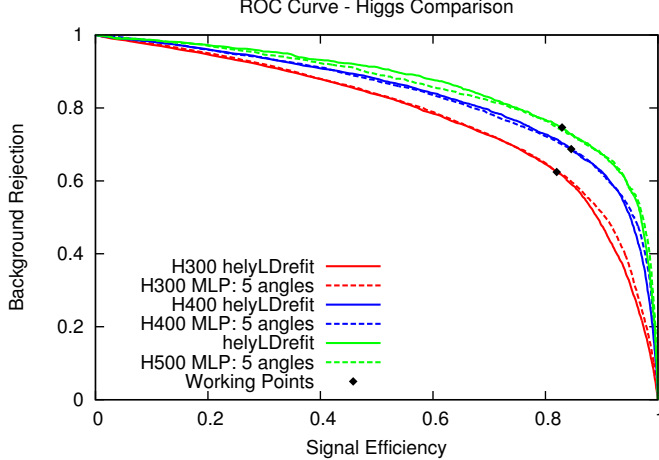


Figure 5.24. This training is for a MLP neural network trained on the 5 decay angles of a Higgs 400 GeV sample. This training is applied after preselection and requiring at least one JP medium jet to samples with a Higgs mass of 300, 400, and 500 GeV. The working point is the background rejection point that we currently achieve in the two tag region in our analysis. The helyLD variable is shown for comparison.

all b-tag categories. While 0.5 is a good selection for the MLP, when cross checking between the HelyLD and the MLP, we use the working points as found in Figure 5.24. These working points correspond to efficiency we get in the main line analysis.

5.5 Missing Transverse Energy

After doing preselection and selection using the helicity angles, the 2 b-tag category is still rich in events from $t\bar{t}$ that have two b-quark jets. Our Higgs signature $H \rightarrow ZZ \rightarrow \ell^+\ell^-q\bar{q}$ in addition to the jets have two leptons. The main background that looks like this is: $t\bar{t} \rightarrow (W^+ \rightarrow \ell^+\nu)b(W^- \rightarrow \ell^-\bar{\nu})\bar{b}$. This final state contains oppositely signed leptons (like signal), 2 b-jets (like signal), and two neutrinos (unlike signal).

The additional neutrinos in the final state of the $t\bar{t}$ background give us a nice handle on this background. Every event in the detector must conserve the total

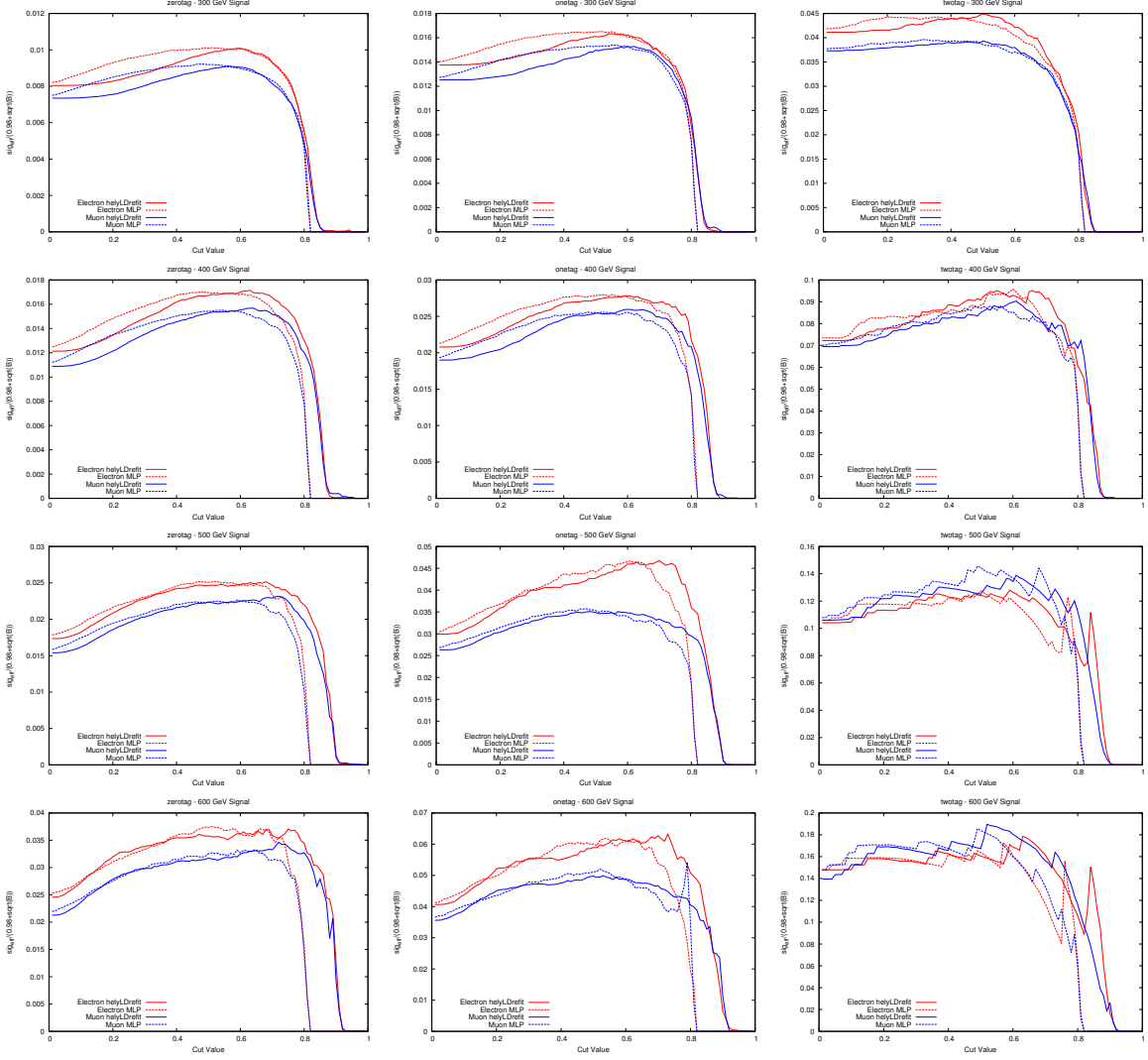


Figure 5.25. The Punzi equation $\frac{\text{sig}_{\text{eff}}}{0.98 + \sqrt{B}}$ for the 3 b-tag regions 0-tag (left column), 1-tag (center column), 2-tag (right column) and Higgs masses 300 (top row), 400 (second row), 500 (third row), 600 (bottom row) GeV. Also a selection outside of the region $\pm 20\%$ around the Higgs masses for each sample is applied to make it similar to the final region. Each plots shows electrons and muons separately.

momentum in the transverse plane. If there is an imbalance among all particles, it means that most likely there is a weakly interacting particle passing through the

detector (like neutrinos). If this imbalance is seen in the event, most likely the event is not in our channel of Higgs decay due to of the lack of neutrinos in the final state.

We define MET as the quantity of transverse energy that is not detected from the events. Reasons for this include gaps in the detectors, as well as finite resolution of the detector, meaning particle flow candidates may not be reconstructed at full efficiency.

While many of these problems can be taken into account to correct the MET, another option is to look at the significance of the PF MET. A function called MET significance can be built by using two likelihood functions; one for the likelihood that the true MET is equal to the value measured in the PF algorithm, and another likelihood which measures if the true MET is equal to zero [74]. The definition of MET significance can be found in Equation 5.5.

$$\text{MET Significance} = 2\ln\lambda(\text{MET}) = 2\ln\frac{L(\text{MET}_{\text{true}} = \text{MET}_{\text{measured}})}{L(\text{MET}_{\text{true}} = 0)} \quad (5.5)$$

Figure 5.26 shows the MET significance after preselection in the three b-tag categories. While the $t\bar{t}$ background is mainly a problem for the 2-tag category, we apply a selection on MET significance on all b-tag categories for constancy. This MET significance requirement of 10 is very loose and is in the tail of the signal distribution. This allows the systematic uncertainty for the disagreement between data and background prediction to be negligible compared to other sources of systematic uncertainty.

Small differences in the MET significance of the data and the Drell-Yan Z+jets simulation are taken into account studying the region $\text{MET significance} < 6$, where the contamination of the $t+X$ background is reduced. It is observed that a simple multiplicative factor of 1.15 ± 0.01 brings the Monte Carlo distribution in very good agreement with the data, a factor that is stable for muons and electrons, and as a function of the number of vertices in the event [75]. The validity of this factor has been checked up to larger values of the MET significance in a top-depleted data subsample, requiring p_T of jets < 20 GeV. Therefore the MET significance in the Drell-Yan, diboson and Higgs boson Monte Carlo events is multiplied by a factor

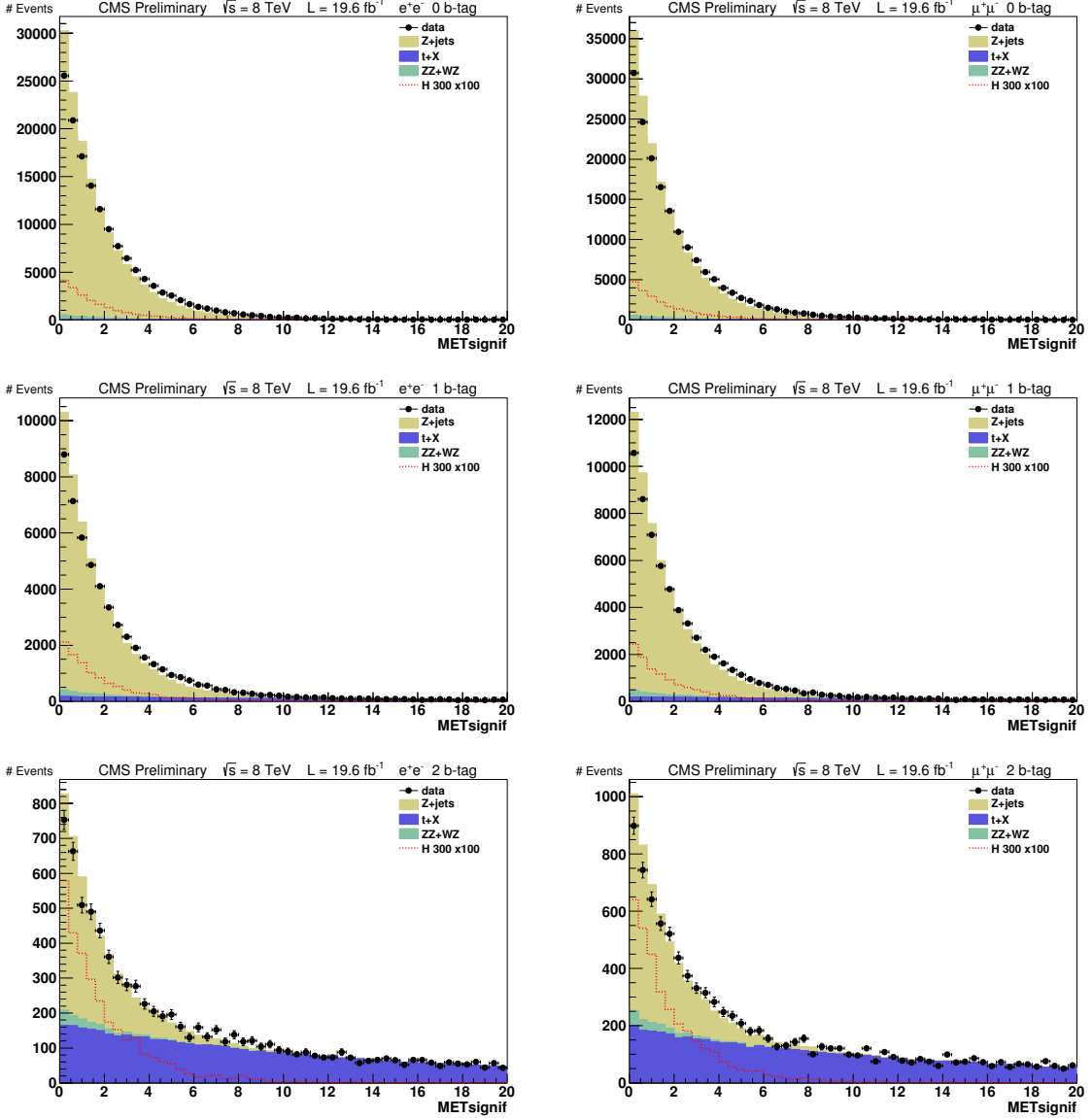


Figure 5.26. Distributions for MET significance after preselection for electrons (right column) and muons (left column) for the 0 b-tag region (top row), 1 b-tag region (center row), and 2 b-tag region (bottom row). A signal simulation is superimposed for a Higgs 300 GeV and multiplied by 100 for ease of reading.

1.15. The effect of this factor on the efficiency of the MET significance is minimal (in all cases the efficiency changes by less than 1%).

5.6 Summary of Selection Requirements

The selection and preselection is the same for all b-tag categories. While there is a difference between the signal and background in each category, the additional discrimination power is negligible and for ease of analysis we use the same selection in each category. Table 5.4 shows a summary of the selection, both the preselection and the final selection.

When there are multiple candidates per event, we apply a string of logic operators to choose one candidate per event. The best candidate is selected by first looking at the signal and sideband region. If a candidate is in the signal region, it is chosen over those in the sidebands. If there are multiple candidates per event in the signal region, then the candidate is chosen according to the higher b-tag category (2 b-tags over 1 b-tag and 1 b-tag over 0 b-tags). If there are multiple candidates in the same b-tag region, then the candidate with the invariant masses of the Z bosons closest to the nominal Z boson mass is chosen. If none of the candidates make it into the signal region, the same ranking of candidates is done for all those in the sideband region.

$$|M_{\ell^+\ell^-} - m_Z| + |M_{JJ} - m_Z| \quad (5.6)$$

The expected yields corresponding to 19.6 fb^{-1} after all the selection can be seen in Table 5.5.

Table 5.4
Selection on the 3 b-tag categories.

observable	0 b-tag	1 b-tag	2 b-tag
btag	none	JPL	JPL & JPM
helicity LD		> 0.5	
missing E_T significance		< 10	
m_{jj}		$[71,111] \text{ GeV}/c^2$	
m_{ll}		$[76,106] \text{ GeV}/c^2$	
$p_T(l^\pm)$		$> 40/20 \text{ GeV}/c$	
$p_T(\text{jets})$		$> 30 \text{ GeV}/c$	
$ \eta (l^\pm)$		$e^\pm < 2.5, \mu^\pm < 2.4$	
$ \eta (\text{jets})$		< 2.4	
lepton quality		see section 4	
jet quality		see section 4	

Table 5.5
Signal expected yields with 19.6 fb^{-1} of data. The background is the combination of Z+jets, $t\bar{t}$, and diboson Monte Carlo.

tag categories	0 b-tag		1 b-tag		2 b-tag	
lepton categories	$\mu\mu jj$	$ee jj$	$\mu\mu jj$	$ee jj$	$\mu\mu jj$	$ee jj$
expected background	21265	19342	7604	6700	731	666
observed data	21396	18505	7788	6689	703	633
$M_H = 250 \text{ GeV}$	118.0	106.9	58.9	55.2	19.0	17.9
$M_H = 300 \text{ GeV}$	126.7	119.1	67.1	57.7	24.7	21.1
$M_H = 400 \text{ GeV}$	121.9	107.2	68.5	60.7	27.3	23.9
$M_H = 500 \text{ GeV}$	57.2	52.7	33.0	29.9	13.7	12.3
$M_H = 600 \text{ GeV}$	21.4	19.3	13.0	12.0	5.3	4.8

6. Correlated and Uncorrelated Systematic Uncertainties

In this chapter the systematic uncertainties affecting the analysis, the methods used to estimate them, and their calculated values are described. The following signal uncertainties are included: Lepton Trigger and Selection, Jet Reconstruction, b-tagging, MET, pile-up, production mechanism, luminosity, and Higgs cross section. After the treatment on signal uncertainties, the background uncertainties are given as well.

6.1 Signal Uncertainties

The main systematic uncertainties on signal normalization as discussed below are summarized in Table 6.1.

6.1.1 Trigger and Lepton Selection Efficiency

To calculate the lepton efficiency, we use the tag and probe method [76]. This method allows the determination of a variety of efficiencies by using a data sample of pure leptons from Z boson decays. For each event, one of the leptons must pass our tag criteria and is labeled as a tag. The other lepton is our probe. Selection efficiency is calculated by comparing the number of probes that pass or fail our selection. We require our events to contain a minimum of two leptons from a Z decay as well as a minimum of one jet. This matches the event topology that we use in the analysis. The requirements for tag and probe events are shown in Table 6.3. After measuring efficiency in data by applying the same method to measure simulation efficiency, we are able to calculate the scale factors. The complete efficiency measurement can be split into five relative measurements: tracking efficiency, reconstruction efficiency,

identification efficiency, isolation efficiency, and the total trigger efficiency. This is expressed in equation (6.1).

$$\epsilon_{lepton} = \epsilon_{tracking} \times \epsilon_{RECO/tracking} \times \epsilon_{ID/RECO} \times \epsilon_{ISO/ID} \times \epsilon_{trigger/ISO} \quad (6.1)$$

Each term in the total efficiency is calculated separately. The efficiencies are measured in p_T and η bins. The trigger used for the 2012 data is the HLT_Ele17_CaloIdVT_CaloIsoVT_Trig17. The trigger needs to be selected to yield unbiased efficiencies for each type. Also the cuts for the L1 and HLT triggers must be looser than those being measured. The tag is required to pass the WP (working point) Medium which is given in Appendix C. Also, the tag is spatially matched to a triggering object and has an energy above 32 GeV. The probe is required to have opposite charge to the tag and the tag-probe combination must have an invariant mass between 60 and 120 GeV. When there

Table 6.1

Summary of systematic uncertainties on signal normalization. Most sources are multiplicative errors on the cross section measurement, except for expected Higgs cross section.

Source	0 b-tag	1 b-tag	2 b-tag	Comment
Muon trigger & ID	2.7%			Tag-&-probe study
Electron trigger & ID	2%			Tag-&-probe study
Electron energy scale	0.2%			
Muon momentum scale	0.1%			
Jet reconstruction	1-4%			JES, correlated among categories
b -tagging eff. and mis-tag rate	1-4%	1-5%	5-8%	Anti-correlated among categories
MET	< 1%			Loose requirement
Pile-up	1-2%			Correlated between categories
Production mechanism (PDF)	1.5%			PDF4LHC, acceptance only
Production mechanism (line-shape)	0-3%			Only for $M_H > 400\text{GeV}$
Luminosity	4.4%			Same for all analyses
Higgs cross section	13-15%			CERN Yellow Report

are multiple tag-probe pairs, all of the pairs are used in order to avoid biasing the measurement. $\epsilon_{tracking}$ is assumed to be essentially 100% [77].

For ϵ_{RECO} , the probes are super-clusters with the standard η cuts and an energy above 10 GeV. At least one jet has to have a $p_T > 5$ GeV and the hadronic energy fraction must be greater than 0.15. If there are photons in the events, the requirements are `hadronicOverEm < 0.15`, standard η cuts, for the barrel `sigmaIetaIeta < 0.01`, while for end cap `sigmaIetaIeta < 0.03`, and `supercluster.energy * sin(supercluster.position.theta) > 20` GeV. For the electrons, passing probes are those that are reconstructed with the GSF algorithm giving a GSF electron. When calculating these efficiencies a fit is used as seen in Figure 6.1. The fit range is 60 -120 GeV. The functional form of the signal PDF (probability density function) is formed from a Breit-Wigner convoluted with a “crystal ball” function [78]. The background PDF is an exponential multiplied by an error function modeling the kinematic turn on of CMS. The values are reported in Appendix B.

ϵ_{ISO} is computed with the same fits as described for calculating ϵ_{RECO} , as well as the same tags. The fits can be seen in Figure 6.2. This time the probes are required to be GSF Electrons and the passing probes are those GSF Electrons that also pass WP Medium (as described in Appendix C). For electrons, the electron identification efficiency is factorized together with isolation and the efficiencies are shown in Appendix B.

Counting passing vs failing probes is used instead of fitting because the backgrounds are predicted from Monte Carlo to be negligible. The tags are again the same as described before. The probes are those GSF Electrons that pass WP medium and the passing probes pass one of the filters of the HLT for the DoubleElectron dataset. For those electrons passing the HLT, we calculate the efficiency in two parts. The corresponding filters are given in Table 6.2. These efficiencies are shown in Appendix B.

Muon efficiency is also calculated using the tag and probe method but they do not need the extra isolation cut to reduce fake events. Other than that, the process is the same as described for electrons. For muons the total normalization uncertainty

is 2.7%, with contributions from the trigger (2.5%), identification (1.0%), and isolation (0.4%). For electrons the total normalization uncertainty is 2%, dominated by identification (2%), and a much smaller contribution from the dielectron trigger efficiency. Normalization uncertainties related to the electron energy scale and the muon momentum scale are very small; always much below 1%.

Table 6.2
The Legs for the Electron HLT.

Leg	Filter
Ele8	hltEle17TightIdLooseIsoEle8TightIdLooseIsoTrackIsoDoubleFilter
Ele17	hltEle17TightIdLooseIsoEle8TightIdLooseIsoTrackIsoFilter

Table 6.3
These are the event requirements for the tag and probe method of calculating trigger and lepton selection efficiency.

Lepton Energy	> 10 GeV
gsfElectron	> 1
super-cluster $ \eta $	< 2.5
ak5PFJet	> 1
Jet $ \eta $	< 2.4
Jet pt	> 30 GeV

6.1.2 Jet Reconstruction

There are two components of the uncertainty on jets. One is the jet energy scale (JES) and the other is the resolution. The resolution uncertainty is negligible compared to other uncertainties, but the JES does make a measurable effect. The

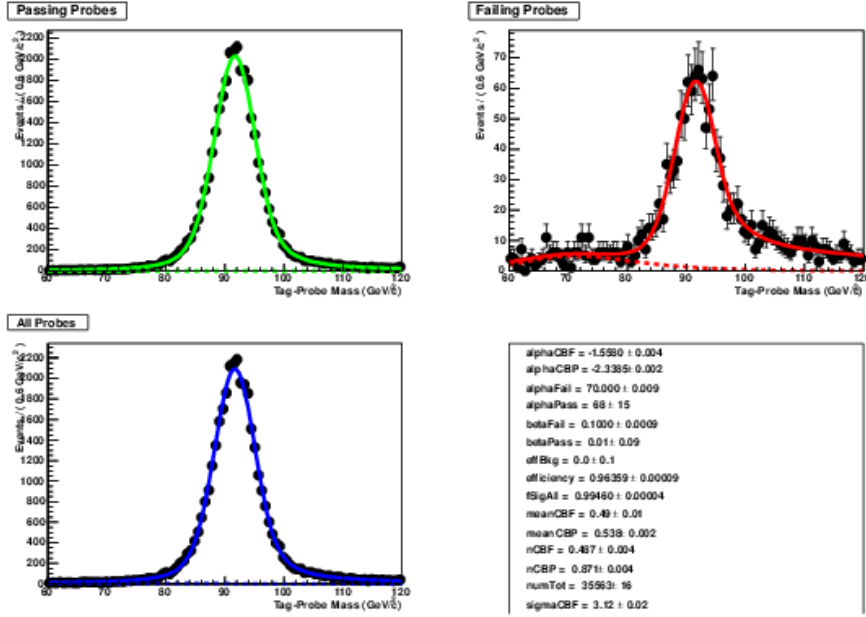


Figure 6.1. Fitting of super-cluster to GSF Electrons for ϵ_{RECO} calculation.

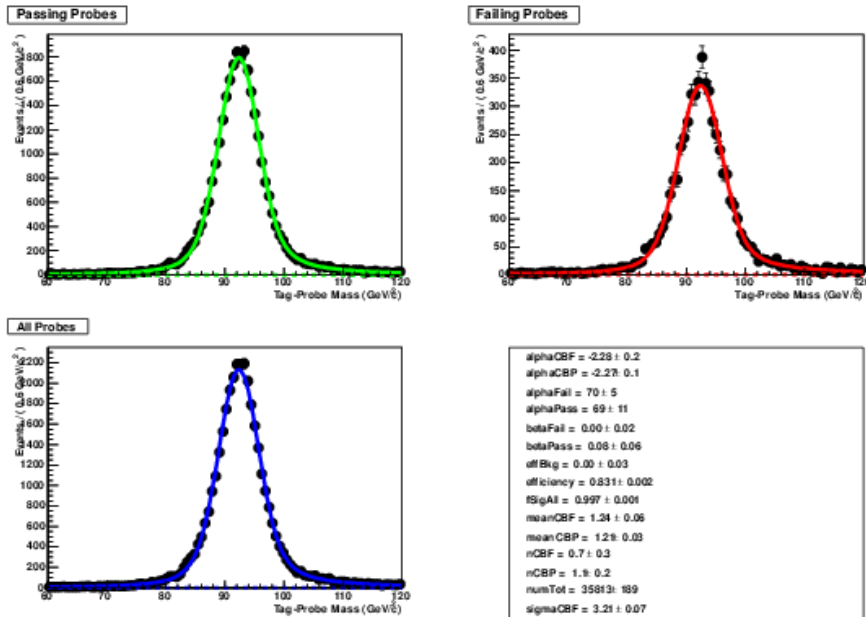


Figure 6.2. Fitting of GSF Electrons for ϵ_{ISO} calculation.

uncertainty on the JES is computed by shifting the p_T of the jets $\pm 1\sigma$ with respect to the measured JES. This shifting of the jet p_T changes the p_T spectrum of the jet which

effects the dijet invariant mass, and ultimately the reconstructed Higgs boson mass. Table 6.4 shows the uncertainty for a range of generated Higgs mass samples. The effect of jet resolution uncertainty on the signal was done by smearing a sub-sample of jets in a sample and looking at the difference between smeared and non smeared events. The effect was negligible. The background is evaluated from data so there should not be a significant effect on those events.

Table 6.4
Jet energy scale (JES) uncertainty for a variety of Higgs boson masses.

M_H GeV	JES -1 σ	JES +1 σ
230	-4.17%	4.26%
300	-1.30%	1.33%
400	-1.20%	1.23%
600	0.86%	0.79%
800	1.10%	1.08%
1000	1.21%	1.16%

6.1.3 b-Tagging

Scale factors between data and simulation have been measured for events with b-jets in bins as a function of p_T and η . This solves the problem that b-jets are more correctly identified in Monte Carlo simulation than they are in data. Also, a mis-tag rate scale factor is calculated when light-quark and gluon jets are tagged as jets from the hadronization of heavy quarks. For the systematic effects, both the scale factor for tagging (SF_b) and scale factor for mis-tags ($SF_{mis-tag}$) are varied up and down by the uncertainty related to each SF. In the analysis, the exact systematic uncertainty (computed as a function of the Higgs mass) is applied.

6.1.4 MET uncertainty

When looking at MET uncertainty, the bulk of the effect comes from our knowledge of the rest of the event, primarily jet energy reconstruction and pile-up. As both of these uncertainties are treated already, much of the MET uncertainty is already taken into account. In signal and Z+jets background there is no real MET, but it is expected to be seen in $t\bar{t}$ events. The uncertainty is found by subtracting the $t\bar{t}$ MC contribution from both data and simulation, and then looking at the differences between the two. In addition, we look at how much of the MET re-scaling described in section 5.5 affects the signal selection efficiency. This is done by counting the number of signal events that cross the final MET cut that we use. This equates to about $\sim 0.5\%$ uncertainty on the final efficiency.

6.1.5 Pile-up

The number of true interactions per bunch crossing in the simulated samples is re-weighted to match the distributions in data. The uncertainty on the measurement of the amount of pile-ups in data is applied to this analysis. This can modify the signal efficiency in primarily two ways. First, there are additional particles in the jets which will change the reconstructed four-momentum. Second, this will introduce a bias in the lepton isolation variables and lower the efficiency in the lepton requirements. This uncertainty is studied by re-estimating the number of true interactions in data with different values of minimum-bias cross section as input. We use 65.84 mb and 72.77 mb as recommended by the CMS pile-up group [79], which corresponds to a $\pm 5\%$ difference with respect to the central value 69.30 mb. The re-estimated distributions and the central value are compared in Figure 6.3. The number of true interactions are re-weighted in the MC to match the shifted distributions in data and then we recompute the signal efficiency. This leads to a change in the signal efficiency $< 1\%$ for the 0- and 1-btag categories, and about 2% for the 2-btag category, for $m_H < 650 GeV$,

approximately independent of lepton channel. These numbers and additional details can be seen in Appendix D.

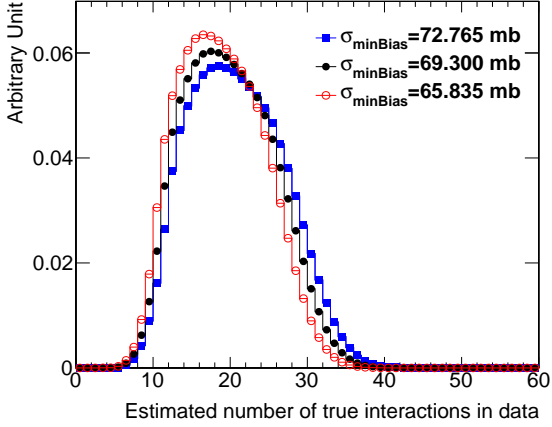


Figure 6.3. Estimated number of true interactions in 2012 data, assuming different values of minimum-bias cross section. The central value is 69.3 mb (solid circles).

6.1.6 Production mechanism

The expected kinematics of the Higgs production is subject to uncertainties due to limited knowledge of the underlying parton distribution functions (PDFs) as well as the shortcomings in the theoretical prediction (missing higher orders in the perturbation series). These uncertainties are propagated to an uncertainty on the selection acceptance and efficiency. Their additional effect on the Higgs production cross section is discussed in a separate section below.

The PDF uncertainties are evaluated according to the PDF4LHC recommendations [80], by computing the selection efficiency for the following PDF sets: cteq66 [81], MSTW2008NLO [82] and NNPDF2.1 [83] and their error sets. The envelope of the various PDF sets is used as the total uncertainty, as recommended, and amounts to 1-4%. The uncertainty noticeably increases for very high Higgs masses. A summary

of systematic uncertainties on the signal acceptance following PDF4LHC recommendations can be found in table 6.5.

Table 6.5
Systematic uncertainties on the signal acceptance following PDF4LHC recommendations.

PDF	m_H (GeV)				
	200	400	600	800	1000
CTEQ66	+0.6% -0.7%	+0.8% -1.0%	+0.8% -1.1%	+1.5% -2.0%	+2.6% -3.2%
MSTW2008NLO	-0.2% -0.5%	+0.6% +0.2%	+0.8% +0.4%	+1.5% +0.7%	+2.5% +1.2%
NNPDF2.1	+0.8% +0.2%	+1.4% +0.75%	+1.5% +0.9%	+2.7% +1.4%	+4.3% -2.4%
Total	+0.8% -0.7%	+1.4% -0.8%	+1.5% -1.1%	+2.7% -2.0%	+4.3% -3.2%

Additional uncertainties arise due to the theoretically calculated Higgs signal shape. The shape uncertainty is evaluated in the recommended way for the Higgs decaying into a pair of Z boson, correctly accounting for the correct line-shape (i.e. re-weighting of the given shape in POWHEG) which also accounts for interference effects. The full description of the re-weighting and uncertainty method is given in [84] and provides an uncertainty that contributes in two ways. Due to the mass-dependence of the selection efficiency, the total signal efficiency is affected by the line-shape. This uncertainty is negligible below 400 GeV and rises to $\sim 3\%$ at 600 GeV, with only small dependence on btag category.

The line-shape used in the CLs procedure is re-extracted with the alternative line-shape models (Figure 6.4 (left)). The tail caused by mismatched jets is not affected at all, as it is a random mixture of events, averaging out any shifts from the uncertainty. The core of the signal distribution is only weakly affected by the uncertainty. In

the worst case (the highest mass we consider), the peak-position shifts by $\sim 2\text{GeV}$ (compared to a sigma of 60 GeV) and the sigma changes by $\sim 1\text{GeV}$. Due to the minuscule effect of this uncertainty, it is not propagated further.

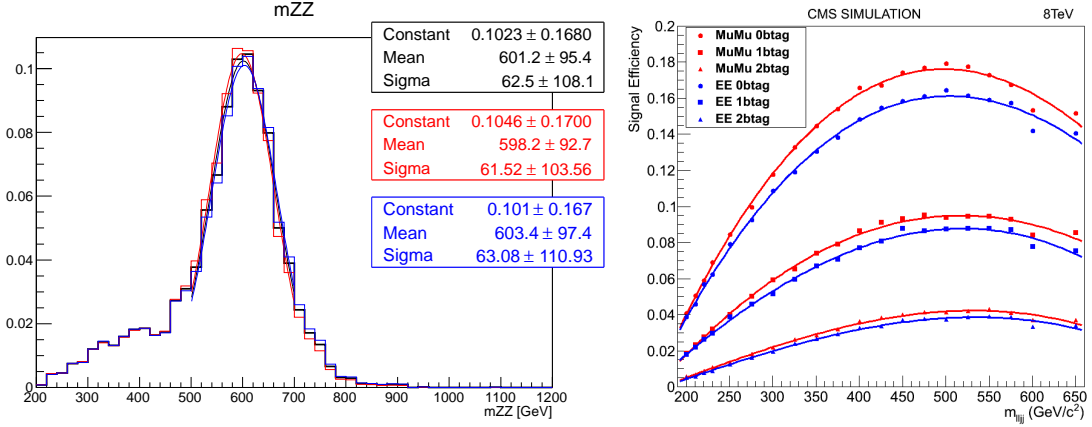


Figure 6.4. Left: reconstructed $m_H = 600\text{GeV}$ Higgs signal (area normalized) with the nominal line-shape (black) and systematic variations (blue/red). Gaussian fits to the core of the distribution are overlaid. Right: parameterization of the signal efficiencies, as function of the Higgs mass hypothesis, in the three btag categories, and the muon and electron channels.

6.1.7 Luminosity uncertainty

The latest recommendation for the 2012 data sets is the uncertainty on LHC luminosity of 4.4% [85].

Higgs cross section and branching fractions

The Higgs production cross section uncertainty depends on production mechanisms, either gluon fusion or vector boson fusion (VBF). However, since the gluon fusion mechanism dominates, it drives the total uncertainty. We use gg and VBF errors separately and for each mass point according to Yellow Report prescription [59].

The total weighted error is in the range 13–15%. This uncertainty does not affect the absolute cross section measurement.

6.2 Background systematic uncertainties

The main systematic uncertainties on the background normalization and shape are summarized in Table 6.6.

6.2.1 Background normalization uncertainties

Lepton trigger and reconstruction uncertainties yield a 2% variation in the normalization of the $M_{\ell\ell jj}$ spectrum. Uncertainties on the muon momentum scale, electron energy scale, pile-up re-weighting and the MET re-scaling procedure have a negligible impact. JES uncertainty causes an uncertainty on the normalization of 5.5%. The uncertainty on the scale factors for the b-tagging efficiency has an effect on the normalization of 0.4%, 0.8% and 4.5% for the 0-, 1- and 2-btag categories respectively. The uncertainty on the b-tagging mis-tag rates introduces an uncertainty in the normalization of 1.9%, 7.8% and 6.2% for the 0-, 1- and 2-btag categories respectively.

6.2.2 Background shape uncertainties

The impact on the $M_{\ell\ell jj}$ distributions of the uncertainties affecting the shape is displayed in Figures 6.5 and 6.6. Jet energy scale causes a $M_{\ell\ell jj}$ -dependent uncertainty varying from almost 0 at low mass, up to 4% at 600 GeV.

To estimate the impact of the $p_T^{\ell\ell jj}$ correction, we compare the $M_{\ell\ell jj}$ Z+jets background distributions with and without the correction. A mass-dependent systematic uncertainty is obtained as the difference of those distributions and goes up to 3% at high $M_{\ell\ell jj}$ values.

Table 6.6
Summary of systematic uncertainties on the normalization and shape
of the background determination.

Source	Normalization	Shape
Muon trigger & ID	2.7%	
Muon momentum scale	0.1%	
Electron trigger & ID	2.0%	
Electron energy scale	0.5%	
Jet energy scale	5.5%	0-4%
<i>b</i> -tagging efficiency SF 0-tag	+0.4%	
<i>b</i> -tagging efficiency SF 1-tag	-0.8%	
<i>b</i> -tagging efficiency SF 2-tag	-4.5%	
Mis-tag SF 0-tag	-1.9%	
Mis-tag SF 1-tag	+7.8%	
Mis-tag SF 2-tag	+6.2%	
MET	0.3%	
Pile-up	0.1%	
$p_T^{\ell\ell jj}$ re-weighting	0.8%	0-3%
Diboson cross section	15%	
Luminosity	4.4%	
Residual difference data-background in control region		0-15% (0-btag) 0-30% (1-btag) 0-40% (2-btag)

Residual differences in the $M_{\ell\ell jj}$ distributions between the data and the background in the m_{jj} sideband control region are taken as an additional mass-dependent systematic uncertainty. Those residual differences are plotted in Figure 6.7 (top). In order to smooth out the fluctuations, a linear variation as shown in the figure is used to incorporate this effect into alternative templates for the background predic-

tion. The resulting alternative templates, around the nominal template, are shown in Figure 6.7 middle and bottom, for the electron and muon channels respectively.

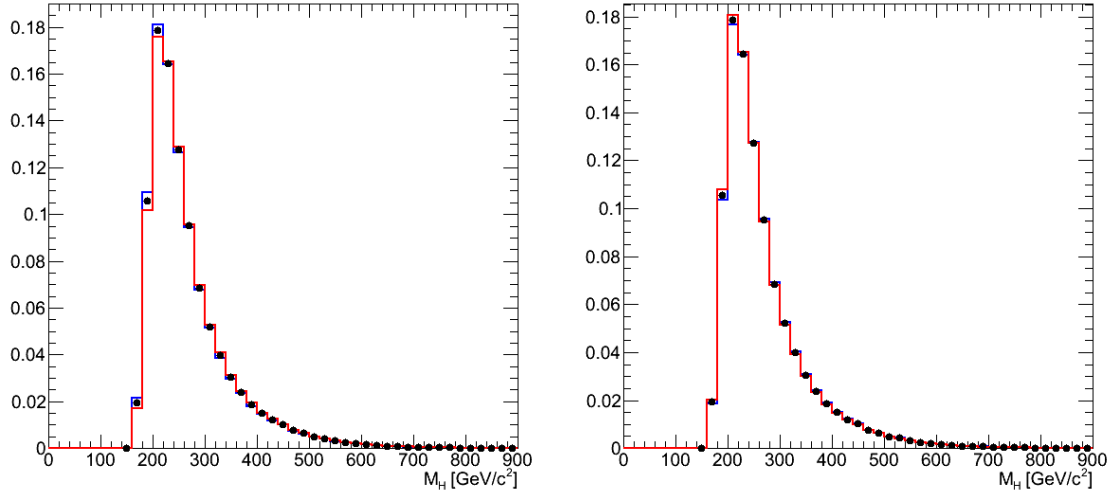


Figure 6.5. Shape variation of the $M_{\ell\ell jj}$ distribution for Z+jets simulated events when varying the systematic uncertainties: (left) jet energy scale, (right) $p_T^{\ell\ell jj}$ -based re-weighting. Black dots denote the reference shapes. Red and blue histograms indicate the up and down variations of the corresponding systematic uncertainties.

6.2.3 Upper and Lower Side Band Comparison

We re-weight the Z+Jets MC in the signal region as seen in Appendix G. In order to estimate how MC reproduced the shape in data for the sideband we plot both data-MC and the ratio $\frac{data}{MC}$. In particular, we also compare the shapes in the lower and upper sidebands to get a more accurate picture of the shape. This gives a more accurate representation of the error in the background than looking at the shape difference between m_{jjll} p_T re-weighted and m_{jjll} non p_T re-weighted. The exclusive Z+Jets samples (1-4 jets) are $m_{jjll}p_T$ re-weighted. The data and MC are normalized to unity before comparisons. The plots for all three categories are shown in Figures 6.8, 6.9, and 6.10.

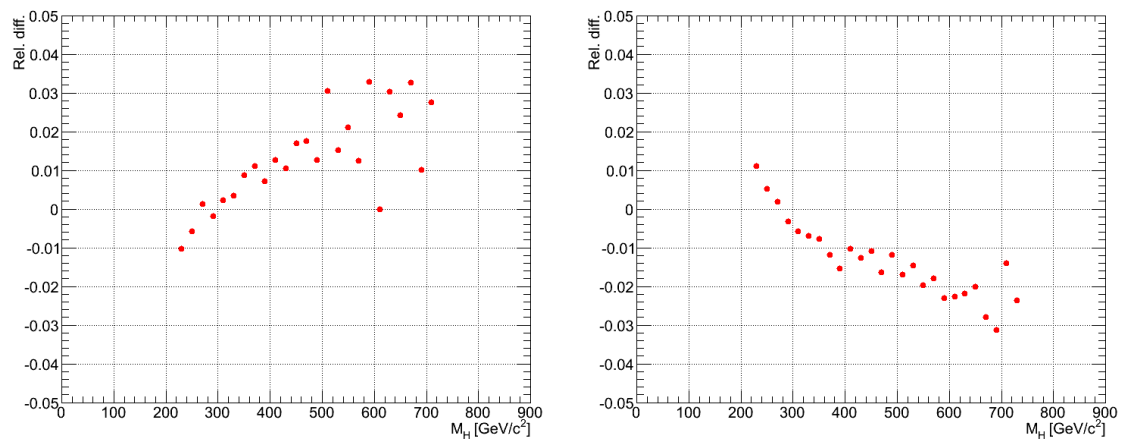


Figure 6.6. Relative difference on the shape of the $M_{\ell\ell jj}$ distribution for $Z+jets$ simulated events when varying the systematic uncertainties: (left) jet energy scale, (right) $p_T^{\ell\ell jj}$ -based re-weighting.

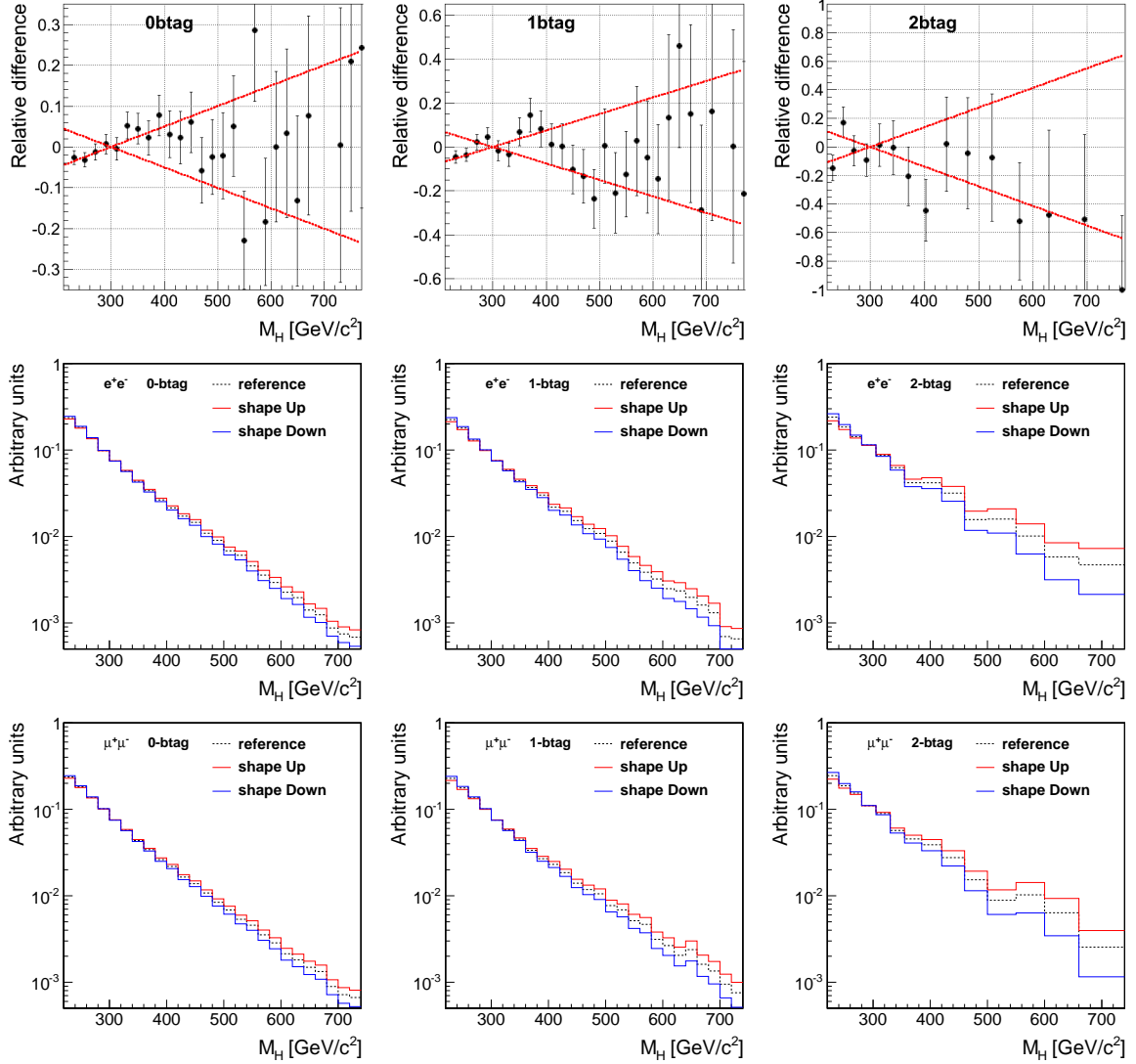


Figure 6.7. Residual differences in the $M_{\ell\ell jj}$ distributions between the data and the background, in the M_{jj} sideband control region (top). Alternative templates for the background prediction taking into account those residual variations, for the electron (middle) and the muon channels (bottom).

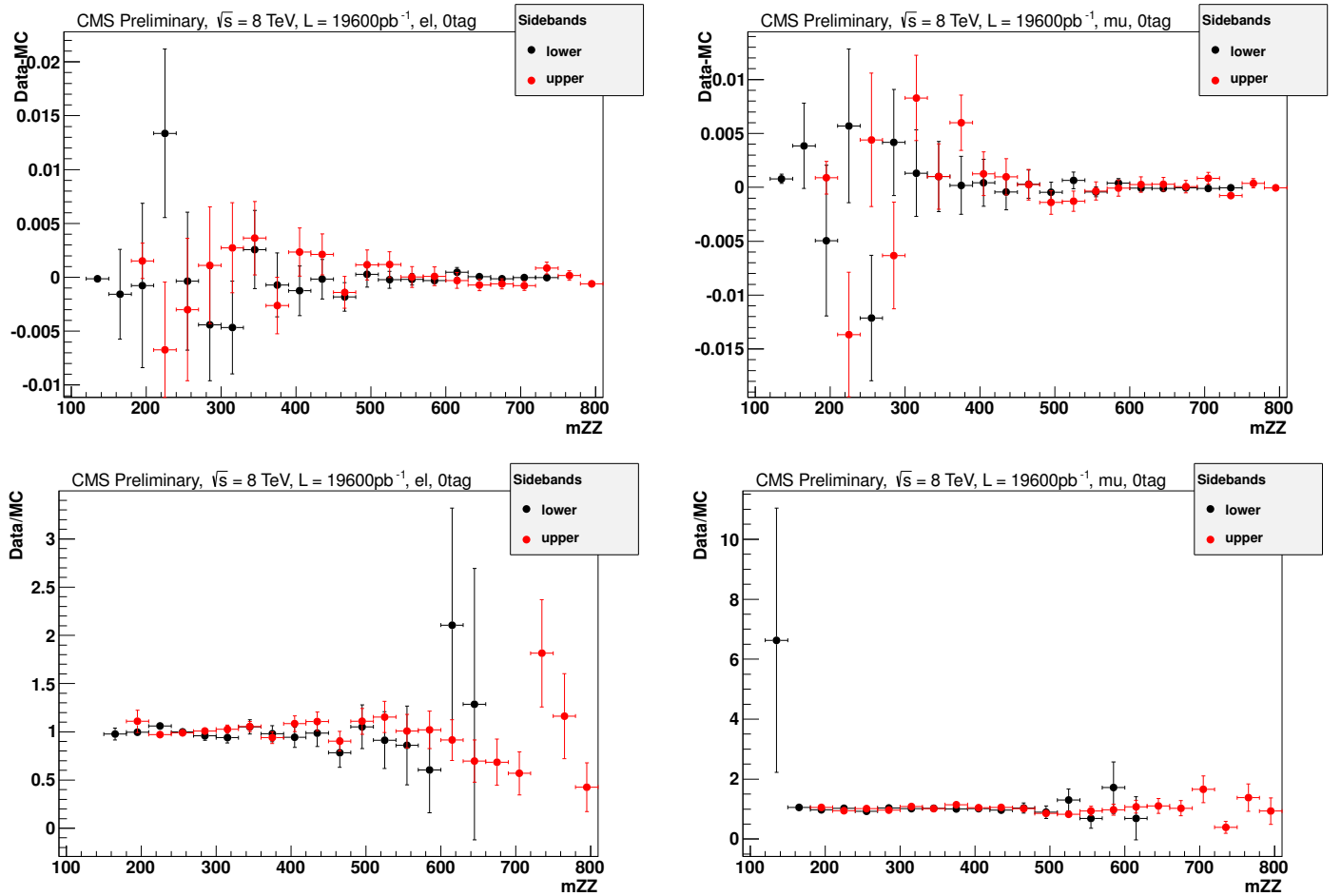


Figure 6.8. Comparing Data and MC in the 0 btag regions for both the upper sideband and lower sideband regions. Data and MC are first normalized to unity before the comparisons. All plots are a function of the mass of the two Zs. Top left: Data - MC for electrons. Top right: Data - MC for muons. Bottom left: Data/MC for electrons. Bottom right: Data/MC for muons.

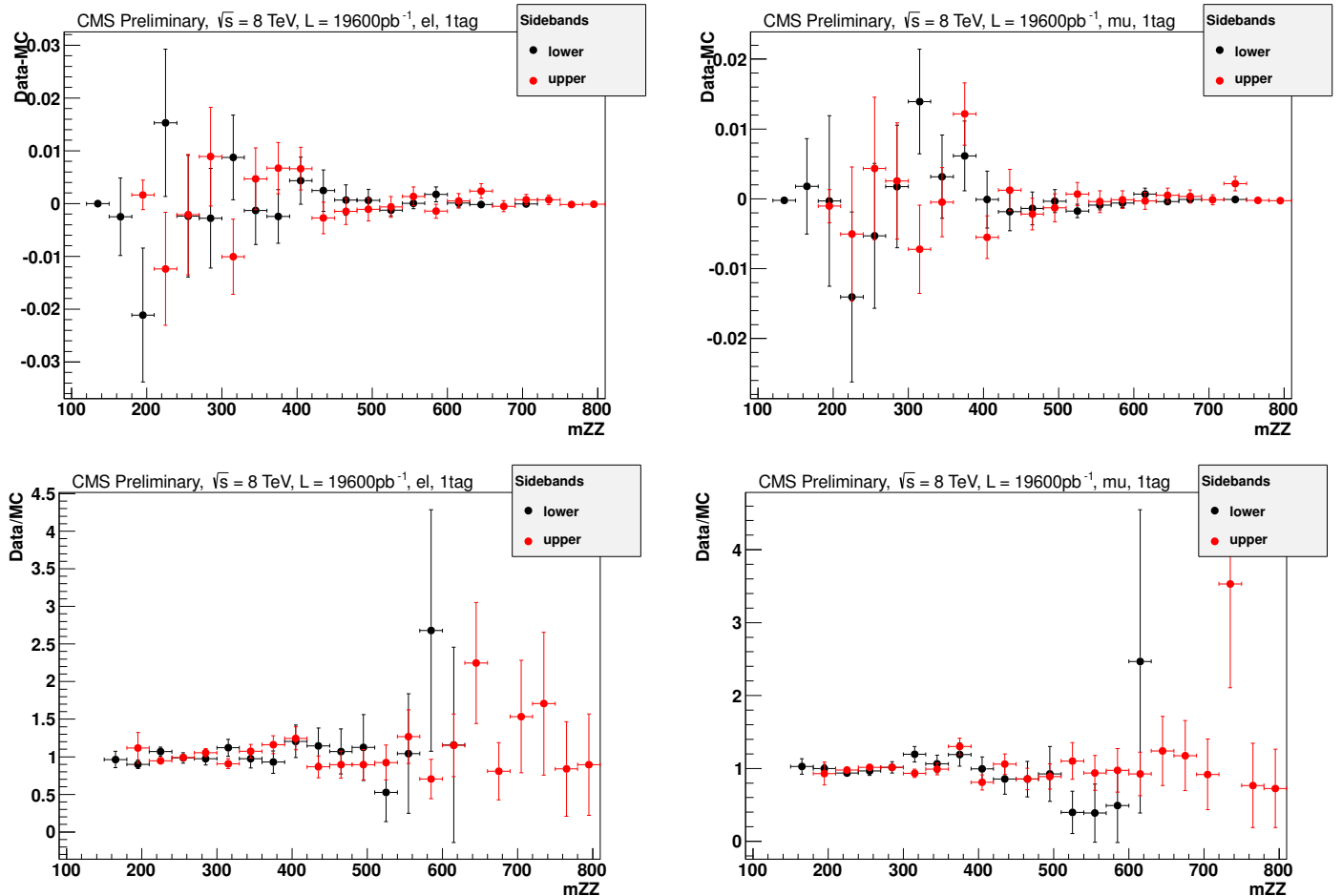


Figure 6.9. Comparing Data and MC in the 1 btag regions for both the upper sideband and lower sideband regions. Data and MC are first normalized to unity before the comparisons. All plots are a function of the mass of the two Zs. Top left: Data - MC for electrons. Top right: Data - MC for muons. Bottom left: Data/MC for electrons. Bottom right: Data/MC for muons.

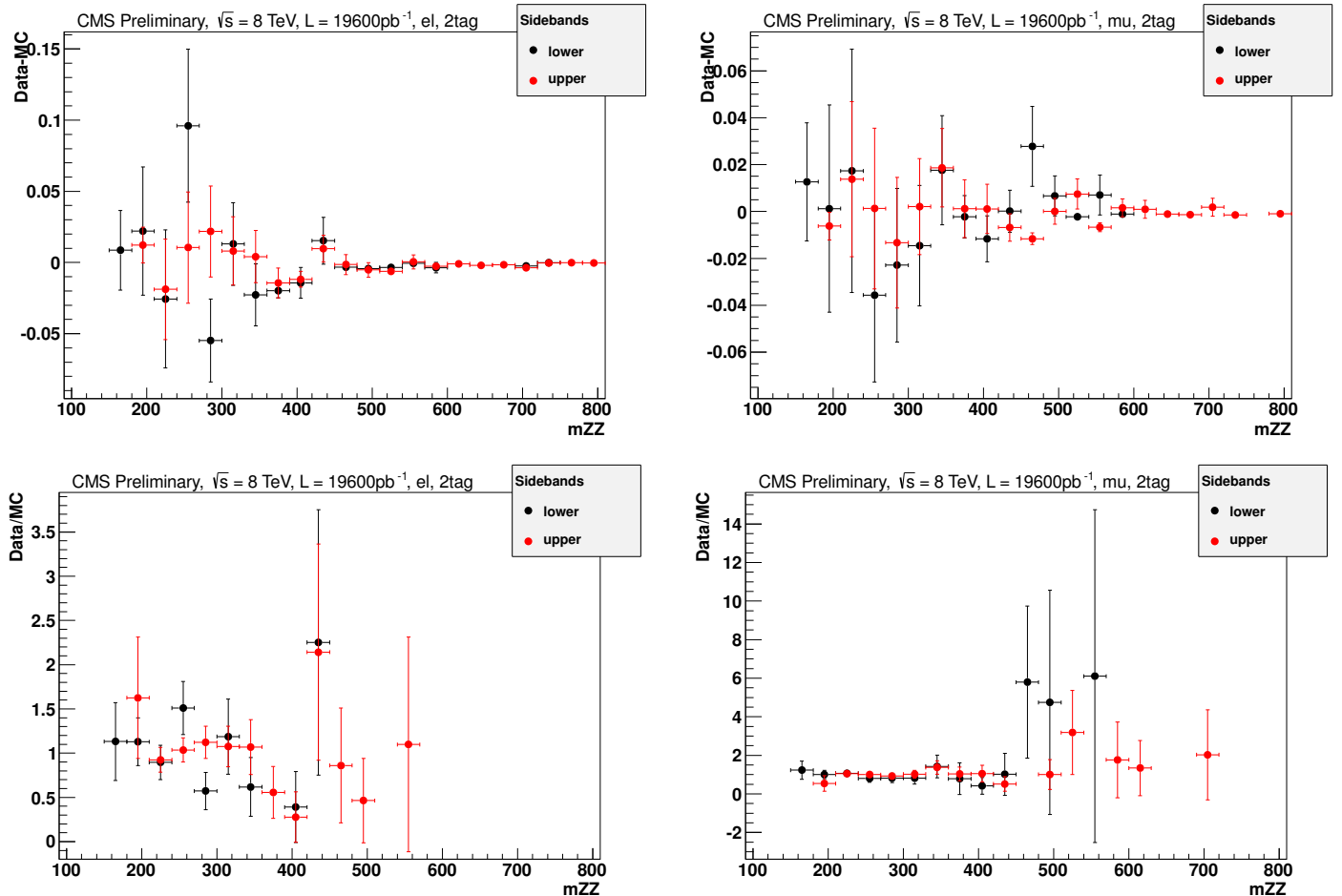


Figure 6.10. Comparing Data and MC in the 2 btag regions for both the upper sideband and lower sideband regions. Data and MC are first normalized to unity before the comparisons. All plots are a function of the mass of the two Zs. Top left: Data - MC for electrons. Top right: Data - MC for muons. Bottom left: Data/MC for electrons. Bottom right: Data/MC for muons.

7. Statistical interpretation and results

7.1 Signal determination

The signal efficiency of the selection is evaluated as the ratio between the number of selected events in each of the six channels (electron and muon channels, 0-, 1-, and 2-btag categories) under study and the total number of generated events in the Monte Carlo samples. The signal efficiency as a function of the Higgs mass is fitted to a polynomial in order to be estimated for those Higgs mass hypothesis where no Monte Carlo sample is available, as shown in Figure 7.1.

The narrow width approximation breaks down at high Higgs mass (typically $> 400\text{GeV}$) due to the very large Higgs width ($> 70\text{GeV}$). A more correct approach to describe the Higgs invariant-mass distribution has been proposed, known as Complex Pole Scheme (CPS) [86]. The total Higgs production cross section has been recomputed by the Higgs Cross Section Working Group to include the corrections due to CPS at high Higgs mass [87]. In this analysis the simulated signal samples are properly re-weighted to follow the CPS.

At high Higgs mass the interference between the Higgs signal and the $gg \rightarrow ZZ$ background becomes large [88]. The effect of interference has been shown to be constructive below the Higgs mass peak and destructive above. It therefore has a negligible effect on the total cross section (1-2%) but it biases the ZZ invariant-mass distribution. Moreover the interference has been computed only at LO (leading order) while the signal is known at NNLO (next to next to leading order). In this analysis the uncertainty due to missing higher perturbative order on the interference and the simulated line-hape is also corrected in the re-weighting [88].

After this is done, the obtained distribution should reflect the expectation for the Higgs events, both in yield and shape. This re-weighting has been included in the analysis in order to account for the correct distributions.

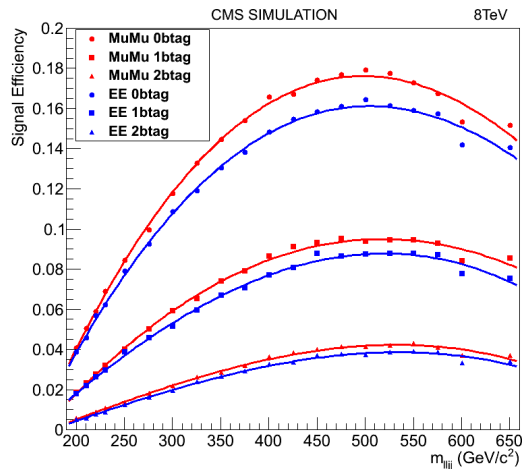


Figure 7.1. Parameterization of signal efficiency as a function of Higgs mass hypothesis in 0-btag (left), 1-btag (middle), 2-btag (right) categories and in the muon (top) and electron (bottom) channels.

7.2 Results

Since the decay products of the Higgs boson can be fully reconstructed, it is possible to use the reconstructed Higgs boson mass distribution to discriminate Higgs signal events against background events. The reconstructed mass will peak around the true Higgs boson mass, m_H , for the signal, while for background processes it will have a broader distribution. Consequently, a shape-based treatment of the expected and observed distribution of the invariant mass of the Higgs candidate (i.e. the 4-object mass) increases the sensitivity of the analysis, compared to a simpler counting experiment. Since the expected shape of the background and the signal cannot be obtained from first principles, an analytic function cannot be used. Therefore, a binned histogram-based calculation has been used for the shape analysis.

The normalization of the simulated background ($Z+jets$ and diboson) in the signal region is allowed to vary. The constraints come from the number of events in the m_{jj} sideband in data. The signal-free regions of the $M_{\ell\ell jj}$ distribution impose an additional constraint to the background normalization. The observed and expected numbers of events in the sideband region are given as input to the limit calculation tool. The calculation to discriminate signal from background events is performed independently for the six individual analysis channels (electrons and muons in the 0, 1, and 2-btag categories), and then combined taking into account the correlations among the systematic uncertainties. These uncertainties may affect either the shape of the distributions or their normalization, and are properly taken into account in the statistical analysis.

The mass distributions of the $\ell^+\ell^-jj$ system are depicted in Figures 7.2 and 7.3 for data in the signal region. The statistical uncertainty on the background is much smaller than the statistical uncertainty on the data, as the number of $Z+jets$ simulated events used to estimate this background corresponds to a luminosity from 5 to 10 times larger. The full dataset (19.6 fb^{-1}) is used to assess the good modeling of the background in the m_{jj} sideband region (Figures 7.4 and 7.5). Residual differences are taken as a systematic uncertainty, as explained in the previous section. As a cross check, the $M_{\ell\ell jj}$ distributions for the electron and muon channels are studied separately, both in the m_{jj} sideband and signal regions. They show an excellent agreement as can be seen in Appendix G.

Expected upper limits on the SM Higgs boson production cross section are determined as function of the Higgs boson mass hypothesis, taking as input the $M_{\ell\ell jj}$ distribution for data, and for the background and signal expectations. The statistical procedure, based on the profile likelihood method, uses the *asymptotic* CL_s [89] approach, implemented in the official tool developed by the CMS Higgs combination group [90]. Systematic uncertainties are treated as nuisance parameters.

The results are expressed as upper limits on the ratio of the cross section times branching fraction of the process $H \rightarrow ZZ \rightarrow \ell^+\ell^- q\bar{q}$, divided by the expectation for

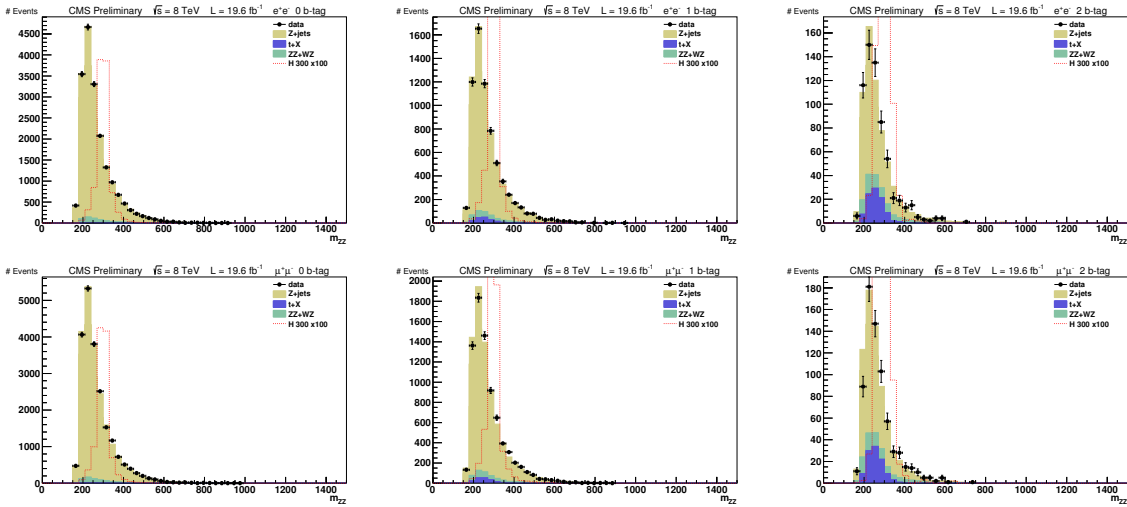


Figure 7.2. Mass distributions of the $\ell^+\ell^-jj$ system for events in the signal region in the electron (top) and muon (bottom) channels. From left to right, plots correspond to the 0-, 1-, and 2-btag categories.

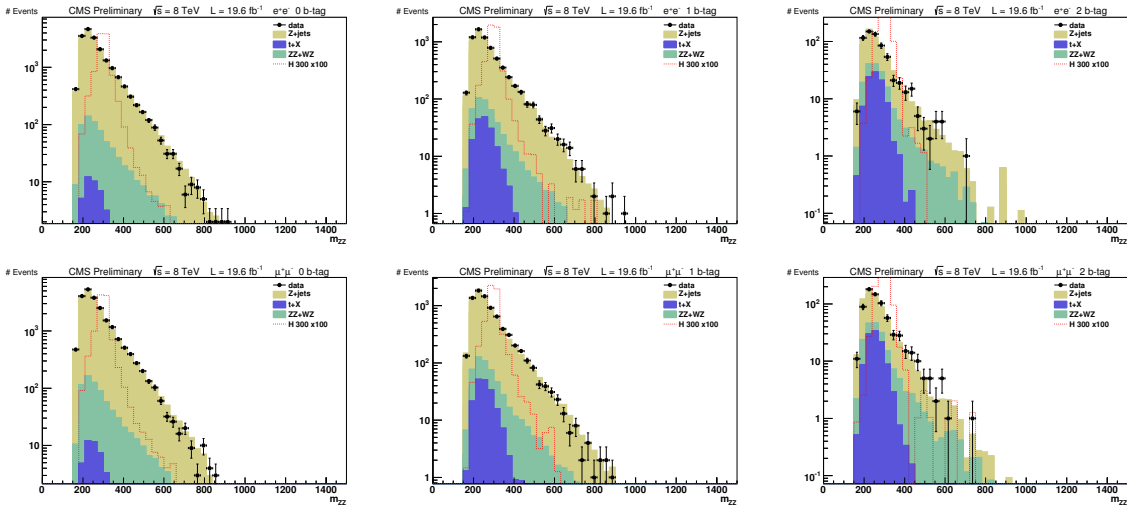


Figure 7.3. Mass distributions of Figure 7.2 in logarithmic scale.

the standard model Higgs boson, $\sigma/\sigma_{\text{SM}}$. A particular Higgs boson mass hypothesis is excluded whenever $\sigma/\sigma_{\text{SM}} < 1$. The observed limit on $\sigma/\sigma_{\text{SM}}$ is determined for m_H

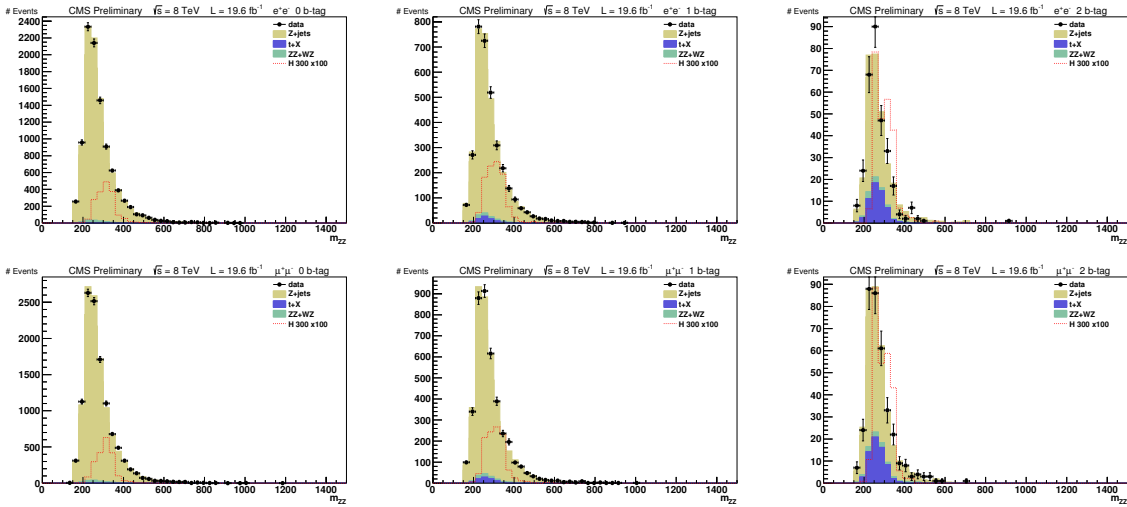


Figure 7.4. Mass distributions of the $\ell^+\ell^-jj$ system for events in the m_{jj} sideband region in the electron (top) and muon (bottom) channels. From left to right, plots correspond to the 0-, 1-, and 2-btag categories.

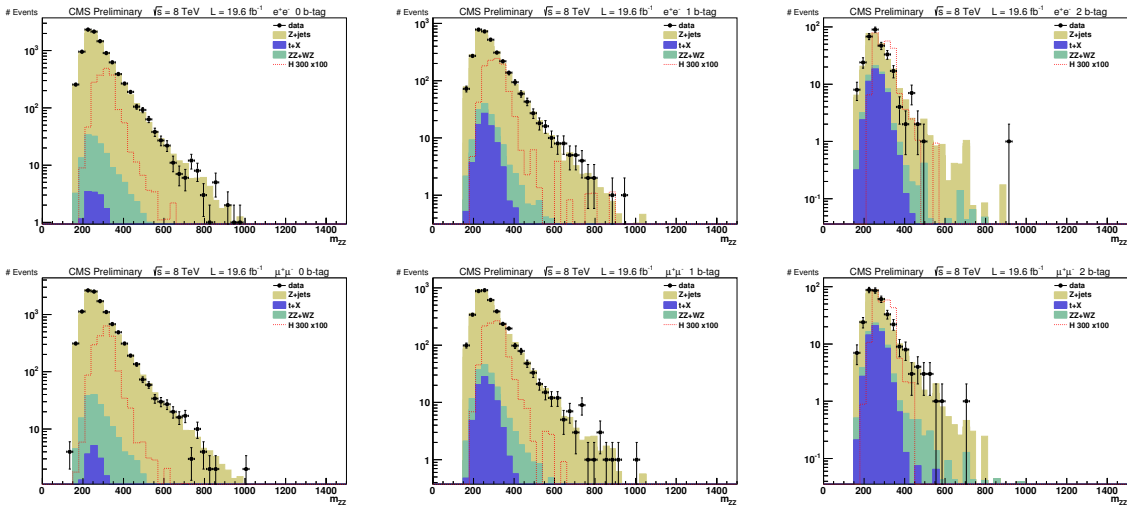


Figure 7.5. Mass distributions of Figure 7.4 in logarithmic scale.

hypotheses between 230 GeV and 650 GeV, using $M_{\ell\ell jj}$ distributions defined in the range from 220 GeV to 800 GeV. The $M_{\ell\ell jj}$ region below 220 GeV presents a very sharp rising edge from Z+jets which is difficult to have under control and is excluded from the analysis.

Figure 7.6 shows the expected and observed limits for the full dataset recorded during 2012 at 8 TeV, corresponding to a luminosity of 19.6 fb^{-1} . With the increased luminosity in this dataset the 2-btag category becomes the most powerful contribution to the combination of the six channels (Figure 7.7). These results were cross-checked with an independent statistical method (Appendix H).

Limits on the SM production cross section times branching fraction for $H \rightarrow ZZ$ are presented in Figure 7.8. For comparison, expectations are shown for a SM-like Higgs boson. In addition, the limits as observed in this study are combined with the results of the previous analysis on the 2011 data sets [91], as shown in Figure 7.9.

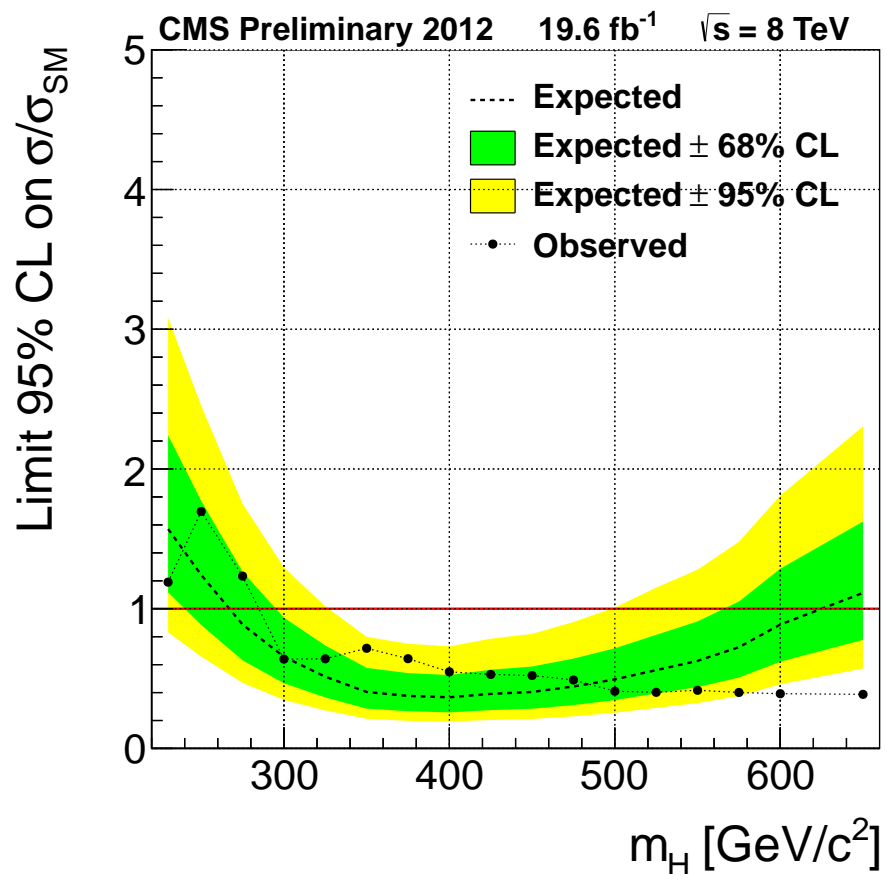


Figure 7.6. Observed (solid) and expected (dashed) 95% CL upper limit on the ratio of the production cross section to the SM expectation for the Higgs boson obtained using the CL_s technique. The 68% and 95% ranges of expectation for the background-only model are also shown with green and yellow bands, respectively. The solid line at 1 indicates the expectation for a SM-Higgs-like boson. The plot shows the expected and observed limits using 19.6 fb⁻¹ of data.

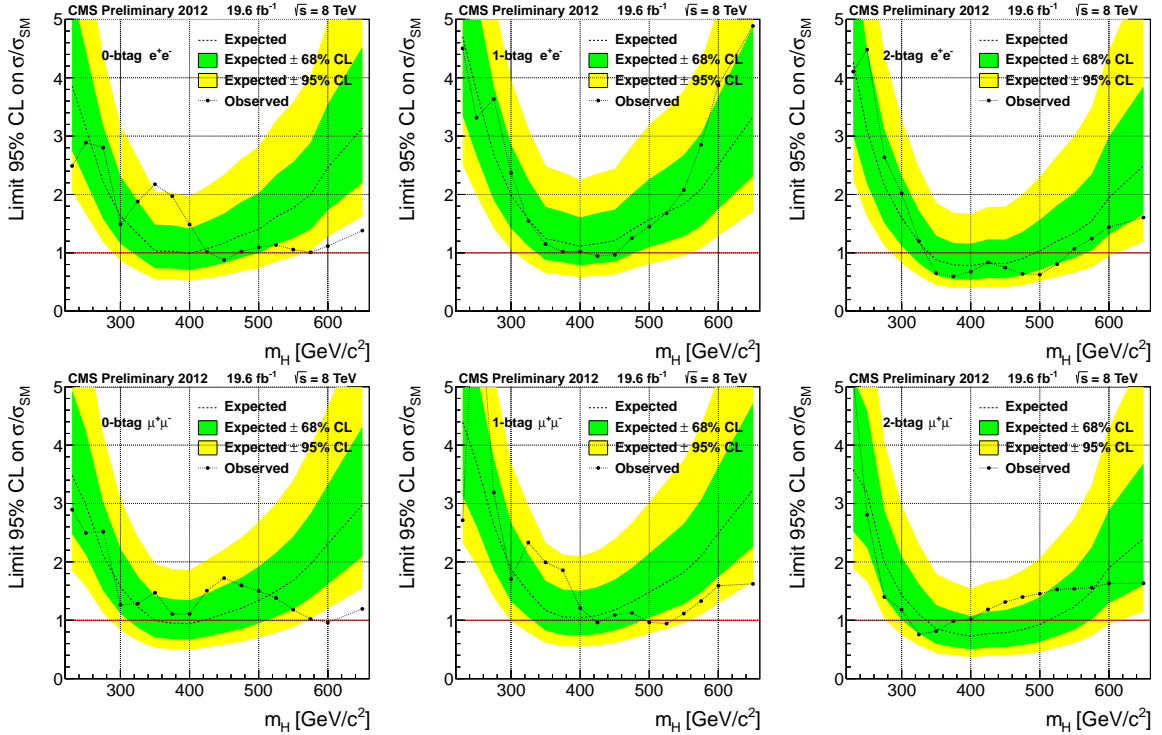


Figure 7.7. Observed (solid) and expected (dashed) 95% CL upper limit on the ratio of the production cross section to the SM expectation for the Higgs boson obtained using the CL_s technique, separate for the different lepton flavor and b-tag categories. The 68% and 95% ranges of expectation for the background-only model are also shown with green and yellow bands, respectively. The solid line at 1 indicates the expectation for a SM-Higgs-like boson.

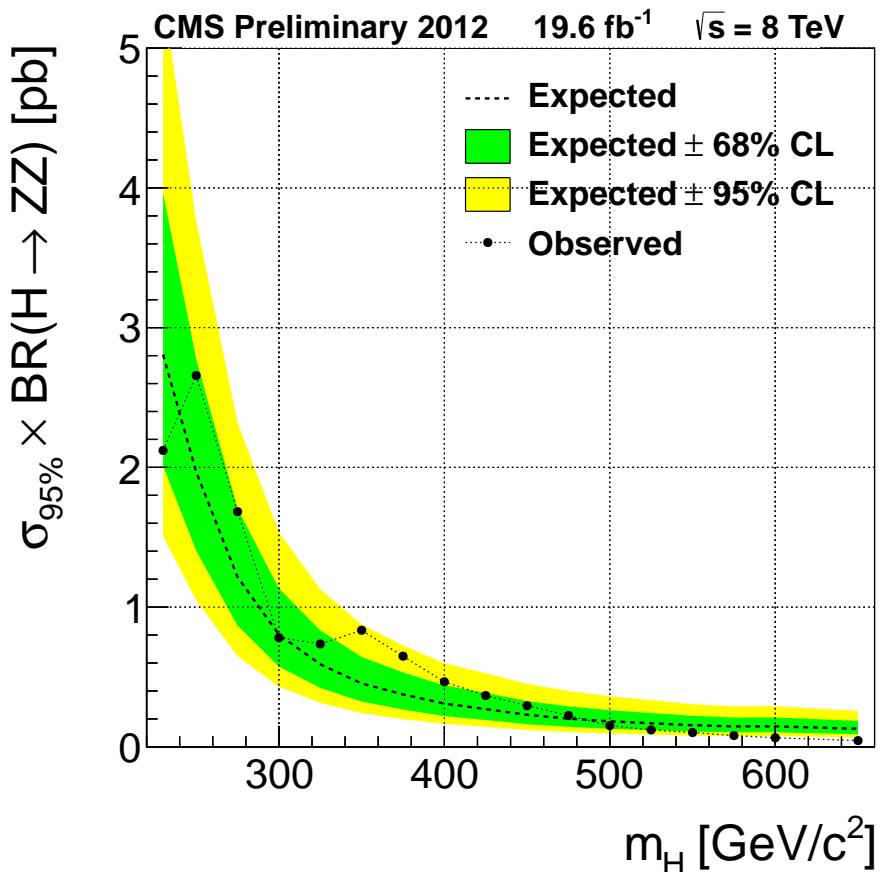


Figure 7.8. Observed (solid) and expected (dashed) 95% C.L. upper limit on the product of the production cross section and branching fraction for $H \rightarrow ZZ$ obtained with the CL_s technique. The 68% and 95% ranges of expectation for the background-only model are also shown with green and yellow bands, respectively. The left plot shows the observed limit only at the points where the signal shape can be directly obtained from the simulation.

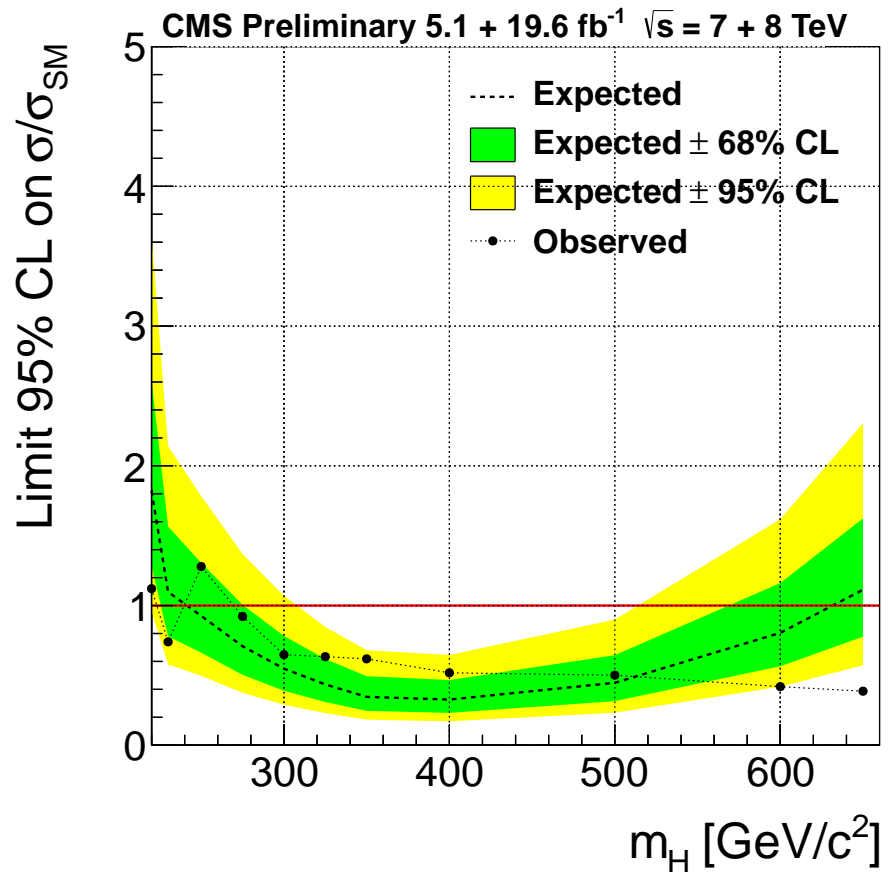


Figure 7.9. Observed (solid) and expected (dashed) 95% CL upper limit on the ratio of the production cross section to the SM expectation for the Higgs boson obtained using the CL_s technique. The 68% and 95% ranges of expectation for the background-only model are also shown with green and yellow bands, respectively. The solid line at 1 indicates the expectation for a SM-Higgs-like boson. This result is the combination of this study (i.e. Figure 7.6) with the previous 2011 results.

8. Conclusion

We have performed a search for a SM-like Higgs boson in the decay channel $H \rightarrow ZZ \rightarrow \ell^+\ell^-q\bar{q}$. This decay mode is relevant at high mass (200 to 650 GeV) and contributed significantly in a region that has not been probed before the LHC in any laboratory. The data samples analyzed are those collected by the CMS experiment in 2012 with an integrated luminosity corresponding to 19.6 fb^{-1} at 8 TeV, combined with those previously collected in 2011 with an integrated luminosity of 5.1 fb^{-1} at 7 TeV.

No evidence for a Standard Model Higgs boson has been found and the upper limits on the Higgs boson production cross section between 200 and 650 GeV have been computed. In addition, the analysis excludes the existence of a standard-model-like Higgs boson in the mass range between 285 GeV to 650 GeV, where the expected exclusion range goes from 266 GeV to 626 GeV.

In the near future, this analysis will be extended in the high-mass region up to 1 TeV. This analysis also sets a benchmark for other analysis and could be extended for the search of exotic, spin-2 particles, the Graviton, and other Standard Model Higgs-like particles.

APPENDICES

A. Data and Monte Carlo samples

Table A.1
Data samples used in the analysis.

Channel	Dataset	Luminosity [pb ⁻¹]
$2\mu 2q$	/DoubleMu/Run2012A-13Jul2012-v1/AOD	808
	/DoubleMu/Run2012A-recover-06Aug2012-v1/AOD	82
	/DoubleMu/Run2012B-13Jul2012-v4/AOD	4429
	/DoubleMu/Run2012C-24Aug2012-v1/AOD	495
	/DoubleMu/Run2012C-EcalRecover_11Dec2012-v1/AOD	134
	/DoubleMu/Run2012C-PromptReco-v2/AOD	6394
	/DoubleMu/Run2012D-PromptReco-v1/AOD	7274
$2e 2q$	/DoubleElectron/Run2012A-13Jul2012-v1/AOD	808
	/DoubleElectron/Run2012A-recover-06Aug2012-v1/AOD	82
	/DoubleElectron/Run2012B-13Jul2012-v4/AOD	4429
	/DoubleElectron/Run2012C-24Aug2012-v1/AOD	495
	/DoubleElectron/Run2012C-EcalRecover_11Dec2012-v1/AOD	134
	/DoubleElectron/Run2012C-PromptReco-v2/AOD	6394
	/DoubleElectron/Run2012D-PromptReco-v1/AOD	7274
$e\mu qq$	/MuEG/Run2012A-13Jul2012-v1/AOD	808
	/MuEG/Run2012A-recover-06Aug2012-v1/AOD	82
	/MuEG/Run2012B-13Jul2012-v4/AOD	4429
	/MuEG/Run2012C-24Aug2012-v1/AOD	495
	/MuEG/Run2012C-EcalRecover_11Dec2012-v1/AOD	134
	/MuEG/Run2012C-PromptReco-v2/AOD	6394
	/MuEG/Run2012D-PromptReco-v1/AOD	7274

Table A.2

The signal samples, $H \rightarrow ZZ \rightarrow \ell^+ \ell^- q\bar{q}$ ($\ell = e, \mu, \tau$), simulated with POWHEG are `/GluGluToHToZZTo2L2Q_M-xyz_8TeV-powheg-pythia6/Summer12_DR53X-PU_S10_START53_V7A-v1/AODSIM`, where xyz is the Higgs boson mass hypothesis, m_H . The cross section times branching fraction for each m_H value is listed in pb. Each sample was generated with 300,000 events.

m_H (GeV)	$\sigma \times \text{Br}(H \rightarrow ZZ \rightarrow \ell^+ \ell^- q\bar{q})$ [pb]
200	0.2566
210	0.2538
220	0.2416
230	0.2278
250	0.2022
275	0.1751
300	0.1563
325	0.1478
350	0.1482
375	0.1360
400	0.1111
425	0.0914
450	0.7311
475	0.6000
500	0.4719
525	0.0380
550	0.0305
575	0.0250
600	0.0201

Table A.3

Background simulated samples of the Summer12 production used in the analysis. The equivalent luminosity of the processed events for each sample is computed using the (N)NLO cross section in the 3rd column.

Process	dataset	σ [pb]	luminosity [fb^{-1}]
$Z + \text{jets}$ (inclusive)	/DYJetsToLL_M-50_TuneZ2Star_8TeV-madgraph-tarball/ Summer12_DR53X-PU_S10_START53_V7A-v1/AODSIM	3503.71	8.7
$Z + 1 \text{ jet}$ (exclusive)	/DY1JetsToLL_M-50_TuneZ2Star_8TeV-madgraph/ Summer12_DR53X-PU_S10_START53_V7A-v1/AODSIM	660.6	36.4
$Z + 2 \text{ jet}$ (exclusive)	/DY2JetsToLL_M-50_TuneZ2Star_8TeV-madgraph/ Summer12_DR53X-PU_S10_START53_V7A-v1/AODSIM	215.1	101.6
$Z + 3 \text{ jet}$ (exclusive)	/DY3JetsToLL_M-50_TuneZ2Star_8TeV-madgraph/ Summer12_DR53X-PU_S10_START53_V7A-v1/AODSIM	65.79	167.4
$Z + 4 \text{ jet}$ (exclusive)	/DY4JetsToLL_M-50_TuneZ2Star_8TeV-madgraph/ Summer12_DR53X-PU_S10_START53_V7A-v1/AODSIM	27.59	232.1
$t\bar{t}$	/TTTo2L2Nu2B_8TeV-powheg-pythia6/ Summer12_DR53X-PU_S10_START53_V7A-v1/AODSIM	23.38	461
ZZ	/ZZ_TuneZ2star_8TeV_pythia6_tauola/ Summer12_DR53X-PU_S10_START53_V7A-v1/AODSIM	17.654	549
WZ	/WZ_TuneZ2star_8TeV_pythia6_tauola/ Summer12_DR53X-PU_S10_START53_V7A-v1/AODSIM	22.88	424
WW	/WW_TuneZ2star_8TeV_pythia6_tauola/ Summer12_DR53X-PU_S10_START53_V7A-v1/AODSIM	57.1097	168

B. Trigger efficiencies and Monte Carlo correction factors

The trigger efficiencies and MC correction factors used in the analysis are listed in Tables B.1 and B.2 for the electron triggers, and in Table B.3 for the muon trigger.

Table B.1
Working point loose to the HLT Ele8 leg tag-and-probe efficiencies
and scale factors.

η coverage	p_T range (GeV/c)	efficiency (data)	efficiency (MC)	data/MC ratio
0.0 < $ \eta $ < 0.8	$10 < p_T < 20$	0.474 ± 0.009	0.591 ± 0.012	0.801 ± 0.022
0.8 < $ \eta $ < 1.4		0.343 ± 0.008	0.477 ± 0.011	0.718 ± 0.024
1.6 < $ \eta $ < 2.0		0.444 ± 0.014	0.489 ± 0.018	0.909 ± 0.044
2.0 < $ \eta $ < 2.5		0.452 ± 0.015	0.541 ± 0.024	0.836 ± 0.046
0.0 < $ \eta $ < 0.8	$20 < p_T < 40$	0.986 ± 0.001	0.988 ± 0.001	0.997 ± 0.001
0.8 < $ \eta $ < 1.4		0.936 ± 0.001	0.946 ± 0.001	0.990 ± 0.002
1.6 < $ \eta $ < 2.0		0.901 ± 0.002	0.905 ± 0.003	0.995 ± 0.004
2.0 < $ \eta $ < 2.5		0.944 ± 0.002	0.944 ± 0.002	1.000 ± 0.003
0.0 < $ \eta $ < 0.8	$40 < p_T < 200$	0.991 ± 0.001	0.994 ± 0.001	0.997 ± 0.000
0.8 < $ \eta $ < 1.4		0.976 ± 0.001	0.978 ± 0.001	0.998 ± 0.001
1.6 < $ \eta $ < 2.0		0.945 ± 0.002	0.946 ± 0.002	0.999 ± 0.002
2.0 < $ \eta $ < 2.5		0.962 ± 0.002	0.962 ± 0.002	1.000 ± 0.002

As a cross check, we have compared the trigger efficiencies calculated from data with the trigger efficiencies provided by the HLT trigger simulation. Table B.4 shows the trigger simulation efficiencies for the Z+jets and Higgs signal (300 GeV) simulated

Table B.2
Working point loose to the HLT Ele17 leg tag-and-probe efficiencies
and scale factors.

η coverage	p_T range (GeV/c)	efficiency (data)	efficiency (MC)	data/MC ratio
0.0 < $ \eta $ < 0.8	$10 < p_T < 20$	0.955 ± 0.004	0.969 ± 0.004	0.985 ± 0.006
0.8 < $ \eta $ < 1.4		0.852 ± 0.006	0.867 ± 0.007	0.983 ± 0.011
1.6 < $ \eta $ < 2.0		0.839 ± 0.011	0.841 ± 0.013	0.997 ± 0.020
2.0 < $ \eta $ < 2.5		0.868 ± 0.010	0.889 ± 0.015	0.976 ± 0.020
0.0 < $ \eta $ < 0.8	$20 < p_T < 40$	0.983 ± 0.001	0.984 ± 0.001	0.999 ± 0.001
0.8 < $ \eta $ < 1.4		0.932 ± 0.001	0.940 ± 0.001	0.991 ± 0.002
1.6 < $ \eta $ < 2.0		0.895 ± 0.002	0.898 ± 0.003	0.997 ± 0.004
2.0 < $ \eta $ < 2.5		0.933 ± 0.002	0.935 ± 0.003	0.998 ± 0.003
0.0 < $ \eta $ < 0.8	$40 < p_T < 200$	0.989 ± 0.001	0.991 ± 0.001	0.998 ± 0.001
0.8 < $ \eta $ < 1.4		0.972 ± 0.001	0.973 ± 0.001	0.999 ± 0.001
1.6 < $ \eta $ < 2.0		0.938 ± 0.002	0.939 ± 0.002	0.999 ± 0.002
2.0 < $ \eta $ < 2.5		0.951 ± 0.002	0.955 ± 0.002	0.996 ± 0.003

samples. The ratio between the trigger efficiencies calculated from data and the trigger simulation, averaged over η , is 0.94, both for the Z+jets and Higgs signal (300 GeV) simulated samples. This discrepancy can be explained by the missing cut on the longitudinal distance between the two muons (Δz) in the muon trigger simulation. The Muon POG is recalculating the data/MC trigger efficiency scale factors to take this effect into account. It is important to note that we are applying to the MC the trigger efficiencies calculated from data, listed in table B.3, hence this effect is taken into account. In any case, this small discrepancy would only be relevant

Table B.3

Dimuon trigger efficiencies, calculated using the Muon POG official numbers, for two tight muons, both with $p_T > 20$ GeV/c, in four bins of pseudorapidity for each of the two muons.

muon η	$0.0 < \eta < 0.9$	$0.9 < \eta < 1.2$	$1.2 < \eta < 2.1$	$2.1 < \eta < 2.4$
$0.0 < \eta < 0.9$	0.938 ± 0.011	0.880 ± 0.014	0.864 ± 0.012	0.880 ± 0.021
$0.9 < \eta < 1.2$	0.880 ± 0.014	0.836 ± 0.021	0.824 ± 0.017	0.819 ± 0.047
$1.2 < \eta < 2.1$	0.864 ± 0.012	0.824 ± 0.017	0.813 ± 0.010	0.804 ± 0.021
$2.1 < \eta < 2.4$	0.880 ± 0.021	0.819 ± 0.047	0.804 ± 0.021	0.784 ± 0.063

for the signal, given that the background normalization is constrained to the data in the m_{jj} sideband region.

We have performed the same study for electrons. The overall trigger efficiencies calculated from data and from the trigger simulation, averaged over p_T and η , agree within 1%.

Table B.4

Muon trigger efficiencies from trigger simulation for the Z+jets simulated samples.

muon η	Z+jets			
	$0 - 0.9$	$0.9 - 1.2$	$1.2 - 2.1$	$2.1 - 2.4$
$0 - 0.9$	0.97	0.94	0.93	0.92
$0.9 - 1.2$	0.94	0.91	0.91	0.89
$1.2 - 2.1$	0.93	0.91	0.90	0.88
$2.1 - 2.4$	0.92	0.88	0.88	0.85

Table B.5

Muon trigger efficiencies from trigger simulation for the Higss (300 GeV) simulated samples.

muon η	Higgs signal, 300 GeV			
	0 – 0.9	0.9 – 1.2	1.2 – 2.1	2.1 – 2.4
0 – 0.9	0.97	0.94	0.94	0.93
0.9 – 1.2	0.94	0.91	0.90	0.91
1.2 – 2.1	0.93	0.91	0.91	0.88
2.1 – 2.4	0.90	0.89	0.88	0.97

C. Lepton identification requirements and efficiencies

The standard tag-&-probe method used to evaluate the lepton identification efficiencies from data requires the reconstruction of the dilepton system with invariant mass in the range [60-120] GeV. One of the leptons, called tag, is required to pass full selection criteria and to match the tighter leg of the trigger. The other lepton candidate, (the probe) is selected with criteria that depends on the efficiency being measured. The sample is divided into two exclusive subsamples depending on whether the probe lepton passes or fails the selection criteria currently under investigation. Due to the presence of background events, the signal yields are obtained with a fit to the invariant mass distribution of the dilepton system. The measured efficiency is calculated as a function of p_T and η of the probe lepton from the relative yields of the signal in subsamples with passing or failing probes. Finally, the data to Monte Carlo scale factors are deduced by dividing the efficiencies in data by the ones obtained from Monte Carlo using exactly the same procedure. Scale factors are used instead of raw efficiencies in order to benefit from partial cancellations of systematic uncertainties associated with the procedure. The total efficiency measurement is factorized into five sequential relative efficiency measurements: tracking, reconstruction, identification, isolation and the total trigger efficiency. This can be expressed as following product:

$$\epsilon_{lepton} = \epsilon_{tracking} \times \epsilon_{RECO/Tracking} \times \epsilon_{ID/RECO} \times \epsilon_{ISO/ID} \times \epsilon_{Trigger/ISO}$$

Lepton identification requirements are given in Table C.1 for electrons, and in Table C.2 for muons. The data to simulation scale factors for these electron and muon identification requirements are listed in Table C.3.

Table C.1
Electron ID requirements for the Loose ID working point.

Variable	Barrel cut	Endcap cut
$\Delta\eta_{trk,supercluster}$	< 0.007	< 0.009
$\Delta\phi_{trk,supercluster}$	< 0.15	< 0.1
$\sigma_{i\eta,i\eta}$	< 0.01	< 0.03
H/E	< 0.12	< 0.10
d_0 (wrt primary vertex)	< 0.2 mm	< 0.2 mm
d_z (wrt primary vertex)	< 2 mm	< 2 mm
$ 1/E - 1/p $	< 0.05	< 0.05
$I_{PF, corr}/p_T$	< 0.15	< 0.15
Missing hits	≤ 1	≤ 1
Conversion vertex fit prob.	$< 10^{-6}$	$< 10^{-6}$

Table C.2
Muon ID requirements for the Tight ID working point.

Variable	Cut
isGlobalMuon	True
isPFMuon	True
$\chi^2/ndof$ (global fit)	< 10
Muon chamber hits in global fit	> 0
Muon stations with muon segments	> 1
d_{xy} (from tracker, wrt primary vertex)	< 2 mm
d_z (from tracker, wrt primary vertex)	< 5 mm
Valid pixel hits (tracker track)	> 0
Tracker layers with hits	> 5
$I_{PF, corr}/p_T$	< 0.12

Table C.3

Data to simulation scale factors for electron (upper) and muon (lower) identification requirements in various η ranges.

electron p_T	$0.0 < \eta < 0.8$	$0.8 < \eta < 1.442$	$1.556 < \eta < 2.0$	$2.0 < \eta < 2.5$
20 - 30	1.005 ± 0.003	0.981 ± 0.003	0.980 ± 0.005	1.017 ± 0.006
30 - 40	1.004 ± 0.001	0.991 ± 0.001	0.992 ± 0.002	1.019 ± 0.003
40 - 50	1.008 ± 0.001	0.994 ± 0.001	1.004 ± 0.002	1.005 ± 0.001
50 - 200	1.008 ± 0.001	0.999 ± 0.001	1.006 ± 0.003	1.009 ± 0.002

muon p_T	$0.0 < \eta < 0.8$	$0.8 < \eta < 2.1$	$2.1 < \eta < 2.4$
20 - 40	1.0043 ± 0.0004	1.0074 ± 0.0005	1.022 ± 0.001
40 - 100	1.0012 ± 0.0004	1.0043 ± 0.0004	1.014 ± 0.001

D. Systematic uncertainties on the signal

The systematic uncertainties on the signal are listed in Tables D.1 (muon channel) and D.2 (electron channel), for various m_H values, for the three btag categories.

Table D.1
Systematic uncertainty on the signal in the muon channel.

m_H (GeV)	0-btag		1-btag		2-btag	
	$1\sigma_{UP}$ (%)	$1\sigma_{DOWN}$ (%)	$1\sigma_{UP}$ (%)	$1\sigma_{DOWN}$ (%)	$1\sigma_{UP}$ (%)	$1\sigma_{DOWN}$ (%)
200	-3.2	1.5	5.8	-1.3	4.0	-6.7
210	-3.4	1.2	4.8	-1.9	8.5	-2.5
220	-3.1	1.7	4.5	-1.7	6.8	-6.1
230	-3.4	1.8	4.8	-2.1	7.4	-5.3
250	-2.9	2.1	3.8	-2.4	6.3	-5.5
275	-3.4	1.5	4.5	-1.0	6.1	-5.5
300	-3.6	1.4	4.6	-0.69	6.8	-5.7
350	-3.8	1.7	4.7	-0.84	6.7	-6.1
375	-3.7	1.7	5.0	-0.31	5.2	-7.5
400	-3.9	1.6	4.5	-0.74	6.8	-5.7
425	-4.1	1.6	5.1	-0.59	5.9	-5.8
450	-4.1	1.8	4.0	-1.1	8.1	-5.0
475	-3.9	1.8	4.1	-0.6	7.0	-6.5
500	-3.6	2.1	3.6	-0.97	7.1	-6.7
525	-4.1	2.0	4.8	-0.65	6.4	-7.1
550	-3.6	1.9	3.5	-0.87	6.9	-5.6
575	-4.4	1.8	4.9	-0.78	6.7	-5.7
600	-4.3	1.9	4.4	-1.3	7.8	-4.9

Table D.2
Systematic uncertainty on the signal in the electron channel.

m_H (GeV)	0-btag		1-btag		2-btag	
	$1\sigma_{UP}$ (%)	$1\sigma_{DOWN}$ (%)	$1\sigma_{UP}$ (%)	$1\sigma_{DOWN}$ (%)	$1\sigma_{UP}$ (%)	$1\sigma_{DOWN}$ (%)
200	-3.4	1.8	3.9	-3.7	12	-0.18
210	-3.5	1.2	5.4	-1.1	6.9	-5.5
220	-2.9	1.9	4.1	-2.0	7.0	-7.2
230	-3.6	1.4	4.9	-1.9	8.7	-3.5
250	-2.9	2.2	4.0	-2.4	5.1	-6.2
275	-3.5	1.5	4.7	-1.3	6.3	-4.6
300	-3.9	1.5	5.9	-0.26	5.9	-7.7
350	-3.9	1.5	4.7	-0.41	7.1	-6.5
375	-3.9	1.8	4.5	-1.1	7.5	-5.7
400	-3.9	1.9	4.0	-1.1	8.2	-6.0
425	-4.0	1.8	4.8	-0.67	6.9	-6.6
450	-3.9	1.5	3.8	-0.43	7.8	-5.3
475	-4.3	1.8	5.2	-0.54	6.1	-6.2
500	-4.1	2.0	5.2	-0.83	5.8	-6.7
525	-4.0	2.0	3.8	-1.3	8.1	-5.5
550	-4.0	1.8	4.5	-1.1	6.2	-5.1
575	-4.0	1.9	4.1	-0.67	7.1	-6.2
600	-4.4	1.8	5.2	-0.68	6.7	-6.1

E. Expected signal and background events per btag category

Tables E.1, E.2, and E.3 list the numbers of signal and background events expected for 19.6 fb^{-1} in the mass range $[m_H - 6\%, m_H + 10\%]$ in the three btag categories, separately for the $\mu^+\mu^-jj$ and e^+e^-jj channels (denoted $\mu\mu$ and ee , respectively).

Table E.1
Expected yields in the 0-btag category.

m_H (GeV)	signal		Z+jets		e μ data		diboson		total background	
	$\mu\mu$	ee	$\mu\mu$	ee	$\mu\mu$	ee	$\mu\mu$	ee	$\mu\mu$	ee
250	90.0	80.4	6160.5	5312.2	24	19	201.7	175.6	6386.3	5506.7
300	90.0	80.6	3334.3	2800.3	11	9	121.1	106.6	3466.6	2915.7
400	82.6	73.5	1254.4	1065.9	1	0	55.9	49.3	1310.9	1115.6
500	33.4	30.2	429.0	381.9	1	1	23.9	20.4	454.0	403.2
600	11.9	10.5	179.3	152.3	0	0	11.3	10.8	190.6	163.2

Table E.2
Expected yields in the 1-btag category.

m_H (GeV)	signal		Z+jets		e μ data		diboson		total background	
	$\mu\mu$	ee	$\mu\mu$	ee	$\mu\mu$	ee	$\mu\mu$	ee	$\mu\mu$	ee
250	44.7	40.1	2124.7	1779.0	87	68	89.7	74.2	2301.2	1921.4
300	46.8	40.8	1174.5	987.0	33.0	25	60.8	49.1	1268.3	1062.1
400	45.0	40.8	459.8	406.7	6	5	26.9	24.1	492.9	435.7
500	18.9	17.0	181.1	155.8	1	0	13.9	10.1	195.5	166.3
600	7.0	6.4	80.9	61.4	0	0	6.5	5.5	87.4	66.9

Table E.3
Expected yields in the 2-btag category.

m_H (GeV)	signal		Z+jets		e μ data		diboson		total background	
	$\mu\mu$	ee	$\mu\mu$	ee	$\mu\mu$	ee	$\mu\mu$	ee	$\mu\mu$	ee
250	15.6	14.8	180.9	138.6	42	33	18.7	16.4	241.7	188.0
300	18.5	16.0	91.2	70.9	28	22	12.2	11.7	131.4	104.6
400	19.8	16.8	32.2	24.6	1	0	7.0	5.3	39.7	30.4
500	8.2	7.5	9.6	8.9	0	0	2.7	2.5	12.3	11.4
600	3.0	2.8	5.6	4.5	0	0	1.7	1.5	7.3	6.0

F. Determination of $t\bar{t}$ background from data

In the analysis, the $t\bar{t}$ background is estimated from data. Additional plots supporting the robustness of the procedure are presented below. The comparison of $e^\pm\mu^\mp$ and $(e^+e^- + \mu^+\mu^-)$ distributions using Powheg + Pythia top MC shows an excellent agreement, as depicted in Figure F.1 for several variables after different steps of the selection. A similar agreement is observed in Figure F.2, which compares the 2012 $e^\pm\mu^\mp$ data to Powheg + Pythia top MC. Figure F.3 displays the MET significance distribution for dilepton data compared to the sum of Drell-Yan Monte Carlo plus $e^\pm\mu^\mp$ data for events with two b-tags (1 JPM + 1 JPL), and the dijet invariant mass (right) for $e^+e^- + \mu^+\mu^-$ and $e^\pm\mu^\mp$ data for events outside the leptonic Z mass window, show again very good agreement.

Next, the data-driven evaluation of the $t\bar{t}$ background is compared to an alternative method based on top simulation only. Figure F.4 compares the previous $e^\pm\mu^\mp$ data distributions to the prediction of Powheg + Pythia top MC normalized to the NLO $t\bar{t}$ cross-section. The gray area represents the systematic error (including luminosity, lepton trigger and ID efficiencies, b-tagging efficiency, mistag efficiency, and pile-up uncertainties; no contribution from normalization) of the MC prediction. With the 19.6 fb^{-1} , the statistical errors of the $e^\pm\mu^\mp$ data points compare well to the size of the gray boxes. In addition, the $t\bar{t}$ MC underestimates the normalization of the $e^\pm\mu^\mp$ data by 20% before b-tagging (12% for events with 2 b-tagged jets). Based on this comparison, we chose to use the data-driven estimation.

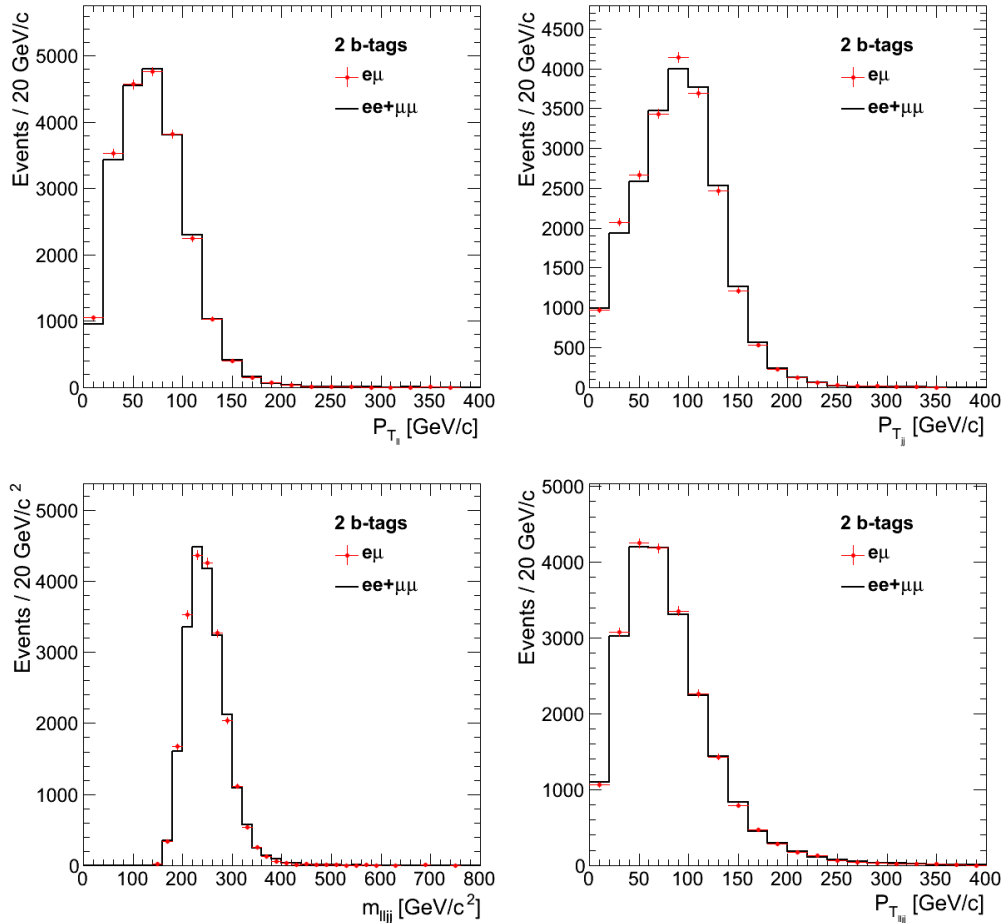


Figure F.1. Powheg + Pythia top MC $e^\pm\mu^\mp$ to $(e^+e^- + \mu^+\mu^-)$ comparison for several variables after different steps of the selection, as specified in the legends. Top: dilepton (left) and dijet transverse momentum (right). Bottom: dilepton + dijet “Higgs” invariant mass (left) and transverse momentum (right).

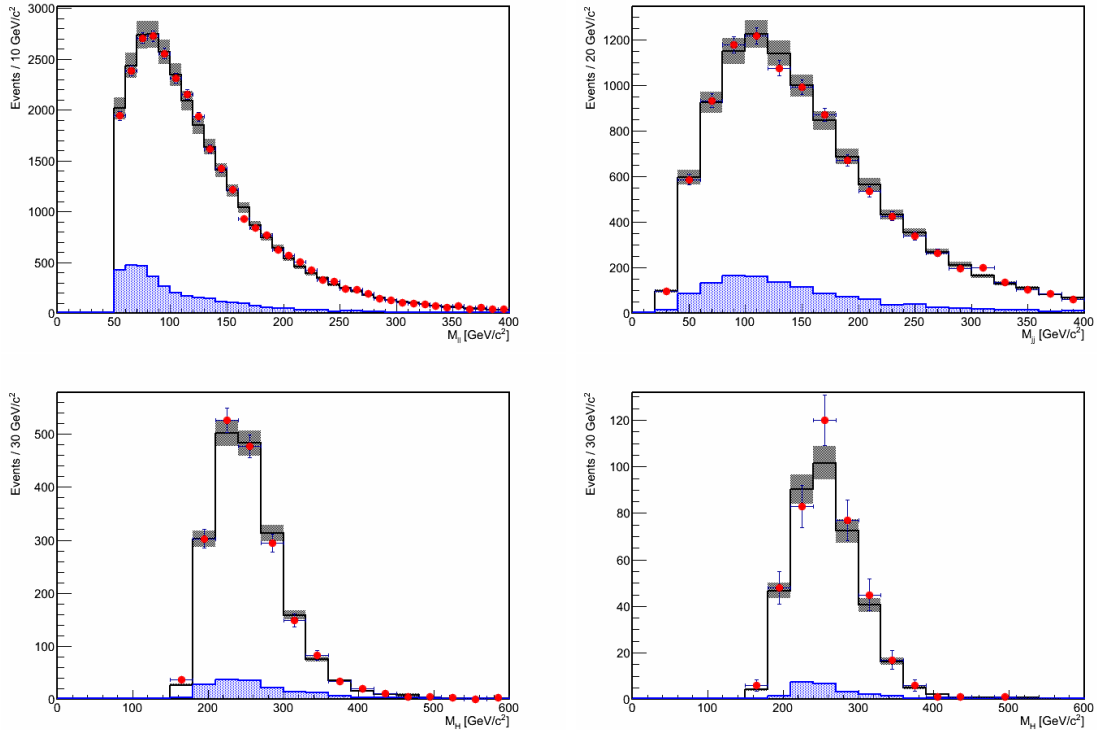


Figure F.2. Comparison of 2012 $e^\pm\mu^\mp$ data to Powheg + Pythia top MC, corresponding to an integrated luminosity of 19.6 fb^{-1} . Red dots are $e^\pm\mu^\mp$ data; white histogram top Monte Carlo; blue histogram other small backgrounds. Top: dilepton invariant mass (left) and dijet invariant mass (right). Bottom: “Higgs” invariant mass for events with 1 JPL b-tag (left), and two (1 JPM + 1 JPL) b-tags and MET significance < 10 (right).

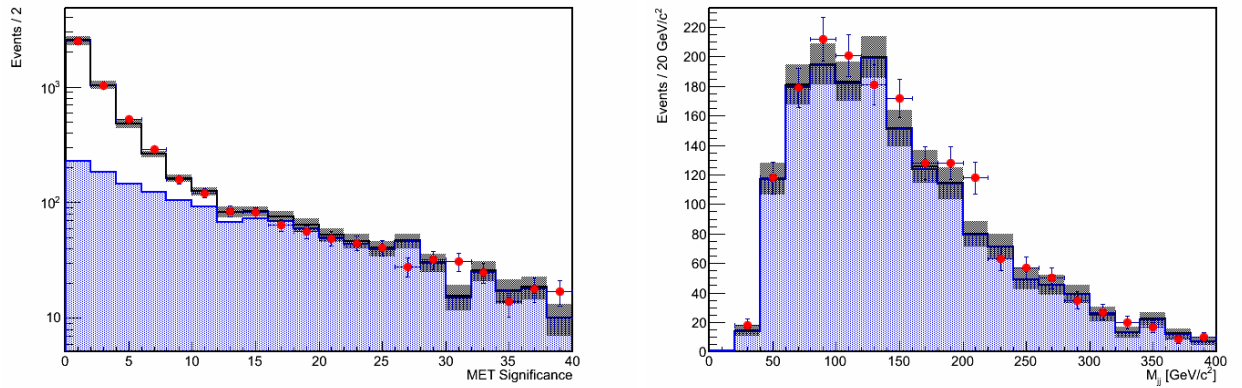


Figure F.3. MET significance distribution for dilepton data compared to the sum of Drell-Yan Monte Carlo plus $e^\pm\mu^\mp$ data for events with two btags (left). Dijet invariant mass (right) for $e^+e^- + \mu^+\mu^-$ and $e^\pm\mu^\mp$ data for events outside the leptonic Z mass window, with two b-tags, and MET significance > 8 . Other cuts are detailed in the text. Red dots are $e^+e^- + \mu^+\mu^-$ data; white histogram Drell Yan Monte Carlo; blue histogram $e^\pm\mu^\mp$ data (plus other small backgrounds).

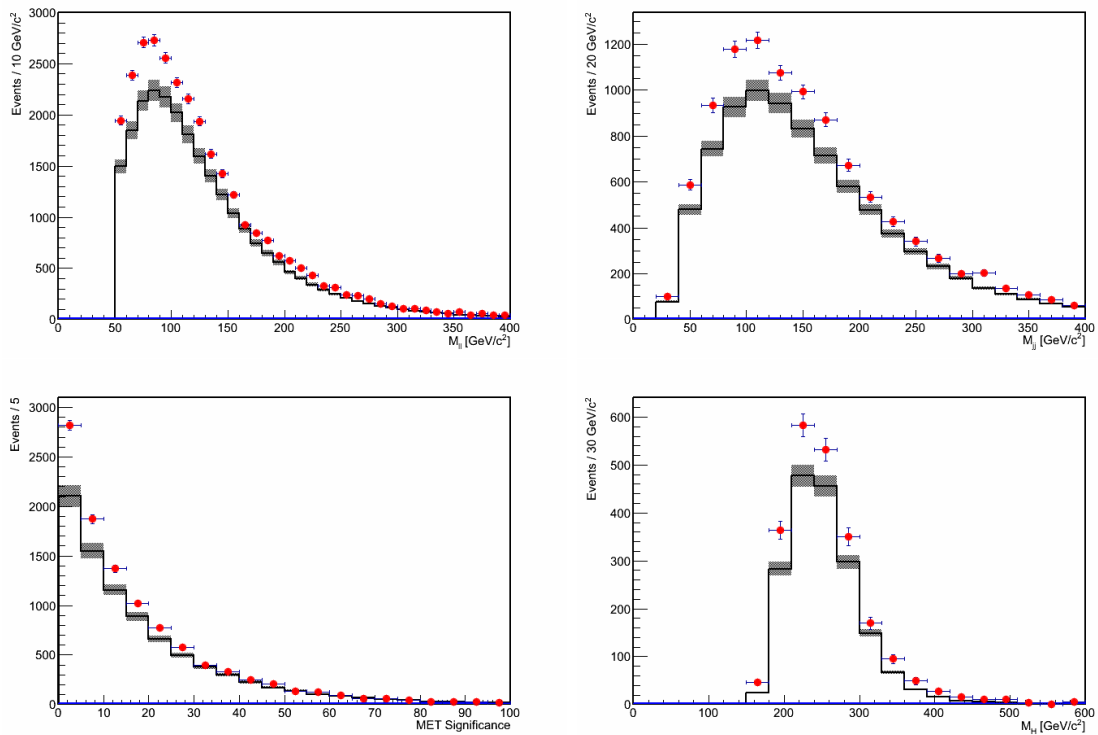


Figure F.4. Comparison of 2012 $e^\pm\mu^\mp$ data to Powheg + Pythia top MC normalized to the $t\bar{t}$ NLO cross-section. Red dots are $e^\pm\mu^\mp$ data; white histogram top Monte Carlo. Top: dilepton invariant mass (left) and dijet invariant mass (right). Bottom: MET significance (left), and “Higgs” invariant mass (right).

G. Mass distributions for the electron and muon channels

The m_{lljj} (m_{ZZ}) distributions, depicted in Figure G.1 for the electron and muon channels, display an excellent agreement both in the m_{jj} sideband and signal regions.

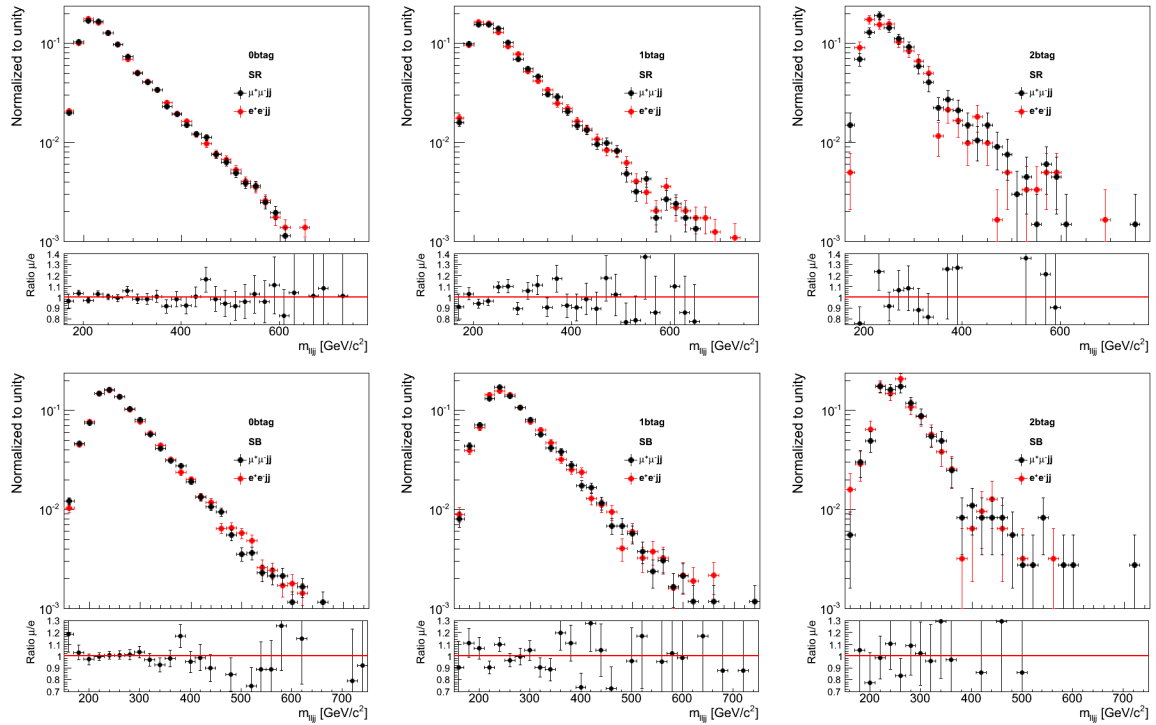


Figure G.1. Mass distributions of the $\ell^+\ell^-jj$ system for events in the electron and muon channels: data in the m_{jj} (top) signal and (bottom) sideband regions. From left to right, plots correspond to the 0-, 1-, and 2-btag categories.

In order to minimize systematic uncertainties from Monte Carlo predictions, we normalize background to sidebands. For completeness, the signal region is $71 < m_{jj} < 111$ GeV and the sideband region is $60 < m_{jj} < 71$ GeV plus $111 < m_{jj} < 130$ GeV. The procedure is applied independently in each b-tag category since background

composition varies between categories. The dominant backgrounds include Z+jets with either light or heavy flavor jets, and top background. These backgrounds equally populate the m_{jj} signal region and m_{jj} sidebands [92]. If we were to rely on Monte Carlo prediction of background, uncertainties in the b-tag efficiency alone would result in about 20% uncertainty in the 2 b-tag category. We observe good agreement of the m_{jj} distributions in the three b-tag categories and in different m_{ZZ} mass ranges for the range $60 < m_{jj} < 130$ GeV. A more detailed look at the sidebands can be seen in Section 6.2.3.

We can use parameterization of the m_{ZZ} mass spectrum in the background Monte Carlo in the m_{jj} signal region and m_{jj} sideband. We create a ratio $\alpha(m_{ZZ})$ between the two, which predicts how sideband data can be scaled to obtain background prediction in the signal region. Then background expectation $N_{bkg}(m_{ZZ})$ is obtained from the distribution of events in the sideband $N_{sb}(m_{ZZ})$ as shown in equation G.1.

$$N_{bkg}(m_{ZZ}) = N_{sb}(m_{ZZ}) \times \frac{N_{bkg}^{MC}(m_{ZZ})}{N_{sb}^{MC}(m_{ZZ})} = N_{sb}(m_{ZZ}) \times \alpha(m_{ZZ}) \quad (\text{G.1})$$

The advantage of the above approach is that most systematic uncertainties cancel in the ratios. The remaining factor, $\alpha(m_{ZZ})$, reflects small kinematic differences between the signal region and sideband. This procedure also provides automatic normalization of background and makes any needed adjustments to the shape of the m_{ZZ} mass spectrum. Even though we use these corrections there is very good agreement between data and Monte Carlo prediction of the m_{ZZ} and m_{jj} distributions after the preselection requirements [75].

To estimate the shape of background in data, the events in the sideband region have been scaled according to $\alpha(m_{ZZ})$. These distributions are then fit using a parameterization derived from Monte Carlo. The fit function is a Crystal-Ball function multiplied by the Fermi-function [78] [93]. The Fermi-function helps to describe the sharp kinematic turn-on at low mass, but otherwise this is a purely empirical fit. Only the width of the Gaussian core of the Crystal-Ball and the turn-over point to

the power-law are free parameters in the fit. The other parameters are fixed to values extracted from the simulation [92].

H. Limit Cross Checks

Another approach, referred to as *cut-and-count* analysis, uses only the number of events selected with a reconstructed Higgs mass in the window $[m_H - 6\%, m_H + 10\%]$. The Higgs cross section limit is determined from the expected number of signal and background events passing the selections s and b respectively. The results shown in Figure H.1 are compatible with the full results.

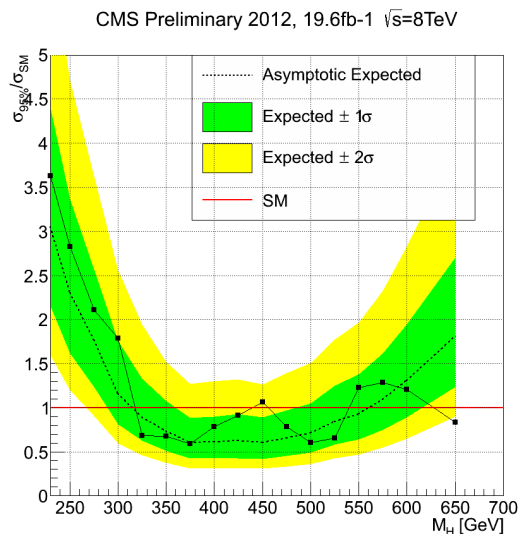


Figure H.1. Observed (solid) and expected (dashed) 95% CL upper limit on the ratio of the production cross section to the SM expectation for the Higgs boson obtained using the *cut-and-count* technique, which integrates the mass distributions in a range $[m_H - 6\%, m_H + 10\%]$ around each Higgs mass hypothesis. The 68% and 95% ranges of expectation for the background-only model are also shown with green and yellow bands, respectively. The solid line at 1 indicates the expectation for a SM-Higgs-like boson.

I. 3D Prototype Silicon Sensors

The silicon pixels of the LHC are exposed to large amounts of radiation. The next phase of the LHC (called High Luminosity LHC) will see an order of magnitude higher in the luminosity corresponding to approximately $10^{35} \text{ cm}^{-2} \text{ s}^{-1}$ [94]. This luminosity means that the inner tracker will receive a radiation fluence of around $10^{16} n_{eq}/\text{cm}^2$. This is problematic since the current planar silicon detectors only function with a max fluence of approximately $10^{15} n_{eq}/\text{cm}^2$. 3D silicon detectors are one of the ways that may provide the necessary radiation tolerance for the next phase of the LHC.

I.1 3D Sensors

Silicon detectors are typically fabricated with planer structures on the material surfaces. The voltages needed to deplete the detector bulk are typically on the order of tens of volts. The drift paths are also comparable to the thickness of the bulk [95]. In a 3D detector there are vertical cylindrical electrodes that go through the entire wafer thickness. An example diagram of the processes in a planer and 3D detector is shown in Figure I.1 [96]. The main reason that 3D detectors have better radiation hardness compared to planer detectors is that there is a much shorter distance between the electrodes. This is also independent of the thickness of the substrate.

There are a variety of different configurations that 3D sensors can use [95]. The configurations that have been fabricated and are used in the following tests can be seen in Figure I.2. The fabrication was done by SINTEF and one sensor has four readout columns (4E) and the other has 2 (2E) for each CMS pixel that is sized $100 \mu\text{m}$ by $150 \mu\text{m}$. The distances between each center of the readouts is $62.5 \mu\text{m}$ for the 2E and $45 \mu\text{m}$ for the 4E sensors [97].

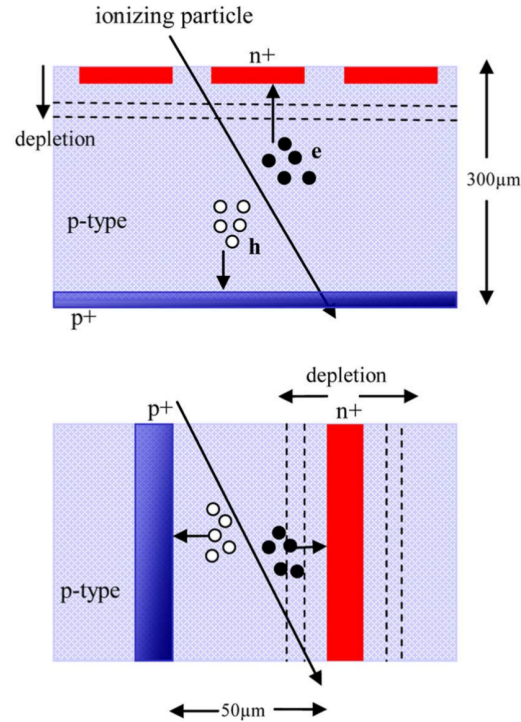


Figure I.1. Operations of planar and 3D detectors are depicted. [96]

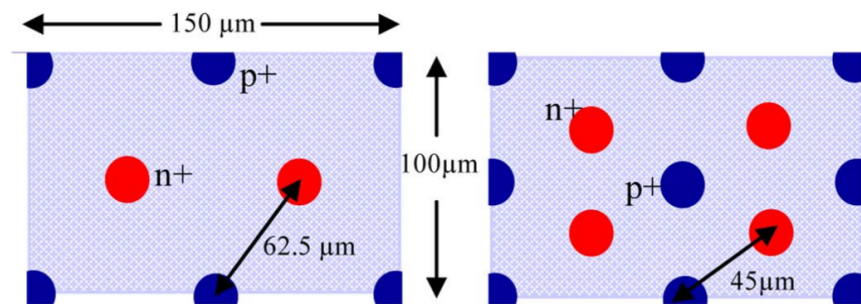


Figure I.2. Sketch of arrangement of columnar electrodes in CMS pixel sensors of 2E type (left) and 4E type (right). [96]

The fabricated sensors are tested both on the wafer and also after they have been connected to a 40 MHz CMS pixel readout chip (ROC) through bump-bonds. Each

ROC has 4160 pixels that are organized in a matrix of 52 columns by 80 rows. The characterization of the I-V properties of the 3D pixel sensors can be seen in Figure I.3. After the wire bonding, the leakage current drops off for all the sensors tested. This is because when the sensors were tested on the wafers, only a temporary metal layer was used to connect the columns. This allowed the entire chip to be tested at once, but led to extra leakage current as can be seen in Figure I.3.

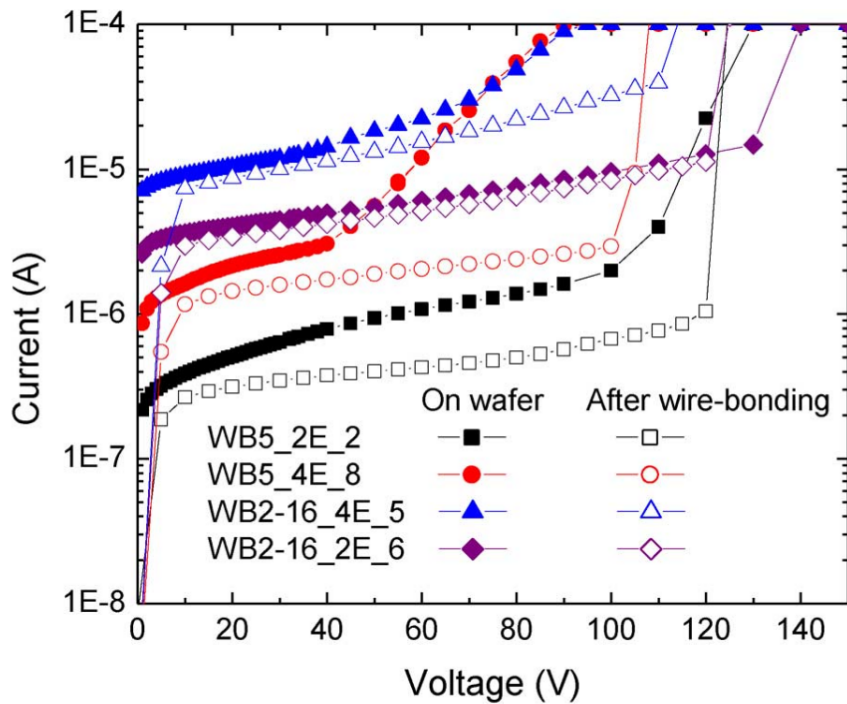


Figure I.3. I-V characteristics of four 3D CMS pixel sensors with different combinations of substrate thickness and electrode configuration as measured at wafer level and after wire-bonding. The convention used in naming is wafer_electrode_configuration_sensor number. [96]

I.2 Threshold and Noise Measurements

A scan of the threshold of every pixel is done by injecting an internal charge (VCAL) and then looking at the response versus how much charge was deposited. One

VCAL unit corresponds to 65.5 electrons. The ideal curve would be a step function from 0 to 1. But because some of the injected charge below the threshold is not detected, and some of it above the threshold is detected there is a noise component. This noise is the width of the curve. The efficiency curve is called an S-curve. This corresponds to the convolution of the ideal step function and the Gaussian pixel noise distribution.

The threshold is the value of charge that corresponds to an efficiency of 0.5 in the S-curve. The equivalent noise charge (ENC) of the pixel is given below.

$$ENC = \frac{1}{\sqrt{2\pi}} \frac{1}{s} \quad (I.1)$$

In this equation, s is the slope of the S-curve at an efficiency of 0.5. The distribution of both the noise and thresholds of the individual pixels make up a Gaussian distribution, which in turn give the threshold and noise of the entire chip. Figure I.4 shows the efficiency versus VCAL curves for two pixels, one on the edge and one in the center. Similarly Figure I.5 shows the map of the noise for each pixel in the rows and columns as they are laid out on the entire sensor. Also shown is the Gaussian fit for the noise on these pixels.

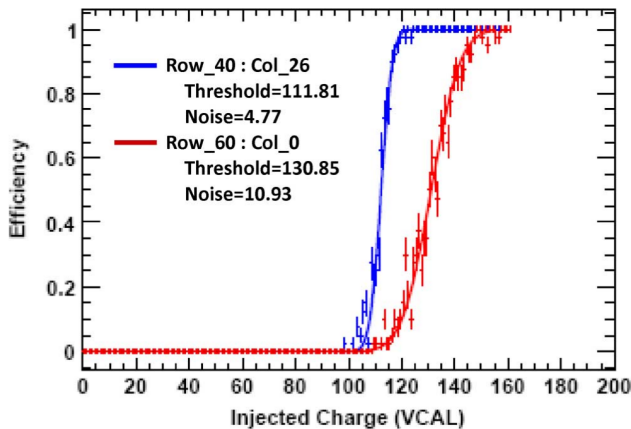


Figure I.4. S-curves of an edge pixel and a regular pixel in the sensor WB5_2E_2 at a reverse bias of 40 V. The threshold and noise values are in VCAL units. [96]

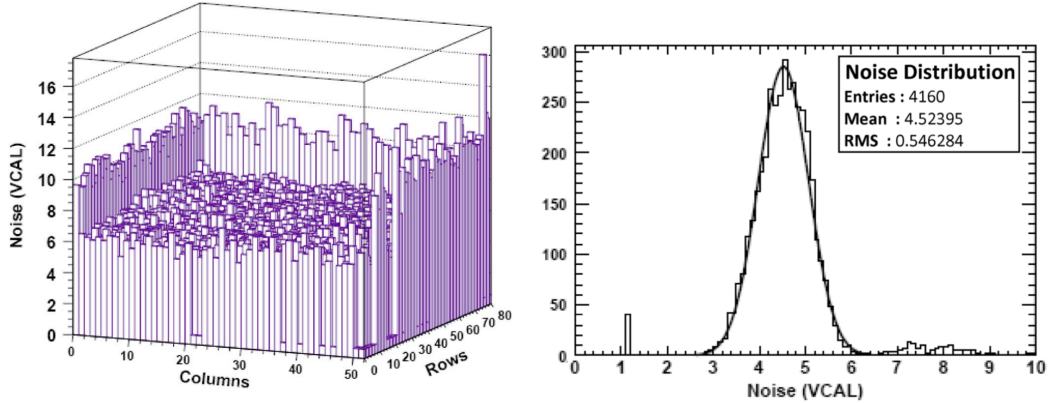


Figure I.5. Noise map of the WB5_2E_2 chip at a reverse bias of 40 V (left). Gaussian noise distribution of the WB5_2E_2 chip at a reverse bias of 40 V (right). [96]

In addition to measuring the noise performance at just one bias voltage, this has also been done for a range of voltages. This can be seen in Figure I.6. We see that the noise decreases for bias voltages up to 40 V, but beyond this the noise is essentially constant. We also get that the minimum noise for the 2E sensors is approximately 300 electrons and around 450 electrons for the 4E sensors. The 4E sensors have a higher noise compared with the 2E sensors because there is a smaller separation between the electrodes. This smaller separation is also why both of the 3D detector configurations have higher noise than planer pixel detectors.

For the threshold, there is a trimming algorithm that is done to correct variations between pixels and to unify the individual pixel thresholds to the lowest value [96]. This is needed to improve the position resolution of the detector. Figure I.7 shows both the normal threshold measurements and the same measurements using trimming.

For the WB2-16_2E_6 module with reverse bias voltage of 40 V, the threshold is 7919 ± 362 electrons before trimming and 6832 ± 86 electrons after trimming. The other modules have similar performance. Compared with the FPIX detector (and BPIX) which has a threshold of 2870 ± 220 electrons (2940 ± 80), the 3D detector display higher thresholds [98].

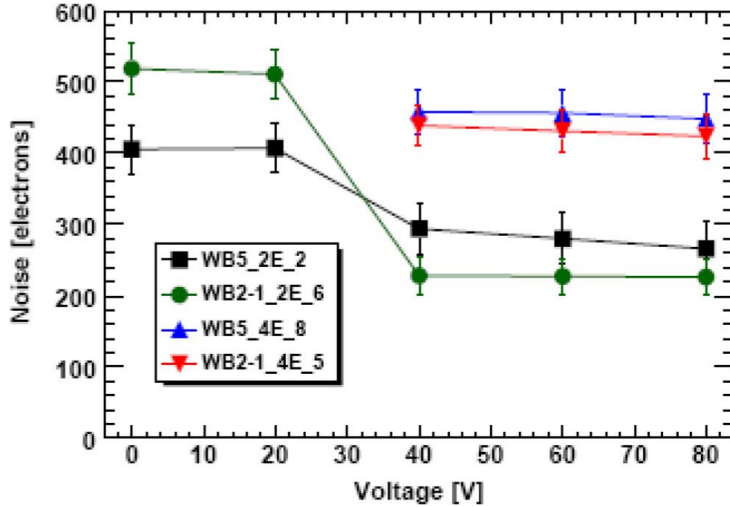


Figure I.6. Noise as a function of reverse bias voltage for the four sensors featuring different substrate thickness and electrode configuration. [96]

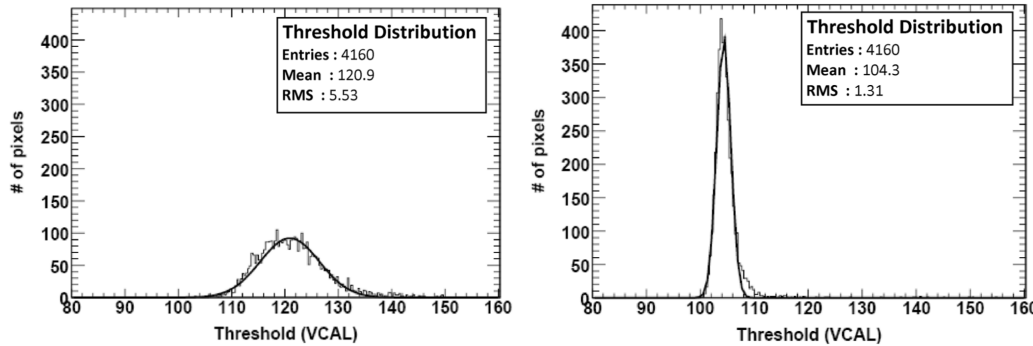


Figure I.7. Threshold distribution of the WB2-16_2E_6 chip at a reverse bias of 40 V before trimming (right) and after trimming (left). [96]

Since these studies have been performed, there have been a number of improvements particularly in fabrication of the 3D sensors and the ability to fabricate them without any support structure. With additional improvements that have also been

made in the trimming algorithms, 3D pixel detectors are proving to be very promising for the future pixel upgrade to the High Luminosity LHC.

LIST OF REFERENCES

LIST OF REFERENCES

- [1] David J. Griffiths. *Introduction to Quantum Mechanics (2nd ed.)*. Prentice Hall, ISBN 0-13-805326-X, 2004.
- [2] J. Christman. The Weak Interaction. *Physnet, Michigan State University*, 2001.
- [3] S.L. Glashow. Partial Symmetries of Weak Interactions. *Nucl.Phys.*, 22:579–588, 1961.
- [4] D.V.Schroeder M.E.Peskin. *An Introduction To Quantum Field Theory*. Westview Press, 1995.
- [5] G. 't Hooft. Renormalizable lagrangians for massive Yang-Mills fields. *Nucl. Phys.*, B35:167, 1971.
- [6] M.Veltman G. 't Hooft. Regularization and renormalization of gauge fields. *Nucl. Phys.*, B44:189, 1972.
- [7] Ringo Doe. Gauge theory, 2013.
- [8] S. Dawson. Introduction to electroweak symmetry breaking. *arXiv:9901280*, 1998.
- [9] Luis lvarez Gaum and John Ellis. Eyes on a prize particle. *Nature Physics*, 7:2–3, 2011.
- [10] F. Englert and R. Brout. Broken Symmetry and the Mass of Guage Vector Mesons. *Phys.Rev.Lett.*, pages 13:321–322, 1964.
- [11] G. Ridolfi. Search for the Higgs boson: theoretical perspectives. *arXiv:hep-ph/0106300*, 2001.
- [12] ALEPH Collaboration, CDF Collaboration, D0 Collaboration, DELPHI Collaboration, L3 Collaboration, OPAL Collaboration, SLD Collaboration, LEP Electroweak Working Group, Tevatron Electroweak Working Group, SLD Electroweak and Heavy Flavour Groups. Precision Electroweak Measurements and Constraints on the Standard Model. 2010. 18 pages.
- [13] R. Barate et al. Search for the standard model Higgs boson at LEP. *Phys.Lett.*, B565:61–75, 2003.
- [14] Combined CDF and D0 Upper Limits on Standard Model Higgs Boson Production with up to 8.6 fb^{-1} of Data. 2011.
- [15] Henning Flacher, Martin Goebel, Johannes Haller, Andreas Hocker, Klaus Monig, et al. Revisiting the Global Electroweak Fit of the Standard Model and Beyond with Gfitter. *Eur.Phys.J.*, C60:543–583, 2009.

- [16] Lyndon Evans and Philip Bryant. Lhc machine. *Journal of Instrumentation*, 3(08):S08001, 2008.
- [17] Ulrik Egede. Higgs production, Aug 2013.
- [18] LHC Higgs Cross Section Working Group. Lhc higgs cross section wg picture gallery, Aug 2013.
- [19] J. Beringer et al. (Particle Data Group). 2012 Review of Particle Physics. *Phys. Rev. D*, 86, 2012.
- [20] CMS Computing Production. <http://cmsdoc.cern.ch/cms/production/www/html/general/>, 2014.
- [21] John M. Campbell, J.W. Huston, and W.J. Stirling. Hard Interactions of Quarks and Gluons: A Primer for LHC Physics. *Rept.Prog.Phys.*, 70:89, 2007.
- [22] CERN 2004-003. *LHC Design Report*. 2004.
- [23] Cern accelerator complex, May 2011.
- [24] ATLAS Collaboration. The ATLAS Experiment at the CERN Large Hadron Collider. *Journal of Instrumentation*, 3:S08003, 2008.
- [25] ALICE Collaboration. The ALICE Experiment at the CERN LHC. *Journal of Instrumentation*, 3:S08002, 2008.
- [26] LHCb Collaboration. The LHCb Detector at the LHC. *Journal of Instrumentation*, 3:S08005, 2008.
- [27] Atlas. <http://www-zeus.physik.uni-bonn.de/atlas.php?lang=en>, 2013.
- [28] Cms. http://www.gridpp.ac.uk/pics/stand2004/cms_2.jpg, 2013.
- [29] Lhc. <http://science.portalhispanos.com/wordpress/2011/08/30/lhcb-mide-de-forma-precisa-la-oscilacion-materia-antimateria-de-los-mesones-b/>, 2013.
- [30] Alice. <http://cerncourier.com/cws/article/cern/35879>, 2013.
- [31] LHC. Lhc programme coordination. <http://lpc.web.cern.ch/lpc/>, 10 2013.
- [32] G L Bayatian. *CMS Physics: Technical Design Report*. Technical Design Report CMS. CERN, Geneva, 2006.
- [33] The CMS Collaboration. The CMS experiment at the CERN LHC. *Journal of Instrumentation*, 3:S08004, 2008.
- [34] CMS. Cms luminosity public results. <https://twiki.cern.ch/twiki/bin/view/CMSPublic/LumiP10> 2013.
- [35] Francesco Pandolfi. Search for a standard model higgs boson in the decay channel h to zz to llqq at the cms experiment, 06 2011. Slides of a talk given at Seminario sul Progetto di Tesi, 11.06.10.
- [36] CMS Collaboration. The Magnet Project: Technical Design Report. *CERN/LHCC*, 97:10, 1997.

- [37] Newsline. Cms solenoid magnet, 05 2011.
- [38] CMS Collaboration. The Tracker Project: Technical Design Report. *CERN/LHCC*, 98:10, 1998.
- [39] D. Sprenger, M. Weber, R. Adolphi, R. Brauer, L. Feld, K. Klein, A. Ostapchuk, S. Schael, and B. Wittmer. Validation of Kalman Filter alignment algorithm with cosmic-ray data using a CMS silicon strip tracker endcap. *Journal of Instrumentation*, 5:6007, June 2010.
- [40] CMS Collaboration. The Electromagnetic Calorimeter Project: Technical Design Report. *CERN/LHCC*, 97:33, 1997.
- [41] CMS Collaboration. The Hadron Calorimeter Project: Technical Design Report. *CERN/LHCC*, 97:31, 1997.
- [42] S Chatrchyan et al. Performance of CMS Hadron Calorimeter Timing and Synchronization using Test Beam, Cosmic Ray, and LHC Beam Data. *JINST*, 5:T03013, 2010.
- [43] et al. Bayatyan, G L. *CMS TriDAS project: Technical Design Report, Volume 1: The Trigger Systems*. Technical Design Report CMS. 2002.
- [44] Sergio Cittolin, Attila Rcz, and Paris Sphicas. *CMS The TriDAS Project: Technical Design Report, Volume 2: Data Acquisition and High-Level Trigger. CMS trigger and data-acquisition project*. Technical Design Report CMS. CERN, Geneva, 2002.
- [45] Emilio Meschi, T Monteiro, Christopher Seez, and Pratibha Vikas. Electron reconstruction in the cms electromagnetic calorimeter. Technical Report CMS-NOTE-2001-034, CERN, Geneva, Jun 2001.
- [46] Stephanie Baffioni, Claude Charlot, Federico Ferri, David Futyan, Paolo Meridiani, Ivica Puljak, Chiara Rovelli, Roberto Salerno, and Yves Sirois. Electron reconstruction in cms. Technical Report CMS-NOTE-2006-040, CERN, Geneva, Feb 2006.
- [47] et Al. Adam Wolfgang. Reconstruction of Electrons with the Gaussian-Sum Filter in the CMS Tracker at the LHC. *CMS-NOTE-2005-001*, 2005.
- [48] Francesco Pandolfi. Search for the Standard Model Higgs Boson in the H to ZZ to llqq Decay Channel at CMS, 2011.
- [49] Matteo Cacciari, Gavin P. Salam, and Gregory Soyez. The anti- k t jet clustering algorithm. *Journal of High Energy Physics*, 2008(04):063, 2008.
- [50] G. Corcella *et al.* Herwig 6.5 release note. 2013.
- [51] CMS Collaboration. Particle-flow event reconstruction in cms and performance for jets, taus, and met. *Technical Report CMS-PAS-PFT-09-001*, 2009.
- [52] Annapaola de Cosa. Search for a Higgs boson in the H to ZZ to llqq channel with the CMS experiment at the LHC, 2013.
- [53] S. de Visscher et al. J. Alwall, P. Demin. MadGraph/MadEvent v4: the new webgeneration. *JHEP*, 09:028, 2007.

- [54] P.Nason. A New Method for Combining NLO QCD with Shower Monte Carlo Algorithms. *JHEP*, 11:040, 2004.
- [55] Oleari S. Frixione, P. Nason. Matching NLO QCD Computations with Parton Shower Simulations: the POWHEG method. *JHEP*, 11:070, 2007.
- [56] C. Oleari et al. S. Alioli, P. Nason. NLO Vector-Boson Production Matched with Shower in POWHEG. *JHEP*, 07:06, 2008.
- [57] T. Sjöstrand, S. Mrennan and P. Z. Skands. PYTHIA 6.4 Physics and Manual. *JHEP*, 05:026, 2006.
- [58] LHC Higgs Cross Section Working Group, S. Dittmaier, C. Mariotti, G. Passarino, and R. Tanaka (Eds.). Handbook of LHC Higgs Cross Sections: 1. Inclusive Observables. *CERN-2011-002*, CERN, Geneva, 2011.
- [59] LHC Higgs Cross Section Working Group, S. Dittmaier, C. Mariotti, G. Passarino, and R. Tanaka (Eds.). Handbook of LHC Higgs Cross Sections: 2. Differential Distributions. *CERN-2012-002*, CERN, Geneva, 2012.
- [60] K. Nakamura et al. Review of particle physics. *J. Phys.*, G37:075021, 2010.
- [61] L. Borrello et al. "search for the standard model higgs boson in the decay channel $h \rightarrow zz \rightarrow 2l2b'$ ". CMS Analysis Note CMS-AN-2011-399, 2011.
- [62] Matteo Cacciari, Gavin P. Salam, and Gregory Soyez. The Anti-k(t) jet clustering algorithm. *JHEP*, 0804:063, 2008.
- [63] CMS Collaboration. Jet energy corrections determination at 7 tev. CMS Physics Analysis Summary CMS-PAS-JME-10-010, 2010.
- [64] FastJet Algorithm. <https://twiki.cern.ch/twiki/bin/view/CMSPublic/WorkBookJetEnergyCorr> 2014.
- [65] The CMS $H \rightarrow ZZ \rightarrow 2l2q$ Group. Search for the standard model Higgs Boson in the decay channel $H \rightarrow ZZ \rightarrow 2l2q$ at CMS. *CMS-AN-2012/115*, 2012.
- [66] b-Jet Identification in the CMS Experiment. Technical Report CMS-PAS-BTV-11-004, CERN, Geneva, 2012.
- [67] Search for a standard model like Higgs boson in the decay channel H to ZZ to l+l- q qbar at CMS. Technical Report CMS-PAS-HIG-12-024, CERN, Geneva, 2013.
- [68] A. et. Al De Rujula. Higgs boson look-alikes at the lhc. *Journal Name: Physical Review. D, Particles Fields*, Jul 2010.
- [69] Yanyan Gao, Andrei V. Gritsan, Zijin Guo, Kirill Melnikov, Markus Schulze, and Nhan V. Tran. Spin determination of single-produced resonances at hadron colliders. *Phys. Rev. D*, 81:075022, Apr 2010.
- [70] Y. Gao et al. Spin determination of single-produced resonances at hadron collider. *Phys. Rev.*, D81:075022, 2010.
- [71] A. De Rujula et al. Higgs look-alikes at the LHC. *Phys. Rev.*, D82:013003, 2010.

- [72] et al. A. Hoecher. TMVA - Toolkit for Multivariate Data Analysis. *arXiv:physics/0703039*, 2007.
- [73] G. Punzi. Sensitivity of searches for new signals and its optimization. In *proceedings to PhyStat 2003 Conference, Stanford, Ca, USA, September 2003, PSN MODT002*.
- [74] The CMS collaboration. Missing transverse energy performance of the cms detector. *Journal of Instrumentation*, 6(09):P09001, 2011.
- [75] Search for a standard model like Higgs boson in the decay channel H to ZZ to l+l- q qbar at CMS. Technical Report CMS-AS-HIG-13-064, CERN, Geneva, 2013.
- [76] The Egamma ID Group. Tag and probe methodology for analysis using electron and photons. *CMS-AN-2012/116*, 2012.
- [77] The CMS Collaboration. Measurements of the Inclusive W and Z Cross Sections in pp Collisions at $\sqrt{s} = 7$ TeV. *JHEP*, 1101:080, 2011.
- [78] The Crystal Ball Function. http://en.wikipedia.org/wiki/Crystal_Ball_function, 2014.
- [79] Michael Hildreth. Estimating systematic errors due to pileup modeling. twiki, 2012.
- [80] et Al. Michiel Botje. The PDF4LHC Working Group Interim Recommendations. <http://arxiv.org/abs/1101.0538>, 2011.
- [81] Hung-Liang Lai, Marco Guzzi, Joey Huston, Zhao Li, Pavel M. Nadolsky, et al. New parton distributions for collider physics. *Phys.Rev.*, D82:074024, 2010.
- [82] A.D. Martin, W.J. Stirling, R.S. Thorne, and G. Watt. Parton distributions for the LHC. *Eur.Phys.J.*, C63:189–285, 2009.
- [83] Richard D. Ball, Valerio Bertone, Francesco Cerutti, Luigi Del Debbio, Stefano Forte, et al. Impact of Heavy Quark Masses on Parton Distributions and LHC Phenomenology. *Nucl.Phys.*, B849:296–363, 2011.
- [84] CMS Collaboration. Discovery of a new boson in the search for the standard model higgs boson in the hzz2l channel in pp collisions at $\sqrt{s}=7$ and 8 tev. CMS Note 2012/367, 2012.
- [85] CMS Collaboration. Cms luminosity based on pixel cluster counting - summer 2012 update. CMS Physics Analysis Summary CMS-PAS-LUM-12-001, 2012.
- [86] Stefano Goria, Giampiero Passarino, and Dario Rosco. The Higgs Boson Line-shape. *Nucl.Phys.*, B864:530–579, 2012.
- [87] LHC Higgs Cross Section Working Group web page.
- [88] Giampiero Passarino. Higgs Interference Effects in $gg \rightarrow ZZ$ and their Uncertainty. *JHEP*, 1208:146, 2012.
- [89] G. Cowan, K. Cranmer, E. Gross, O. Vitells. Asymptotic formula for likelihood based tests of new physics. *Eur. Phys. J.*, C71:1554, 2011.

- [90] CMS Higgs Combination Group. Documentation of the RooStats-based statistics tools for Higgs PAG. <https://twiki.cern.ch/twiki/bin/view/CMS/SWGuideHiggsAnalysisCombinedLimit>, 2011.
- [91] CMS Collaboration. Search for a higgs boson in the decay channel $h \rightarrow zz^(*) \rightarrow q\bar{q}l^-l^+$. 2011.
- [92] S. Bolognesi, A. Bonato, D. Del Re, A.V. Gritsan, M. Manelli, M. Mozer, F. Pandolfi, N.V Tran, and A. Whitbeck. Search for the standard model higgs boson in the decay channel $h \rightarrow zz \rightarrow 2\ell 2q$ at cms. *CMS Note*, CMS-AN-2011/388, 2011.
- [93] Fermi Dirac Statistics. http://en.wikipedia.org/wiki/Fermi-Dirac_statistics, 2014.
- [94] Michalangel L. Mangano. The super-LHC. *CERN-PH-TH/2009-164*, 2009.
- [95] J. Segal S. I. Parker, C. J. Kenney. 3DA proposed new architecture for solid-state radiation detectors. *Nucl. Instr. Meth. A*, 395:328–343, 1997.
- [96] O. Koybasi, E. Alagoz, A. Krzywda, K. Arndt, G. Bolla, D. Bortoletto, T-E Hansen, T.A. Hansen, G.U. Jensen, A. Kok, S. Kwan, N. Lietaer, R. Rivera, I. Shipsey, L. Uplegger, and C. Da Via. Electrical characterization and preliminary beam test results of 3d silicon cms pixel detectors. *Nuclear Science, IEEE Transactions on*, 58(3):1315–1323, 2011.
- [97] O. Koybasi, D. Bortoletto, T-E Hansen, A. Kok, T.A. Hansen, N. Lietaer, G.U. Jensen, A. Summanwar, G. Bolla, and S.W.L. Kwan. Design, simulation, fabrication, and preliminary tests of 3d cms pixel detectors for the super-lhc. *Nuclear Science, IEEE Transactions on*, 57(5):2897–2905, 2010.
- [98] A. Kumar. Commissioning of the CMS forward pixel detector. *JINST*, 4:P03026, 2009.